



City Research Online

City, University of London Institutional Repository

Citation: Nomoni, M. (2024). Novel Pulsatile Phantoms in Photoplethysmography. (Unpublished Doctoral thesis, City, University of London)

This is the accepted version of the paper.

This version of the publication may differ from the final published version.

Permanent repository link: <https://openaccess.city.ac.uk/id/eprint/33288/>

Link to published version:

Copyright: City Research Online aims to make research outputs of City, University of London available to a wider audience. Copyright and Moral Rights remain with the author(s) and/or copyright holders. URLs from City Research Online may be freely distributed and linked to.

Reuse: Copies of full items can be used for personal research or study, educational, or not-for-profit purposes without prior permission or charge. Provided that the authors, title and full bibliographic details are credited, a hyperlink and/or URL is given for the original metadata page and the content is not changed in any way.

Novel Pulsatile Phantoms in Photoplethysmography

Michelle Nomoni

A thesis submitted to the graduate faculty in partial fulfilment
of the requirements for the degree of Doctor of Philosophy in
Biomedical Engineering



School of Science and Technology
Research Centre for Biomedical Engineering
City, University of London

2024

Table of Contents

TABLE OF CONTENTS	I
TABLE OF FIGURES	III
TABLE OF TABLES.....	VI
ACKNOWLEDGEMENTS.....	VII
DECLARATION	VIII
ABBREVIATIONS.....	IX
PUBLICATIONS.....	X
ABSTRACT	XI
1. INTRODUCTION	1
INTRODUCTION	1
THESIS STRUCTURE	3
1.1. 2. INTRODUCTION TO BLOOD PRESSURE	6
1.2. INTRODUCTION	6
2.1. ANATOMY AND PHYSIOLOGY.....	7
2.2. BLOOD FLOW	16
2.3. PATHOLOGY	22
2.4. MEASURING BLOOD PRESSURE.....	26
2.5. CONCLUSION.....	32
3. PRINCIPLES OF PHOTOPLETHYSMOGRAPHY	34
3.1. INTRODUCTION	34
3.2. LIGHT TISSUE INTERACTION	35
3.3. PRINCIPLES OF PHOTOPLETHYSMOGRAPHY.....	41
3.4. PPG LIMITATIONS	47
3.5. PPG APPLICATIONS	49
4.1. CONCLUSION:.....	51
4.2. 4. PHANTOM TECHNOLOGIES.....	52
4.3. INTRODUCTION	52
4.4. TYPES OF PHANTOMS.....	53
4.5. DESIGN CONSIDERATIONS FOR PHANTOMS	56
4.6. ADVANCEMENTS IN PHANTOM TECHNOLOGIES	63
APPLICATIONS OF PHANTOMS IN PPG RESEARCH	64
LIMITATIONS AND CHALLENGES IN PHANTOM RESEARCH.....	66
CONCLUSION.....	67
5. DEVELOPMENT OF MEASUREMENT SYSTEMS.....	68
5.1 INTRODUCTION	68
5.2 BASIC PROBES	69
5.3 DYNAMIC PPG SYSTEM (DPPGS).....	71
5.4 PPG PROCESSING AND ACQUISITION SYSTEM	77
SUMMARY	79

	6. DEVELOPMENT OF PHANTOMS	80
	INTRODUCTION	80
	IDEAL SPECIFICATIONS	81
	BRACHIAL GELATINE PHANTOMS	83
	SILICONE PHANTOMS	86
	FABRICATIONS OF CUSTOM VESSEL	91
6.1.	VALIDATION OF VESSELS AND TISSUE	94
6.2.	SUMMARY	104
6.3.	7. INVESTIGATING SEPARATION DISTANCE & ARTERIAL DEPTH.....	106
6.4.	7.1 INTRODUCTION	106
6.5.	7.2 METHODS.....	107
6.6.	7.3 RESULTS.....	111
	SUMMARY	113
	8. INVESTIGATING HAEMODYNAMIC PROPERTIES	114
	8.1 INTRODUCTION	114
	8.2 IN-VITRO SYSTEM SETUP	114
	8.3 PPG ANALYSIS.....	122
	SUMMARY	125
	9. INVESTIGATING ARTERIAL COMPRESSION	126
	9.1 INTRODUCTION	126
	9.2 METHODOLOGY	127
	9.3 RESULTS.....	130
	SUMMARY	135
	10. DISCUSSION.....	136
	11. CONCLUSION	141
	REFERENCES	143

Table of Figures

FIGURE 1 LABELLED CROSS-SECTION OF THE HUMAN HEART SHOWING THE CHAMBERS AND VALVES.[24]	7
FIGURE 2 SUMMARY OF EVENTS OCCURRING DURING THE CARDIAC CYCLE [26]	8
FIGURE 3 NERVOUS SYSTEM CONTROL OF THE HEART. [23]	10
FIGURE 4 FACTORS AFFECTING CARDIAC OUTPUT [23]	11
FIGURE 5 ARTERIAL NETWORK OF THE RIGHT ARM [26]	13
FIGURE 6 ARTERIAL WALL STRUCTURE[26]	15
FIGURE 7 SIMPLE ELECTRIC CIRCUIT (LEFT) SIMPLE SYSTEMIC CIRCULATION SYSTEM MODEL (RIGHT)[45]	16
FIGURE 8 EXAMPLE OF BLOOD PRESSURE WAVEFORMS FROM TWO PATIENTS: (A) NORMOTENSIVE AND (B) HYPERTENSIVE.[46]	17
FIGURE 9 MEAN ARTERIAL PRESSURE AND PULSE PRESSURE.[46]	18
FIGURE 10 CONTRIBUTING COMPONENTS OF BLOOD PRESSURE. [46]	18
FIGURE 11 INTERMITTENT PRESSURE TO CONTINUOUS PRESSURE.[46]	19
FIGURE 12 A SIMPLIFIED VESSEL PRESENTED AS A TUBE.	20
FIGURE 13 NORMAL VASCULAR DISTENSIBILITY. VENTRICULAR/AORTA RATIO IN SYSTOLE (A) AND DIASTOLE (B)[46]	21
FIGURE 14 BLOOD PRESSURE CHART INDICATING THE RELEVANT RANGES FOR EACH CATEGORY OF MEASUREMENTS.[63]	27
FIGURE 15 MODEL DEMONSTRATING AN AUTOMATIC SPHYGMOMANOMETER.[66]	29
FIGURE 16 THE BEER-LAMBERT LAW FOR PPG IS VISUALLY DEPICTED IN A SCHEMATIC WHERE INCIDENT LIGHT INTENSITY (I_0) UNDERGOES EXPONENTIAL ATTENUATION WITHIN THE TISSUE (ILLUSTRATED IN RED), RESULTING IN A TRANSMITTED INTENSITY (I_t). THE LAW QUANTIFIES THIS ATTENUATION AS A FUNCTION OF THE MEDIUM'S EXTINCTION COEFFICIENT (ϵ), THE OPTICAL PATH LENGTH (L), AND THE CONCENTRATION (C) OF THE ABSORBER IN THE TISSUE. ADDITIONALLY, THE TERM G REPRESENTS A PARAMETER THAT VARIES WITH THE SYSTEM.....	39
FIGURE 17 DIAGRAM ILLUSTRATING PPG TECHNIQUES: (A) TRANSMITTANCE; (B) REFLECTANCE. THIS ILLUSTRATION DEPICTS ONLY THE PRIMARY PATHS OF PHOTONS THAT ARE EVENTUALLY DETECTED.[77].....	42
FIGURE 18 THE PPG WAVEFORM AND ITS COMPONENTS.[89]	43
FIGURE 19 A PPG PULSE AND ITS COMMON FEATURES.[90]	44
FIGURE 20 PHANTOMS FOR MEASURING CORONARY ARTERY CALZIFICATIONS, LIVER LESIONS AND LOW CONTRAST CAPABILITY OF CT SCAN PROTOCOLS. [122]	54
FIGURE 21 DEAL FLOW PHANTOM FOR DOPPLER AND COLOR DOPPLER FLOW RESEARCH AND DEVELOPMENT APPLICATIONS. [126].....	54
FIGURE 22 SIMULATION OF THE EYEBROW CRANIOTOMY AND SURGICAL CORRIDOR USING A SURGICAL PHANTOM. [136]	56
FIGURE 23 REFLECTANCE PPG PROBE. (A) ASSEMBLY 3D MODEL OF PROBE FRONT, OPTICAL COMPONENTS AND DIMENSIONS. (B) ASSEMBLY 3D MODEL OF PROBE BACKSIDE. (C) PROBE PCB MODEL. (D) FINAL MANUFACTURED PPG REFLECTANCE PROBE. [152]	70
FIGURE 24 PPG SENSOR COMPONENTS CARTRIDGES. (A) TOP-VIEW OF PHOTODIODE AND LED CARTRIDGE. (B) SIDE-VIEW OF CARTRIDGE. (C) BOTTOM-VIEW OF CARTRIDGE INSERTED INTO BRIDGE ARM.....	72
FIGURE 25 DPPGS V1. THE FIRST DYNAMIC SYSTEM THAT WAS DEVELOPED TO CONTROL THE SEPARATION DISTANCE OF A PPG SENSOR.....	73
FIGURE 26 DPPGS V2 IN SEPARATION MODE.....	ERROR! BOOKMARK NOT DEFINED. 5
FIGURE 27 DPPGS V2 IN COMPRESSION MODE.	76
FIGURE 28 DETAILED BLOCK DIAGRAM SHOWING THE ARCHITECTURE OF ZENPPG [155].....	79

FIGURE 29 (1) INITIAL CAD DESIGN FOR A SIMPLE DUAL VESSEL PHANTOM ENCLOSURE. (2) DUAL VESSEL PHANTOM WITH GELATINE TISSUE AND DUAL SILICONE VESSELS CONNECTED TO THE INVESTIGATION SETUP. (3) A 3D PRINTED ENCLOSURE WITH A MODIFIED DESIGN WITH FURTHER VESSELS ADDED.	85
FIGURE 30 NINE VESSEL GELATINE BRACHIAL PHANTOM.	86
FIGURE 31 PHANTOM PROTOTYPES. (1) A MULTIVESSEL FINGER PHANTOM WITH BLEED PORTS IN THE CONNECTING CHAMBERS. (2) MULTIVESSEL PHANTOM EXHIBITING UNDESIRE WARPING. (3) VERSION 1 OF A WORKING MULTIVESSEL PHANTOM.	88
FIGURE 32 ILLUSTRATION OF THE ASSEMBLED PHANTOM CONNECTED TO THE DISTRIBUTION NETWORK FIXED ON AN ACRYLIC SHEET.	89
FIGURE 33 PHOTO OF THE ASSEMBLED PHANTOM FIXED ON AN ACRYLIC SHEET.	90
FIGURE 34 CONTINUOUS DIP-COATING VESSEL FABRICATION METHOD.	93
FIGURE 35 AN IMAGE SHOWING THE TROUGH, HEATING ELEMENT AND DIP COATER.	93
FIGURE 36 IMAGES OF VESSEL CROSS SECTIONS. COMMERCIAL VESSEL (ID = 0.7 MM) (A) CUSTOM VESSEL (ID = 1.4 MM) (B) WITHDRAWN AT 10 MM·MIN ⁻¹ . (ID = INNER DIAMETER).	95
FIGURE 37 CROSS SECTION OF VESSELS REPRESENTING THE RADIAL ARTERY. COMMERCIAL SILICONE TUBE (LEFT) WITH OUTER DIAMETER OF 2.2 MM AND AN IMT OF 500 μM. CUSTOM SILICONE VESSEL (RIGHT) WITH OUTER DIAMETER OF 2.76 MM AND AN IMT OF 280 μM.	95
FIGURE 38 BOX PLOT OF WALL THICKNESSES MEASURED FROM CUSTOM VESSELS WITHDRAWN AT SEVERAL RATES.	96
FIGURE 39 THE INSTRON 5944 INSTALLED IN THE LAB (LEFT). CUSTOM RADIAL SILICONE VESSEL UNDERGOING TENSILE STRESS TEST (RIGHT).	97
FIGURE 40 TENSILE STRESS/STRAIN GRAPH OF COMMERCIAL AND CUSTOM VESSEL.	97
FIGURE 41 PHOTOGRAPH OF THE VESSEL INFLATION SET-UP. THE SYRINGE PUMP PROVIDED THE MANUAL CONTROL OF INTERNAL PRESSURE, WITH USER RELAYED FEEDBACK FROM THE PRESSURE TRANSDUCER. THE DIGITAL MICROSCOPE RECORDED THE PARAMETER CHANGES DURING INFLATION BY THE PUMP.	99
FIGURE 42 (A). 10% CATALYST VESSEL AT 0 MMHG WITH ANNOTATED PIXEL MEASUREMENTS OF DIAMETER AND LENGTH. (B) THE SAME 10% VESSEL AT 1000 MMHG INTERNAL PRESSURE WITH ANNOTATED PIXEL MEASUREMENTS OF DIAMETER AND LENGTH.	100
FIGURE 43 INTERNAL PRESSURE OF ARTERY AGAINST THE MEASURED EXTERNAL DIAMETER CHANGE FOR THREE CATALYST RATIOS.	101
FIGURE 44 SILICONE SAMPLE UNDER COMPRESSION TESTING.	102
FIGURE 45 MEASURED YOUNG'S MODULUS AT DIFFERENT CATALYST RATIOS WITH THE MARKED YM RANGE FOR THE FINGER AND FOREARM AS SEEN IN THE LITERATURE[164], [165]	103
FIGURE 46 THE PHOTOPLETHYSMOGRAPHY (PPG) SIGNAL FROM THE CLEAR VESSEL PHANTOMS. (A) COMMERCIAL VESSELS. (B) CUSTOM VESSELS. SNRR = SIGNAL-TO-NOISE RATIO (RED WAVELENGTH). SNRI = SIGNAL-TO-NOISE RATIO (INFRARED WAVELENGTH).	104
FIGURE 47 HOMOGENOUS PULSATILE PHANTOM WITH MULTIPLE VESSELS AND INCREASING DEPTHS FROM 3.2 MM (v1) TO 24.4 MM (v9). SEE TABLE 1 FOR ALL VESSEL DEPTHS.	108
FIGURE 48 IN- VITRO INVESTIGATION SETUP. THE PULSATILE PUMP (A) CONNECTED TO THE ARTERIAL NETWORK (B) WITH A PRESSURE TRANSDUCER (C) ATTACHED AT THE INFLOW OF THE PHANTOM (E). THE EMITTER AND DETECTOR WERE HELD BY THE BRIDGE (F). THE SEPARATION DISTANCE BETWEEN THEM IS CONTROLLED BY THE TRANSLATION BRIDGE (G) AND THE SIGNAL WAS ACQUIRED BY THE ZENPPG (H).	110
FIGURE 49 AN EIGHT SECOND WINDOW OF THE FILTERED PPG SIGNALS AT 4 MM.	111
FIGURE 50 A 3D SURFACE PLOT OF THE PPG SIGNAL STRENGTH AGAINST BOTH VARIABLE PARAMETERS. SEPARATION DISTANCE (MM) (X-AXIS). VESSEL DEPTH (MM)(Y-AXIS).	112
FIGURE 51 PUMP SETUP. ACTUAL IN-VITRO LAB SETUP (A), WITH DIAGRAMMATIC REPRESENTATION OF ALL MAJOR COMPONENTS (B).	115
FIGURE 52 BELL CURVE GENERATED USING EQ 8.1 & EQ. 8.2, IMPLEMENTED IN MATLAB (THEMATHWORKS, USA)	116

FIGURE 53 THE ANALOGUE FEEDBACK FROM THE DRIVING WAVEFORM (AO FEEDBACK), AND THE PRESSURE WAVES PRODUCED UNDER THE RESISTIVE CONDITION I. (IRC=OPEN, TPR=OPEN) IN THE SYSTEM AT THREE LOCATIONS: THE COMPLIANCE CHAMBER (P1), PRE-PHANTOM (P2) AND POST-PHANTOM (P3).	118
FIGURE 54 THE ANALOGUE FEEDBACK FROM THE DRIVING WAVEFORM (AO FEEDBACK), AND THE PRESSURE WAVES PRODUCED UNDER THE RESISTIVE CONDITION II. (IRC=OPEN, TPR=RESTRICTED) IN THE SYSTEM AT THREE LOCATIONS: THE COMPLIANCE CHAMBER (P1), PRE-PHANTOM (P2) AND POST-PHANTOM (P3).	118
FIGURE 55 THE ANALOGUE FEEDBACK FROM THE DRIVING WAVEFORM (AO FEEDBACK), AND THE PRESSURE WAVES PRODUCED UNDER THE RESISTIVE CONDITION III. (IRC=RESTRICTED, TPR=OPEN) IN THE SYSTEM AT THREE LOCATIONS: THE COMPLIANCE CHAMBER (P1), PRE-PHANTOM (P2) AND POST-PHANTOM (P3).	119
FIGURE 56 THE ANALOGUE FEEDBACK FROM THE DRIVING WAVEFORM (AO FEEDBACK), AND THE PRESSURE WAVES PRODUCED UNDER THE RESISTIVE CONDITION IV. (IRC=RESTRICTED, TPR=RESTRICTED) IN THE SYSTEM AT THREE LOCATIONS: THE COMPLIANCE CHAMBER (P1), PRE-PHANTOM (P2) AND POST-PHANTOM (P3).	119
FIGURE 57 THE PPG'S DETECTED AT THE PRE-PHANTOM (P2) PRESSURE TRANSDUCER FOR DIFFERENT COMBINATIONS OF RESISTIVE ELEMENTS POSITIONS. (A) ILIAC RESISTIVE COMPONENT (IRC) AND TOTAL PERIPHERAL RESISTANCE (TPR) BOTH UNRESTRICTED. (B) IRC UNRESTRICTED, TPR RESTRICTED. (C) IRC RESTRICTED, TPR UNRESTRICTED. (D) IRC AND TPR RESTRICTED.	120
FIGURE 58 (A) THIS FIGURE PLOTS THE BLOOD PRESSURE VALUES PRE-PHANTOM AGAINST VARIED HEART RATES. (B) THIS FIGURE PLOTS THE BLOOD PRESSURE VALUES PRE-PHANTOM AGAINST VARIED FLOW RATES.	121
FIGURE 59 THE MEAN PPG AMPLITUDE OF THREE-MINUTE SAMPLES WITH 6 L·MIN ⁻¹ FLOW AND HEART RATES FROM 40–120 BPM (ALL SD < 0.003).	122
FIGURE 60 THE MEAN PPG AMPLITUDE OF THREE-MINUTE SAMPLES WITH 60 BPM HEART RATE AND FLOW FROM 1–12 L·MIN ⁻¹ (ALL SD < 0.003).	123
FIGURE 61 RED (TOP) AND INFRARED (BOTTOM) PPGS FROM THE FINGER PHANTOM AT FOUR DIFFERENT BLOOD PRESSURE RANGES; 90/50 MMHG (BLACK), 110/70 MMHG (RED), 140/100 MMHG (GREEN) AND 170/130 MMHG (BLUE).	124
FIGURE 62 PULSATILE FLOW RIG DIAGRAM FOR COMPRESSION STUDY.	128
FIGURE 63 PHOTO OF PULSATILE FLOW RIG SET-UP. THE OPTICAL SENSOR IS ATTACHED TO THE DPPGS V2 SYSTEM DESCRIBED IN CHAPTER 5.	128
FIGURE 64 : APPLICATION AND RELEASE OF FORCE ON A VESSEL-TISSUE PHANTOM SIGNAL PROFILE.	130
FIGURE 65 SIDE PROFILE VIEW OF PHANTOM TAKEN AT (LEFT) STAGE A OF THE PROTOCOL WHERE THE SENSOR IS JUST ABOVE THE SURFACE, AND (RIGHT) STAGE E WHERE IT OCCLUDES THE FLOW.	130
FIGURE 66 OSCILLOMETRY: THE OSCILLOMETRIC PULSE EFFECT THAT OCCURS IN SPHYGMOMANOMETER AS CUFF PRESSURE DEFLATES	131
FIGURE 67 ITERATION PLOTS FOR HYPOTENSIVE FLOW EXPERIMENT. EACH GRAPH IN THIS SERIES OF SIX SHOWS ONE ITERATION OF THE EXPERIMENT UNDER HYPOTENSIVE CONDITIONS UNDERGOING APPLIED PRESSURE, WITH THE PPG SIGNAL IN BLUE AND LOAD CELL DATA IN ORANGE. TMAX 1 IS INDICATED ON EACH PLOT.	132
FIGURE 68 ITERATION PLOTS FOR HYPOTENSIVE FLOW EXPERIMENT. EACH GRAPH IN THIS SERIES OF SIX SHOWS ONE ITERATION OF THE EXPERIMENT UNDER HYPOTENSIVE CONDITIONS UNDERGOING RELEASED PRESSURE, WITH THE PPG SIGNAL IN BLUE AND LOAD CELL DATA IN ORANGE. TMAX 2 IS INDICATED ON EACH PLOT.	132
FIGURE 69 THE FORCE AT TMAX 1 FOR EACH BLOOD PRESSURE LEVEL.	133
FIGURE 70 THE FORCE AT TMAX 2 FOR EACH BLOOD PRESSURE LEVEL.	134

Table of Tables

TABLE 1 VESSEL DIMENSIONS OF ARTERIAL FLOW BRANCH FROM HEART TO FINGER.	12
TABLE 2: COMPARATIVE ANALYSIS OF GELATINE-BASED AND SILICONE-BASED PHANTOMS IN PPG APPLICATIONS. THIS TABLE OUTLINES KEY CHARACTERISTICS OF GELATINE AND SILICONE WHEN USED IN THE FABRICATION OF PHOTOPLETHYSMOGRAPHY (PPG) PHANTOMS, HIGHLIGHTING THEIR RESPECTIVE DURABILITY, COST, BIOLOGICAL FIDELITY, CUSTOMIZABILITY, PROCESSING REQUIREMENTS, STABILITY, OPTICAL PROPERTIES, AND MECHANICAL PROPERTIES. THE COMPARISON SERVES TO INFORM MATERIAL SELECTION BASED ON SPECIFIC REQUIREMENTS AND OBJECTIVES IN PPG PHANTOM DEVELOPMENT. [116], [117], [121], [124].....	57
TABLE 3 SPECIFICATIONS FOR ALL DPPGS V2 SYSTEM COMPONENTS	77
TABLE 4 RESULTS COMPARING SHORE HARDNESS AT EACH FINGERTIP AND THE VALUE FOR THE POLYDIMETHYLSILOXANE (PDMS) WHEN MIXED WITH 3% CATALYST. A CATALYST RATIO BELOW 3% WAS FOUND TO BE UNSTABLE. MEASUREMENTS TAKEN WITH A SHORE 00 DUROMETER.....	102
TABLE 5 SIGNAL-TO-NOISE RATIO FOR ALL VESSEL DEPTHS.....	112
TABLE 6 SPECIFICATION FOR THE BDC PUMP AND ITS PRESSURE TRANSDUCERS	115
TABLE 7 MEASURED PRESSURES IN EACH BLOOD PRESSURE STATE AT THE INPUT OF THE PHANTOM.	129
TABLE 8 THE MEAN FORCE VALUES FOR TMAX 1 AND TMAX 2.....	133

Acknowledgements

This journey of pursuing my PhD has been a monumental chapter in my life, and it would not have been possible without the unwavering support and love of my family. To my mother, who instilled in me the virtue of strength, to my father, who taught me the essence of courage, and to my three brothers, to whom I owe so much, I express my deepest gratitude. Your support and belief in my abilities have been the foundation of my perseverance and success.

I extend my heartfelt thanks to Professor Panicos Kyriacou, whose guidance and patience have been invaluable throughout this journey. His wisdom and mentorship have shaped my research and personal growth in profound ways. Special thanks to Dr. James May, whose endless reservoir of knowledge was always available for me to tap into. His insights and advice have been pivotal in navigating the complexities of my research.

I am immensely grateful to my colleagues and friends at the Research Centre for Biomedical Engineering. The friendship, intellectual discussions, and lunchtime conversations have not only enriched my research experience but have also provided much-needed moments of relaxation and laughter.

A special mention to Dr. Mahsa Sheikh and Dr. Maria Roldan for the countless coffee dates that have been a sanctuary from the stresses of our studies and life. These moments are engrained in my mind forever.

Finally, I acknowledge the circumstances in life that has enabled me to embark on this PhD journey. Recognizing the opportunities I have been blessed with, I embarked on this path with a sense of responsibility and purpose.

Declaration

I, Michelle Nomoni, declare that the work presented in this thesis is my work. In the text, any idea, result, or illustration originating from the work of other subjects has been acknowledged. I confirm that the work was carried out entirely as part of my Doctor of Philosophy in Biomedical Engineering candidature at City University of London. I further ensure that this thesis has never been published or submitted elsewhere for obtaining an academic degree or professional qualification.

Michelle Nomoni

Abbreviations

AC	Alternating Current
AI	Artificial Intelligence
BPM	Beats Per Minute
BP	Blood Pressure
CO	Cardiac Output
CV	Cardiovascular
CVD	Cardiovascular Disease
CT	Computer Tomography
DAQ	Data Acquisition
DBP	Diastolic Blood Pressure
DPF	Differential Pathlength Factor
DC	Direct Current
DPPGS	Dynamic Ppg System
EKG	Electrocardiogram
EDV	End-Diastolic Volume
FFT	Fast Fourier Transform
FIR	Finite Impulse Response
HR	Heart Rate
HRV	Heart Rate Variability
IR	Infrared
IMT	Intima-Media Thickness
MAP	Mean Arterial Pressure
PPG	Photoplethysmography
PTT	Pulse Transit Time
PWV	Pulse Wave Velocity
RMS	Root-Mean Square
SBP	Systolic Blood Pressure
SV	Stroke Volume
TPR	Total Peripheral Resistance

Publications

Nomoni, Michelle & May, James. (2019). A Pulsatile Optical Tissue Phantom for the Investigation of Light-Tissue Interaction in Reflectance Photoplethysmography. Conference proceedings: ... Annual International Conference of the IEEE Engineering in Medicine and Biology Society. IEEE Engineering in Medicine and Biology Society. Conference. 2019. 3204-3207. 10.1109/EMBC.2019.8857036.

Nomoni, Michelle & May, James. (2020). Fabricating Novel PDMS Vessels for Phantoms in Photoplethysmography Investigations. Conference proceedings: ... Annual International Conference of the IEEE Engineering in Medicine and Biology Society. IEEE Engineering in Medicine and Biology Society. Conference. 2020. 4458-4461. 10.1109/EMBC44109.2020.9176476.

Nomoni, Michelle & May, James. (2020). Novel Polydimethylsiloxane (PDMS) Pulsatile Vascular Tissue Phantoms for the In-Vitro Investigation of Light Tissue Interaction in Photoplethysmography. Sensors. 20. 4246. 10.3390/s20154246.

May, James & Mejía-Mejía, Elisa & Nomoni, Michelle & Budidha, Karthik & Choi, Changmok & Kyriacou, Panicos. (2021). Effects of Contact Pressure in Reflectance Photoplethysmography in an In Vitro Tissue-Vessel Phantom. Sensors. 21. 8421. 10.3390/s21248421.

May, J.M. & Nomoni, Michelle & Budidha, Karthik & Choi, C.. (2022). Mechanical Testing of Artificial Vessels and Tissues for Photoplethysmography Phantoms. 2022. 629-632. 10.1109/EMBC48229.2022.9871830.

AWARD

“Michelle Nomoni wins the Sir Ivor Cohen Post-Graduate Award,” T. W. C. of Scientific Instrument makers, London, United Kingdom, 2018

Abstract

This thesis marks a significant advancement in photoplethysmography (PPG) with the development of novel pulsatile phantoms, primarily through the innovative application of a continuous dip-coating vessel production. This approach achieved vessels with median wall thickness of 60 μm , surpassing commercial solutions in replicating human vascular structures. The resulting phantoms closely mimic the mechanical and optical properties of biological tissue, enhancing the accuracy and realism of PPG in-vitro simulations.

A key component of this research was the development of specialized instrumentation to work in tandem with these advanced phantoms. This instrumentation, designed for precise data acquisition and analysis, has opened new possibilities for in-depth fundamental research in PPG. It enables more sophisticated studies into the interaction of light with vascular structures and facilitates a comprehensive examination of cardiovascular dynamics under various physiological conditions.

The use of these phantoms to simulate various blood pressure states has provided valuable insights into cardiovascular dynamics and their effect on PPG signal morphology. This has enhanced our understanding of the biophysical mechanisms of PPG and opened up possibilities for its use in comprehensive diagnostics, potentially transforming early detection and monitoring of cardiovascular conditions. The arterial compression study in this thesis demonstrates the potential of PPG for non-invasive blood pressure monitoring. By developing phantoms that replicate human arterial behaviour under different compression levels, we have established promising correlations that are fundamental for the future development of non-invasive blood pressure monitoring devices.

Looking to the future, the advancements in phantom design and instrumentation lay a solid foundation for advancing PPG technology. The potential to refine these models further, including the incorporation of microvascular structures and multi-layered tissue characteristics, promises to open new avenues in cardiovascular research. This progress is expected to significantly enhance non-invasive cardiovascular monitoring, with broad implications for clinical research and healthcare applications.

1

Introduction

INTRODUCTION.....	1
THESIS STRUCTURE.....	3

1.1.
1.2.

Introduction

1.1.

Photoplethysmography (PPG) is an optical technique used to measure several hemodynamic properties with recognised monitoring applications in clinical environments[1]. In principle, PPGs are obtained from a simple optical sensor that transmits and detects light from a volume of tissue. The vessels within tissue contain more blood during systole than diastole, and this change of blood volume causes the absorption variations of photons which result in the PPG waveform [2]. First explored in the 1930's, it wasn't until the invention of the pulse oximeter in 1974, that the PPG was utilised for clinical monitoring, specifically in anaesthetic practise [3], [4]. PPG technology has many advantageous attributes, of which two distinct features have led to its widespread use: the accessibility of sensor components leading to their inexpensive price, and the robustness of its' simple operation with minimal user error. These advantages have enabled the recent expansion in the field with innovative non-invasive techniques in physiological monitoring and vascular assessment. The resurgent interest in PPG devices in the last decade stems from the growing demand for wearable health sensors, such as smart watches or exercise bands that provide non-invasive assessment of cardiovascular physiology[5], [6], [7] .

One major haemodynamic property of interest is blood pressure. Associated with considerable mortality, hypertension is a worldwide public health challenge. With one third of adults globally having hypertension, its detection and monitoring is a key area of

interest[8]. Regular monitoring of blood pressure can aid in early prevention and treatment to avoid possible cardiovascular complications. Prolonged hypertension, when left untreated can cause long term damage to internal organs [9]. Current healthcare systems have only enabled one third of the population dealing with hypertension to manage and maintain their blood pressure within a healthy range [10]. This is mostly attributed to the lack of access to reliable and continuous blood pressure monitoring systems.

Established methods to measure blood pressure in clinical practise fall within two main categories. The invasive method, which is to carry out a procedure of catheterization and insert a pressure sensor directly into a vessel and towards the heart to measure arterial pressure. This method is internationally recognised as the gold standard for its high accuracy and continuous readings of blood pressure[11]. Due to its highly invasive nature, this method carries several risks such as bleeding and infection, and as such is mostly reserved for critically ill-patients and is primarily found in intensive care units[12], [13], [14]. The more common method found in clinical practice is the use of non-invasive cuff-based devices. They employ either oscillometric or auscultatory techniques[15], [16]. [17], [18] Cuff-based methods provide blood pressure measurements with comparatively minimal risk or side effects when compared to invasive measurements. The major drawback of cuff-based devices is the use of the cuff itself. This method requires the inflation and deflation of the cuff to register a reading, which limits these devices to intermittent readings. Many patients find it cumbersome and painful with long term use as it interrupts regular blood flow.

The limitations of currently established blood pressure monitoring devices have opened a field of research into new blood pressure measurement techniques, with the utilisation of PPG showing great promise. The combination of an inexpensive sensor, modern advances in wearable technology and machine learning algorithms has motivated research groups to produce a cuff-less, non-invasive, continuous and calibration free blood pressure monitoring device[19], [20], [21]. These devices presently exist in various forms but improved reliability, and accuracy is essential for an approved medical monitoring device.

In this pursuit of developing new methods to employ PPG techniques in medical devices, such as the potential measurement of blood pressure previously discussed, an important intermediate stage has been identified, which is the use of phantoms in an in-vitro environment. During the development stage of a new medical device, a large dataset of patient signals is required. This is a major hurdle, of not only new blood pressure devices, but many emerging medical monitoring methods. This is where phantoms have been identified as a crucial intermediate step in the development cycle of a new medical devices[22], [23], [24]. The major limitations in data collection during investigations, are the restrictive measures enforced when testing on human patients. To build a dataset for blood pressure technology, readings at varying blood pressures is vital, which during in-vivo experiments are constrained by the inability to induce hypertension or hypotension on demand in individual patients. A solution is to build an advanced in-vitro environment that closely mimics the region of the body the PPG measurements will be taken from. A phantom can be designed to imitate the optical and mechanical properties of the tissue in that region and variables such as heart rate, stroke volume and blood pressure can be isolated and controlled.

The focus and novelty of this research project is to develop for the first time a comprehensive in-vitro system capable of isolating variables to then investigate in isolation. More specifically, this work will focus on the challenges faced with current phantom technology and how new 1.2. techniques developed in this work can solve them.

Thesis Structure

Chapter 2: Introduction to Blood Pressure

This chapter will cover the basic anatomy and physiology background of the cardiovascular system with emphasis on the production and regulation of blood pressure and flow. This chapter will also describe some of the main pathologies associated with the cardiovascular system that affect blood pressure. This is followed by a brief history of clinical blood pressure measurement devices and more recently developed measurement techniques.

Chapter 3: Principles of Photoplethysmography

This chapter will provide an in-depth breakdown of the physics of light and the phenomena that occur when light interacts with biological tissues. It covers the basic principles of operation of PPG, standard waveform characteristics and the history of the origin of the signal. The main applications and limitations are also presented.

Chapter 4: Phantom Technologies

This chapter will present the uses of phantoms and its applicable benefits to in-vitro PPG research. The chapter will outline the current phantoms in development and where the main limitations of phantom research lie.

Chapter 5: Development of the PPG Measurement system

This chapter will detail the development of a versatile PPG measurement systems used throughout the investigations of this thesis. It will provide a guide to development of custom PPG sensors and the custom rigs employed in the experiments.

Chapter 6: Development of Pulsatile Tissue Phantoms

This chapter will cover the development journey of phantoms in this work. Starting from gelatine phantoms and the development steps to a silicone phantom. The novel fabrication method for custom vessels will be detailed. This chapter will also report on the mechanical testing protocols carried out to validate the properties of the phantom.

Chapter 7: Investigation of Separation Distance and Arterial Depth

This chapter describes the first set of experiment carried out on a brachial gelatine phantom. The separation distance between the emitter and detector of a PPG sensor was investigated on a phantom with arteries at various depths. The study motivation, protocol, data acquired, and statistical analysis are presented. This chapter highlights the effect separation distance has on the quality of PPG signals obtained and the depth of the artery also affects it.

Chapter 8: Investigation of the Haemodynamic Properties

This chapter describes the first set of experiments carried out to validate the system. The study motivation, protocol, data acquired, and statistical analysis are presented. This chapter highlights the effect different haemodynamic properties have on the PPG signal in a fundamental investigation.

Chapter 9: Investigation of Arterial Compression

This chapter presents the oscillometric investigation carried out on the phantom through transmural compression. The study motivation, protocol, data acquired, and statistical analysis are presented. This work is vital for improvement of BP estimation reliability and accuracy.

Chapter 10: Conclusion

This chapter discusses the results and observations made in previous chapters and presents final conclusions, remarks, limitations and suggestions for future work.

2

Introduction to Blood Pressure

2.1. INTRODUCTION	6
2.2. ANATOMY AND PHYSIOLOGY	7
2.2.1. THE HEART	7
2.2.2. CARDIAC OUTPUT.....	9
2.2.3. VASCULATURE	11
2.3. BLOOD FLOW	16
2.4. PATHOLOGY	22
2.4.1. CARDIOVASCULAR DISEASE	22
2.4.2. HYPERTENSION	23
2.4.3. HYPOTENSION	25
2.5. MEASURING BLOOD PRESSURE	26
2.5.1. ESTABLISHED METHODS	27
2.5.2. CUFFLESS METHODS	29
CONCLUSION	32

2.1. Introduction

The focus of this project was to investigate the effect blood pressure has on the photoplethysmography (PPG) signal. The primary objective was to study how transmural pressure and PPG signals could potentially correlate to blood pressure readings, calibration-free. A comprehensive grasp of the underlying principles governing both optical and mechanical phenomena, specifically light propagation, and blood flow dynamics, is essential for this endeavour. This chapter provides a brief overview of the anatomy involved, from the brain, heart, and down to the vessels. It presents the information concerning changes in blood pressure and examples of related pathology. The chapter breaks down the long-standing established methods employed in clinical settings, along with some of the newer novel methods currently being developed.

Anatomy and Physiology

The cardiovascular system (CV) is essential to the human body, as it enables the connective transportation of gases, nutrients, wastes, electrolytes, and hormones throughout the body. It maintains blood flow to tissue cells through a network of vessels in the body, supporting thermoregulation for tissue defence and the immune system for repair [1]. The CV system consists of many key components: the heart, which pumps blood around the system through blood vessels; the blood, which acts as a transport medium; and the brain, which provides the automatic regulation of the cardiac muscles. This section introduces the anatomy and physiology of the cardiovascular system, with the vascular system and cardiac cycle discussed in detail, as they play a significant role in the production of the PPG signal.

2.2.1. The Heart

The heart is a synchronized dual pump composed of cardiac muscle, and its structure includes four chambers (left and right ventricles and corresponding atria) as well as atrioventricular valves that feature fibrous strands (chordae tendineae) connected to papillary muscles to prevent leakage and backflow of blood into the atria, as illustrated in Figure 1. The septum separates the right and left chambers of the heart, impeding blood overflow between the two ventricles. Contraction is regulated by a series of electrical impulses originating from the sinoatrial node (SA node) and proceeding to the atrioventricular node (AV node), resulting in the polarization and depolarization of the heart muscles.[25]

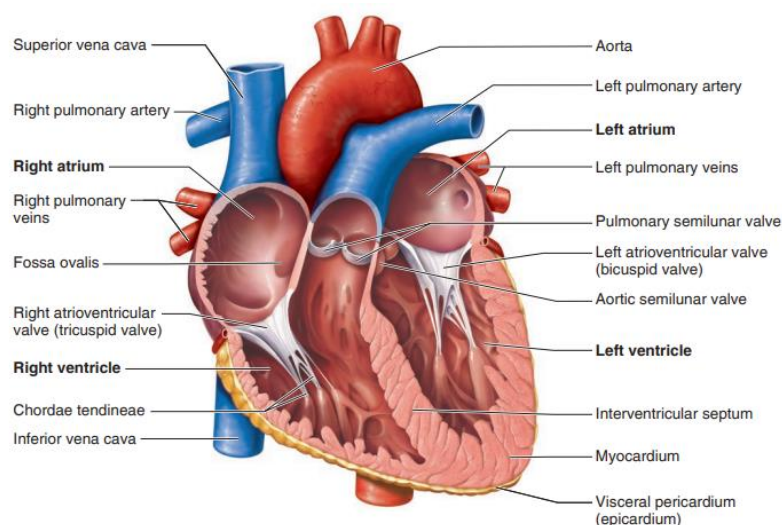


Figure 1 labelled Cross-section of the human heart showing the chambers and valves.[26]

The summary of events at each of the five periods of the cardiac cycle can be seen in Figure 2. It begins with the muscles relaxed, and the internal pressure low. The valves open and blood flows down from the atria into the ventricles (1). The tricuspid and mitral valves then open during atrial systole and the atria then contract, filling up the ventricles with passive blood (2). This leads to isovolumetric contraction (3). The atrioventricular valves are then shut closed due to the ventricular pressure rising above the atrial pressure, ventricular systole proceeds to increase the pressure causing the pulmonary and aortic valves to open. This initiates rapid ventricular ejection followed by reduced ventricular ejection (4). [27]

The right atrium is a highly distensible chamber that receives returning venous blood from systemic circulation at low pressures (0-4 mmHg) via the superior and inferior vena cava. During ejection, the right atrium and ventricle which has the tricuspid valve between them, pumps oxygen depleted blood returning from the body to the lungs via pulmonary artery. This generates a maximal systolic pressure of 20-30 mm Hg. The oxygenated blood returns to the left atrium via the pulmonary veins. The left ventricle is the chamber for systematic circulation around the body, which is ejected through the aorta. It produces a higher blood pressure and has a thicker wall than the right ventricle. The left ventricle generates a higher pressure of 100 – 140 mmHg.

Isovolumetric relaxation diastole occurs because of higher pressure in the aorta and pulmonary artery than the ventricles, closing all the valves (5). The process then repeats itself when the ventricular pressure drops below that of the atrium again. Sarcomere relaxation and collagen recoil action causes the atrioventricular valves to open resulting in rapid ventricular filling followed by reduced ventricular filling (1). The term cardiac cycle refers to the events of one complete heartbeat. [25], [28]

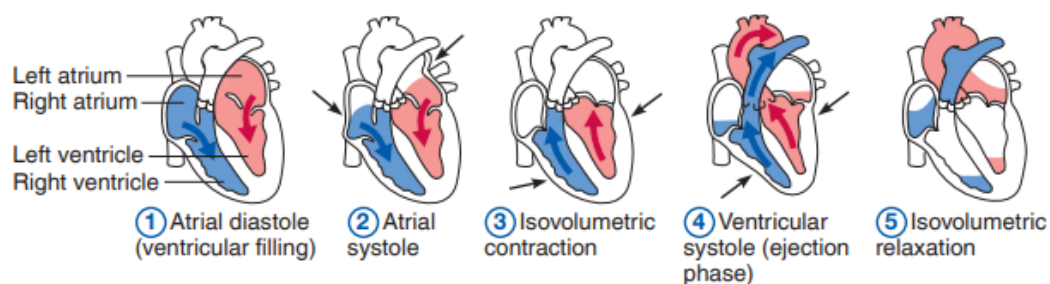


Figure 2 Summary of events occurring during the cardiac cycle [28]

2.2.2. Cardiac Output

Cardiac output (CO) is the amount of blood pumped out by the heart in one minute and is the product of stroke volume (SV), the volume of blood pumped out each cardiac cycle and the heart rate (HR), the number of cardiac cycles per minute. Stroke volume increases as the force of the ventricular contraction increases. The normal heart rate for an adult is 75 beats per minute (BPM) and the Normal stroke volume is about 70 ml per beat and so the average cardiac output of an adult can easily be calculated as

$$CO = HR.SV$$
$$CO = 75 \text{ bpm} . 70 \text{ ml} = 5.25 \text{ L/min.} \qquad \text{Cardiac Output}$$

Eq. 2.1

Normal adult total blood volume is 5.3 L [29], and so almost all of the body's blood supply passes through the heart every minute. Cardiac output varies with the demands of your body, it will vary when your heart rate or stroke volume decreases or increases. A healthy heart will regulate its stroke volume so that the blood that enters the chambers during the previous diastole is ejected in the consequent systole. At rest, 50-60% of blood volume is ejected during contraction, 40-50% of blood volume remains in the ventricles after systole. There are three main factors that affect stroke volume: preload, contractility, and afterload.

Preload describes the amount of stretch on the heart before contraction. The more the heart fills with blood during diastole, the larger the contraction during systole. As preload is proportional to end-diastolic volume (EDV), there are two factors that can ultimately affect it, the duration of diastole and venous return. When the heart rate exceeds 160 bpm, stroke volume often decreases caused by shorter filling times (diastole) which reduces preload. Healthy individuals with slower heart rates at rest will have longer filling periods and therefore larger preload forces resulting in a larger stroke volume. The relationship between preload and stroke volume is referred to as the Frank-Starling law. It is this law which also results in the equalised output of the heart from both sides. If the right side of the heart pumps

more blood, it results in a larger venous return on the left side, causing the preload to increase and the resulting contraction to increase its output, bringing the cycle back to balance.[25]

Contractility can be described as the strength of contractions at any level of preload. This is often affected by substances, either by positive inotropic agents that promote Ca^{2+} inflow during cardiac action potentials that increase contractility or by negative inotropic agents that reduce Ca^{2+} and decrease contractility. [30]

Afterload is the minimum pressure the ventricles must produce to force open the semilunar valves. The larger the afterload, the less volume of blood is ejected, decreasing the stroke volume. Hypertension and atherosclerosis are conditions that affect afterload. [31]

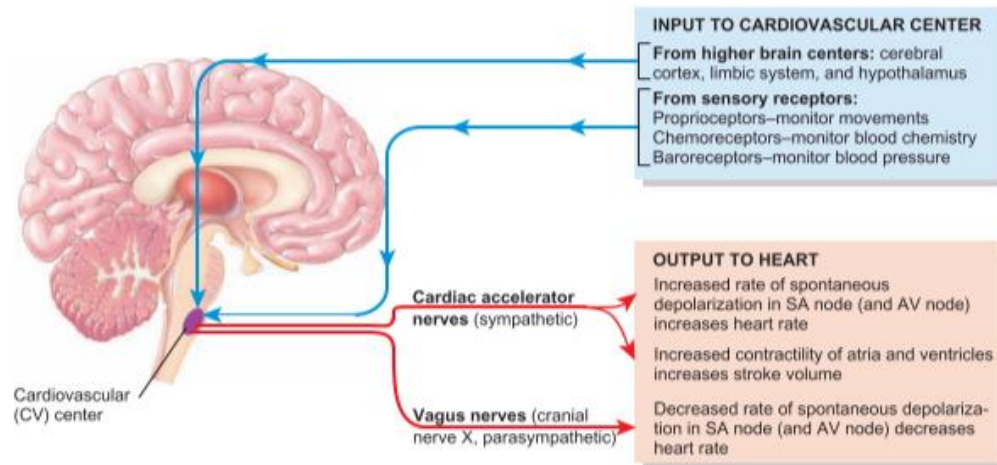


Figure 3 Nervous system control of the heart.[25]

Cardiac output is the product of not only stroke volume but also heart rate. The autonomic regulation of the heart rate originates in the cardiovascular centre of the brain, the medulla oblongata. Figure 3 presents the nervous system control of the heart. The medulla oblongata receives information from other brain centres and sensory receptors that determine its output to the heart, either increasing or decreasing the frequency of nerve impulses in both the sympathetic and parasympathetic nervous system branches of the autonomic nervous systems. Other factors such as certain chemicals, hormones, cations imbalance, and body temperature can all affect the regulation of the heart rate. Figure 4 summarises the factors that affect stroke volume and heart rate that led to increased cardiac output.

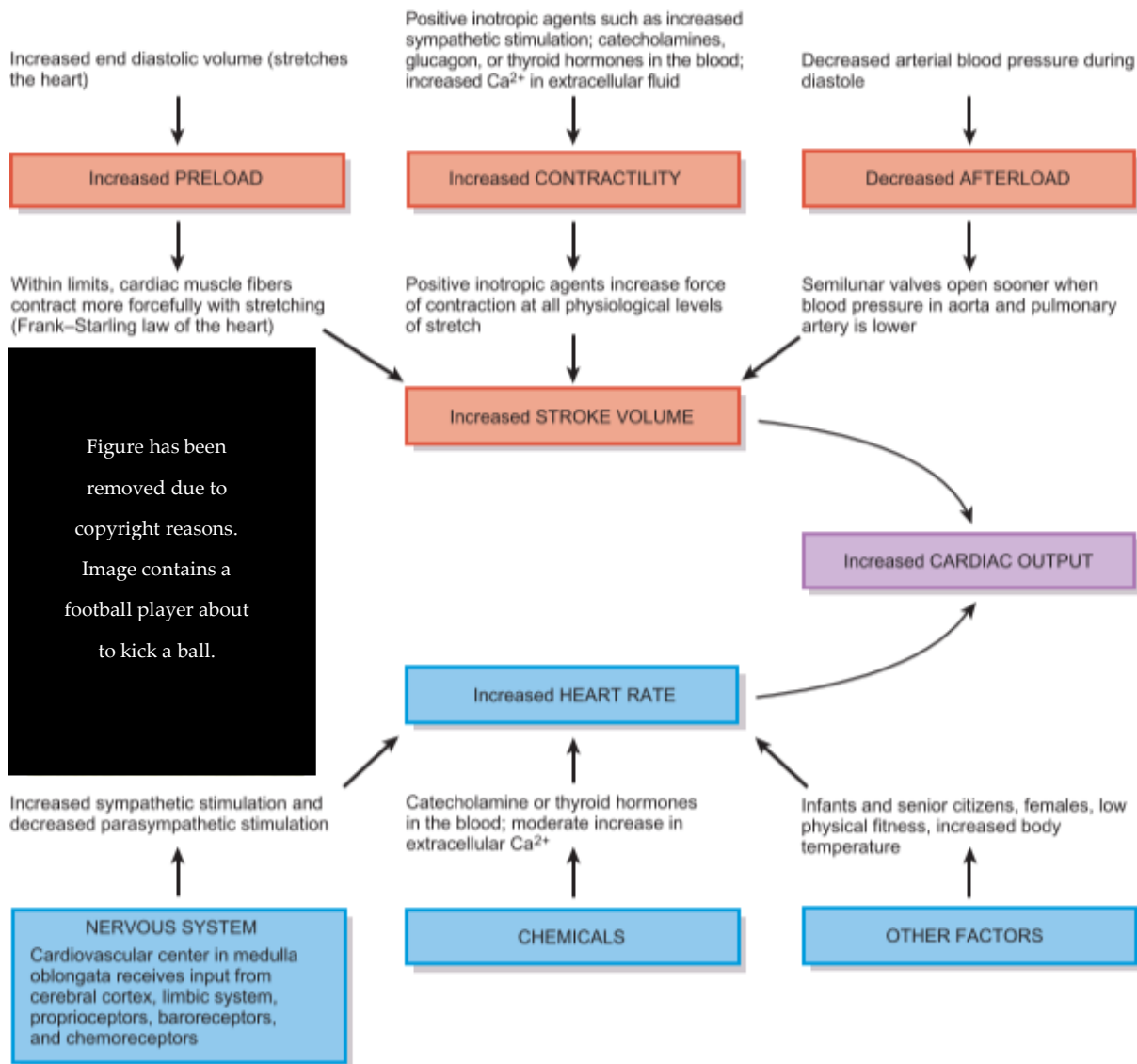


Figure 4 Factors affecting Cardiac output [25]

2.2.3. Vasculature

Blood is carried to and away from the heart to other organs via blood vessels. There are three main groups of vessels, arteries, veins and capillaries. Arteries are strong, elastic vessels that transport oxygenated blood away from the heart to body tissues under high pressures. As the heart propels the blood through these larger arteries, it flows into successively smaller arteries, and then into arterioles which supply the capillary beds. It is then drained by the

venules, which in turn branch into veins and eventually carry the blood back into the heart.[32]

This project will focus on the flow of blood leading to the finger. It originates at the aorta which distributes the oxygenated blood that the heart pumps out through the arterial system. It has a high compliance which dampens the output pulsatile pressure caused by intermittent ejection of blood from the left ventricle. The aorta is subdivided into sections i.e. ascending thoracic aorta, aortic arch, descending thoracic aorta, abdominal aorta and common iliac arteries. To travel towards the finger, blood first branches off the aortic arch into the brachiocephalic artery that subdivides into the right subclavian artery which then supplies the upper right arm, see Figure 5 Arterial network of the right arm.

The subclavian artery leads to the axillary artery and then to the brachial artery, which is the longest of the vessels in the arm. The brachial artery branches after the elbow bend into the radial and ulnar artery which carry the blood to the hand. These two arteries form the palmar arches that then branch off into the individual digital arteries of each finger. Table 1 lists dimensional data of the arterial flow branch from the heart to the finger. Due to the small size and lack of interest in the digital arteries, a figure could not be found for their wall thickness.

Table 1 Vessel dimensions of arterial flow branch from heart to finger.

Vessel	Outer Diameter	Wall Thickness	Reference
Ascending aorta	3 - 3.3 cm	2.36-2.67 mm	[33], [34], [35]
Subclavian artery	9 - 10.6 mm	1.35-1.38 mm	[36], [37]
Brachial artery	3.97 ± 0.64 mm	0.29 ± 0.1 mm	[38]
Radial artery	3.06-3.24 mm	0.25-0.28 mm	[39], [40], [41]
Superficial Palmar arch	1.4 -1.621 mm	0.075–0.138 mm	[41]
Digital arteries	0.89 -1.37 mm	-	[42]

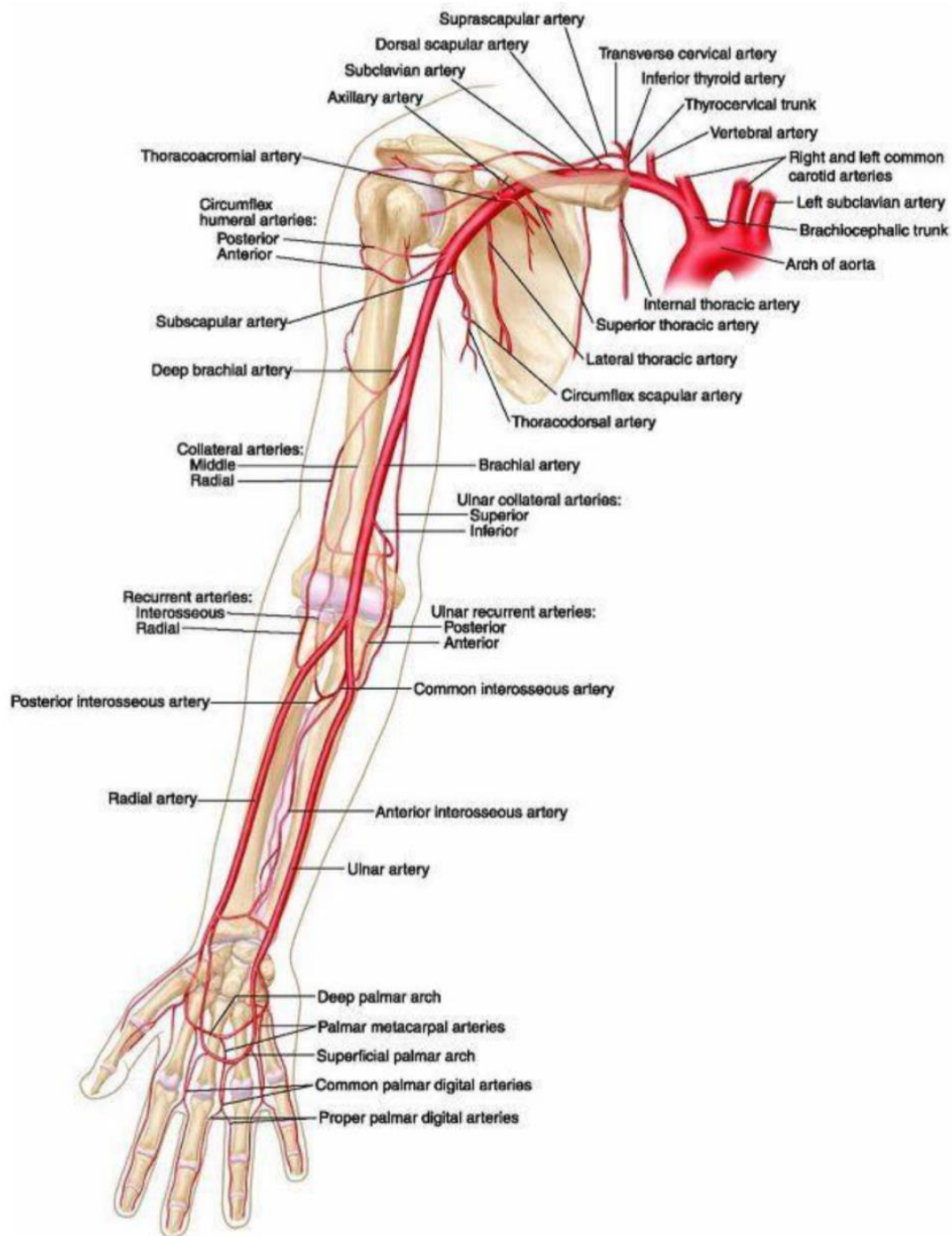


Figure 5 Arterial network of the right arm [28]

The brachial artery and radial artery can be used to measure arterial blood pressure as they are closest to the surface, making them detectable from the epidermis. These distributing arteries sub-divide into smaller vessels as they reach organs, eventually turning into arterioles that are connected to capillaries. The arterioles are also called the resistance vessels which aid

in distribution and regulation of blood pressure. The capillaries form the blood-tissue interface where diffusion of nutrients, waste products and gas exchange take place. Venules are tiny veins continuous with capillaries and transport blood into veins which return deoxygenated blood from tissues to the heart, it holds a large amount of blood with relatively low pressure [43].

The wall of all blood vessels (except capillaries) consists of three layers, see Figure 6. The outermost layer called the tunica adventitia is a connective tissue sheath separated from the middle layer (tunica media) by the external elastic lamina, which tethers the vessel loosely to the surrounding connective tissue. It mostly contains sympathetic fibre terminals that release a vasoconstriction agent which regulates the local resistance and blood flow. It may also contain a vascular network, vasa vasorum to provide nutritional support to outer regions of arterial wall. The middle layer called tunica media has two sub-layers, the outer layer is formed of smooth muscle cells and inner layer is matrix of elastic and collagen fibres. This layer supplies the mechanical strength and contractile power, so it has an important effect on arterial stiffness, and it is thicker in arteries than in veins. Lastly tunica intima (inner layer) is a sheet of flat endothelial cells resting on a thin layer of connective tissues.

The endothelial layer is the barrier to blood and secretes vasoactive products. The large arteries are capable of constriction and dilation but don't have any significant effect on pressure and blood flow. The major arteries (i.e. aorta, pulmonary artery and their branches) have very distensible walls as their tunica media is elastin rich, which enables arteries to act as temporary blood storage. This allows them to expand during heart's systole to accommodate high blood pressure and passively contract during diastole phase. The stretched elastin also stores mechanical energy (tension) which is used during diastole to maintain arterial blood pressure. This is the 'Windkessel effect' that describes effective propagation of energy provided by the heart to smoothen blood flow [44]

The Structure of an Artery Wall

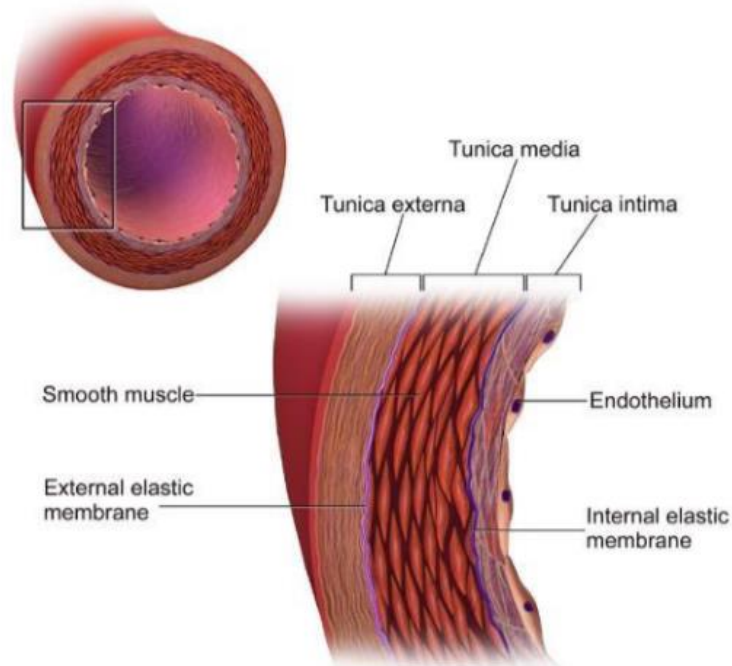


Figure 6 Arterial wall structure[28]

The arterial blood pressure in vessels does not fall below ~80 mmHg even though the heart pumps ejects blood intermittently, providing a continuous blood flow. Another protein mesh in media called collagen fibrils prevents over distension of arteries as it is stiff. The conduit (muscular) arteries include brachial and radial arteries. These contain more smooth muscle in their tunica media which is thicker relative to the lumen, and it prevents collapse at sharp bends. Their role is to conduct blood flow from elastic arteries to resistance vessels (arterioles). They have a rich sympathetic intervention and can change their diameter actively; dilate to facilitate increase blood flow and contraction reduces peripheral blood flow [45]. The vessels are in a partially constricted state (i.e. possess vascular tone), vasoconstriction means vascular smooth muscle will constrict and arteriole narrows, vasodilation refers to expansion of the lumen upon smooth muscle relaxing, it increases the radius and decreases the resistance of the vessel so the blood flow increases. Active tension from vascular smooth muscle and passive tension from the surrounding connective tissue i.e. collagen and elastin are the two components that contribute to wall tension. Constriction of smooth muscle increases active tension and decreases the radius [46].

Blood Flow

The cardiovascular system can be reduced to a simple electric circuit, where the pump (heart) pushes liquid (blood) in a rhythmic cycle through a series of dividing tubes (vessels). The electric circuit in Figure 7 is often used to describe the cardiovascular haemodynamic phenomena.

In accordance with Ohm's law (Figure 7 (left)), the potential difference across the supply, ($\Delta V = V_1 - V_2$) is defined by multiplying the current (I) and the resistance of the circuit (R).

$$\Delta V = I \cdot R$$

Eq. 1.2 Ohm's Law

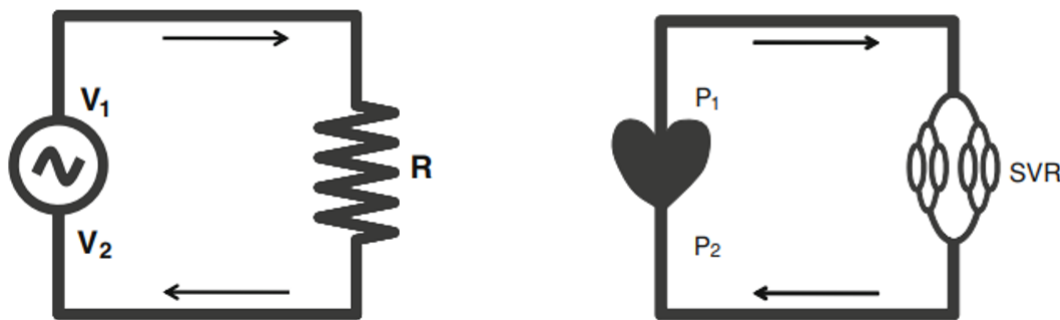


Figure 7 Simple electric circuit (left) Simple systemic circulation system model (right)[47]

The cardiovascular system can be modelled in a similar way (Figure 7 (right)), and the law which describes blood pressure can be derived directly from Ohm's law, where the pressure difference across the heart ($\Delta P = P_1 - P_2$) is defined by multiplying the cardiac output (CO) which represents the current (I), and the systemic vascular resistance (SVR) which represents the resistance of the whole circuit [48].

$$\Delta P = CO \cdot SVR$$

Eq. 2.2

The blood pressure at the point of return in the heart is considerably lower than the highest-pressure value and as such can be neglected. The equation can therefore be simplified by writing the pressure difference as the pressure in the aorta (P)

$$P = CO.SVR$$

Eq. 2.3

Cardiac output is calculated from the multiplication of stroke volume (SV) and heart rate (HR) see Equation 2.4. Blood pressure is changing throughout the cardiac cycle, so the P in this formula best refers to the mean arterial pressure (MAP). The formula can now be written as

$$MAP = SV.HR.SVR$$

Eq. 2.4

According to this formula, blood pressure is dependent on these three factors: stroke volume, heart rate and systemic vascular resistance. Although mean arterial pressure is an important parameter which remains relatively stable in through the arterial tree, it is prone to a simple problem. In the situation where two patients are measured to have the same MAP (100 mmHg), patient (a) has blood pressure values within the normal range and patient (b), who also has the same MAP value (100 mmHg) exhibits blood pressure values characterized as hypertension (Figure 8). These patients could also exhibit the same SV, HR and SVR values. This simple example quickly proves that these three parameters are insufficient to solely calculate blood pressure values, and the concept of pulse pressure must be explored.

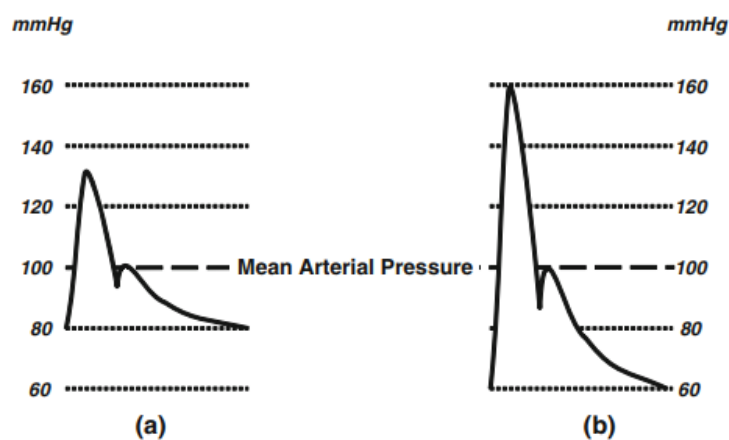


Figure 8 Example of blood pressure waveforms from two patients: (a) normotensive and (b) hypertensive.[48]

Accurate analysis of cardiovascular haemodynamics cannot ignore the two distinct components of blood pressure: the steady component (MAP) and the pulsatile component pulse pressure (PP), see Figure 9.

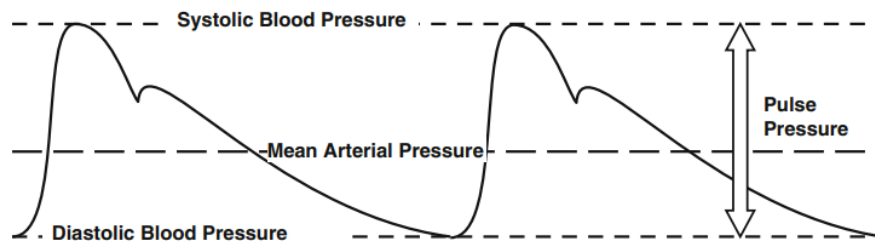


Figure 9 Mean arterial pressure and pulse pressure.[48]

This pulsatile component depends on two factors, the forward wave produced by the interaction of the heart and aorta, and the reflected waves. Figure 10 is a diagrammatic representation of all the components of blood pressure.[48]

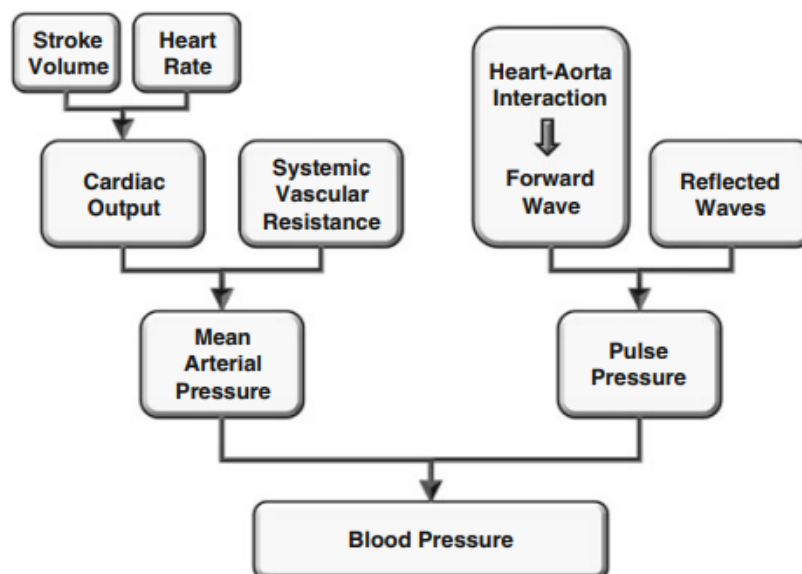


Figure 10 Contributing components of blood pressure. [48]

Large arteries play an important role in regulation of blood pressure and peripheral blood flow. The aorta and large arteries viscoelastic properties provide their buffer function where they can dampen the left ventricular stroke volume output. The cardiac cycle alternates between a contraction phase (systole), where a volume of blood is pushed into the arteries, and the relaxation phase (diastole), where ventricular filling occurs. The large arteries have

the role of dampening the pulsatile output, from intermittent flow to continuous flow, see Figure 11. The aorta stores a quantity of blood after the contraction phase so that the diastolic pressure is maintained.

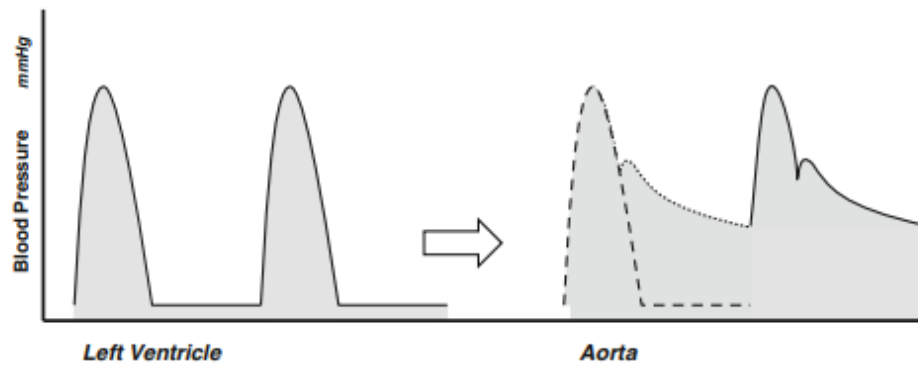


Figure 11 Intermittent pressure to continuous pressure.[48]

This phenomenon where intermittent flow changes to continuous flow due to the viscoelastic properties of the large arteries, is often referred to the Windkessel effect [49]. “Windkessel” means “air chamber” in German and refers to the system used in old fire engines. During the ejection phase, the intermittent pump would push water out through a closed chamber that limited the output of water so that some of it was stored. This would compress the air in the chamber and during the aspiration phase, the air in the chamber would continue to push water out. Stephen Hales first presented in 1733, a basic notion that the circulatory system could be represented by the Windkessel model, where the larger arteries acted as the air chambers.

This idea was then worked on by Otto Frank in 1899 [50], where he formulated mathematically a two element Windkessel model, consisting of two components, the peripheral resistance ‘ R ’ (arterioles and capillaries) and total arterial compliance ‘ C ’, the elasticity of the larger arteries.

$$Q = C \frac{p}{t} * \frac{p}{r}$$

Eq. 2.6

The highest mean blood pressure is found in the aorta (~100 mmHg) and the pressure progressively decreases as the blood flows through the vessels further away from the heart. Vessels have complex structures, branching and curvature but in essence they have the nature of a tube, see Figure 12. A simplified vessel presented as a tube. Flow in steady state is linearly proportional to pressure difference between two points, as explained by the simplified Poiseuille's law (Eq 2.7), where Q is flow, P₁-P₂ is pressure gradient and R is resistance:

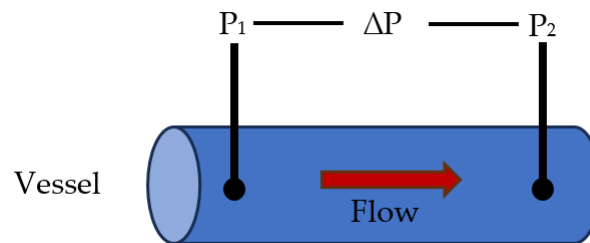


Figure 12 A simplified vessel presented as a tube.

$$Q = \Delta P / R$$

Eq. 2.7

Three factors determine resistance (R) to blood flow in a vessel; vessel length (L), blood viscosity (η) measure of internal friction within a moving fluid and radius (r) of the vessel:

$$R \propto (\eta \times L) / r^4$$

Eq. 2.8

Combining equation 2.7 with equation 2.8 gives Poiseuille's law which describes the dominant influence of vessel radius (r) on flow (F):

$$Q = \frac{\Delta P \pi r^4}{8 \eta l}$$

Poiseuille's Law Eq. 2.9

Equation 2.9 provides the concept of how pressure and flow are affected by blood viscosity and blood vessel changes, this makes the assumptions that the vessels are long, straight, rigid

tubes and, that the blood flow is under steady laminar (non-turbulent) flow conditions, and lastly that blood has a constant viscosity and is independent of flow i.e. Newtonian fluid. 40% of blood volume consists of red blood cells which are semisolid particles that increase the fluid viscosity and affect particles behaviour.[51], [52]

Most blood vessels under normal conditions have laminar blood flow, the orderly movement of adjacent layers of blood moving against the blood vessel wall which reduces energy lost in the flowing blood. Turbulence occurs when this flow is disrupted i.e. at arterial vessels, branching points of large arteries and ascending aorta of the heart. In large arteries turbulence creates a characteristic sound as higher velocities enhance it, the resulting 'murmurs' become louder when blood flow increases across a vessel i.e. when it narrows, this can be detected using a stethoscope. The loss of energy is increased, and a greater pressure drop occurs along the length of the vessel (Poiseuille's law). The parallel arrangement of vascular beds in the body reduces overall resistance and a resistance change in one vascular bed has minimal influence on pressure and flow in other vascular beds. Larger arteries resistance change has minimal effect on total resistance of the vascular bed compared to smaller arteries (resistance vessels).

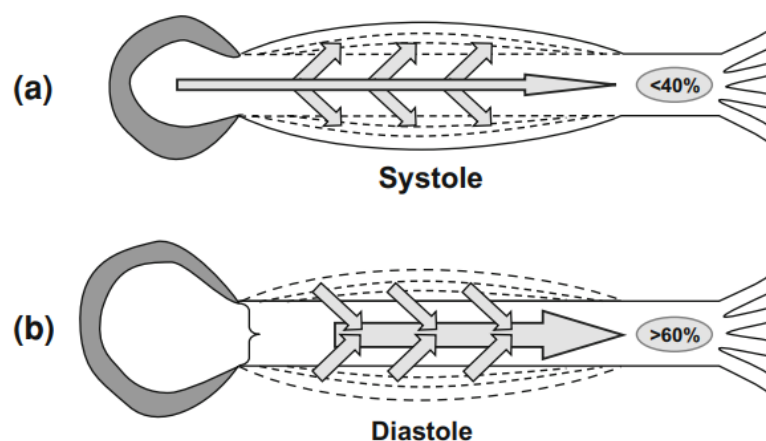


Figure 13 Normal vascular distensibility. ventricular/aorta ratio in systole (a) and diastole (b)[48]

Compliance, closely related to distensibility, is a measure of the change in volume that a vessel can undergo for a given change in pressure. High compliance means that the vessel can hold more blood for a small increase in pressure. This is particularly important in the aorta and other large arteries, which need to absorb the pulse pressure wave generated by the heart's

contractions and then gradually release that blood during diastole, thus ensuring a continuous flow of blood through the smaller vessels. Compliance is integral to the functioning of the circulatory system, helping to modulate blood flow and pressure in response to physiological demands and varying conditions within the vascular network. [51]

Pathology

2.4. Blood pressure is a vital physiological parameter that plays a crucial role in maintaining overall health and homeostasis within the human body. The regulation of blood pressure is a complex and finely tuned process, involving multiple factors, and deviations from the norm can lead to various pathologies. In this section, we will delve into an exploration of the primary pathologies that can disrupt the delicate balance of blood pressure and how these conditions impact the cardiovascular system.

2.4.1. Cardiovascular Disease

Cardiovascular disease (CVD) encompasses a range of conditions affecting the heart and blood vessels, including coronary artery disease, heart failure, arrhythmias, and peripheral arterial disease. While CVD encompasses various disorders, it significantly influences blood pressure and plays a pivotal role in the development and exacerbation of hypertension. [53]

Cardiovascular disease (CVD) and blood pressure are intricately linked, with their interactions governed by several factors, including compliance, arterial stiffness, and shared risk factors. Compliance, represented as $C = \Delta V / \Delta P$, is the relationship between changes in volume and pressure in the cardiovascular system. In blood vessels, compliance is determined by the relative proportion of elastin fibres, smooth muscle, and collagen in the vessel wall. Compliance alterations primarily affect pulse pressure, with mean arterial pressure remaining relatively stable unless influenced by cardiac output and systemic vascular resistance. [54]

Age, arteriosclerosis, and hypertension are pivotal factors that impact compliance. As individuals age, the compliance of their arteries diminishes. This change is influenced by various processes, including the mechanical stress placed on arteries and the deposition of

fatty materials in the vessel lumen. These factors can contribute to the deterioration of elastic fibres within the tunica media of blood vessels. Consequently, the arteries become stiffer and less capable of expanding, which requires the heart to exert more force to propel blood during each pulsation.[55]

Arterial stiffness, often inversely proportional to compliance, serves as a crucial indicator of cardiovascular health. As compliance of the arteries decreases with age, it can result in arterial stiffening. Stiffer arteries are less elastic and do not readily expand, causing increased resistance to blood flow. This altered dynamic has significant repercussions for blood pressure regulation. Notably, it affects the propagation of pressure waves within the arterial tree.[56]

Stiffer arteries can transmit pressure waves more rapidly than compliant vessels. This altered wave transmission can lead to the reflected wave arriving at the heart during systole rather than diastole, thereby interacting constructively with it. The increased arterial stiffness and associated changes in pressure wave dynamics can result in hypertrophy of the heart, a condition where the heart muscles thicken in response to increased workload. This hypertrophy of the heart is a critical component of cardiovascular disease and can contribute to further increases in blood pressure.[57]

2.4.2. Hypertension

Hypertension, commonly known as high blood pressure, is a chronic medical condition that arises from a multitude of interconnected factors, impacting the health of millions worldwide. Understanding the underlying pathophysiology of hypertension is essential for comprehending its diverse causes and far-reaching effects on health.[58]

Blood pressure is a product of cardiac output and systemic vascular resistance. In hypertension, alterations in these parameters disrupt the delicate balance that regulates blood pressure. An increase in systemic vascular resistance, often associated with arterial stiffness, leads to elevated pressure levels. This increased resistance stems from changes in the composition and function of the arterial walls, where the relative proportions of elastin fibres,

smooth muscle, and collagen play a pivotal role in determining compliance and, consequently, blood pressure.[59]

Hypertension rarely has a singular cause. Instead, it is a result of the interplay between various factors. While genetics and family history can predispose individuals to hypertension, modifiable risk factors play a crucial role. Lifestyle choices, including a diet high in salt and saturated fats, sedentary habits, smoking, and excessive alcohol consumption, contribute to the development and progression of hypertension. Chronic stress and underlying medical conditions, such as diabetes and kidney disease, further exacerbate the condition.[57]

The autonomic nervous system and various hormonal pathways are integral in the pathophysiology of hypertension. Increased release of neurotransmitters like norepinephrine, enhanced peripheral sensitivity, and heightened responsiveness to stressors characterize the autonomic dysfunction in hypertensive individuals. Additionally, the renin-angiotensin-aldosterone system (RAAS) plays a significant role in regulating blood pressure. The overactivation of RAAS can lead to sodium and fluid retention, increasing systemic vascular resistance.[26]

Hypertension triggers vascular remodelling, characterized by an increase in vascular smooth muscle mass. As the arterial walls thicken and lose elasticity, they become less compliant and resistant to stretching. This impairs their ability to adapt to variations in blood volume and cardiac output, ultimately raising blood pressure. The consequences of hypertension are profound and detrimental. It is a known risk factor for cardiovascular diseases, including coronary artery disease, heart attacks, heart failure, and strokes. Hypertension also increases the likelihood of kidney disease and vascular disorders, such as atherosclerosis and aneurysms.[56]

Aging introduces another layer of complexity to the pathophysiology of hypertension. In younger individuals, increased cardiac output is often the primary contributor to high blood pressure, while in older patients, systemic vascular resistance and arterial stiffness play dominant roles. With age, aorta and elastic arteries stiffen, amplifying pulse pressure, contributing to left ventricular hypertrophy, and increasing the risk of coronary heart disease.

The health consequences of hypertension are far-reaching. Over time, it can lead to end-organ damage and significantly impact morbidity and mortality. Uncontrolled high blood pressure places tremendous stress on the cardiovascular system, potentially resulting in heart disease, strokes, kidney damage, and vascular disorders. Cognitive impairment and an increased risk of dementia have also been associated with chronic hypertension.[60], [61]

In summary, hypertension is a complex medical condition with multifactorial causes, involving genetics, lifestyle, neurohormonal regulation, vascular remodelling, and age-related changes. Its far-reaching effects on health make it a significant public health concern, emphasizing the importance of early detection. Embracing emerging technologies, such as wearable devices, can play a pivotal role in addressing this significant public health concern. Early detection and proactive management are essential in shaping better health outcomes and reducing the overall impact of hypertension on individuals.

2.4.3. Hypotension

Hypotension, also called low blood pressure, condition in which the blood pressure is abnormally low, either because of reduced blood volume or because of increased blood-vessel capacity. Though not in itself an indication of ill health, it often accompanies disease. Hypotension is typically defined as systolic blood pressure below 90 mm Hg and diastolic blood pressure below 60 mm Hg. It can manifest as a transient condition or a chronic medical issue, often leading to symptoms such as dizziness, fainting, fatigue, and, in severe cases, shock.[62]

There are several factors that can lead to hypotension, and they can be broadly categorized into primary and secondary causes. Primary hypotension encompasses conditions where low blood pressure is the primary medical issue. Secondary hypotension, on the other hand, results from underlying medical conditions or external factors, such as dehydration, blood loss, severe infection, heart problems, endocrine disorders, and medication side effects.[57]

Low blood pressure can have a range of effects on the body. Common symptoms of hypotension include dizziness or light-headedness, fainting (syncope), blurred vision, fatigue, weakness, nausea, difficulty concentrating, and cold, clammy skin. In severe cases, hypotension can lead to shock, a life-threatening condition where there is inadequate blood flow to meet the body's needs[63]. A particular type of hypotension known as orthostatic hypotension occurs when blood pressure drops significantly upon standing up. It is often associated with conditions like dehydration, neurological disorders, or autonomic dysfunction.[64]

Hypotension, while less discussed than hypertension, is a medical condition that should not be underestimated. It can result from various causes, leading to a range of symptoms and, in severe cases, life-threatening complications. Understanding the underlying factors, recognizing symptoms, and timely management are key to addressing and mitigating the effects of low blood pressure, ensuring optimal cardiovascular health and overall well-being.

2.5. **Measuring Blood Pressure**

The accurate measurement of blood pressure is essential for diagnosis, monitoring treatment efficacy, and assessing an individual's overall well-being. Over the years, several techniques and instruments have been developed to measure blood pressure. In this section, we will explore and compare various blood pressure measurement techniques, shedding light on their mechanisms, advantages, and limitations. Blood pressure is measured in millimetres of mercury (mmHg) and recorded with the systolic number first, followed by the diastolic number. For example, a normal blood pressure would be recorded as 120/80 mmHg. Here are common healthcare ranges for blood pressure readings:

- **Hypotensive 'Low' Blood Pressure:** Systolic blood pressure below 90 mmHg and diastolic blood pressure below 60 mmHg.
- **Normal Blood Pressure:** A normal blood pressure reading is typically considered to be around 120/80 mm Hg.

- **Prehypertension:** This is a newer category introduced in some guidelines to identify individuals at risk of developing hypertension. It is defined as systolic blood pressure less than 140 mmHg and diastolic blood pressure less than 90 mmHg.
- **Hypertension Stage 1:** This stage is defined by systolic blood pressure between 140-160 mmHg or diastolic blood pressure between 90-100 mmHg.
- **Hypertension Stage 2:** This stage is diagnosed when systolic blood pressure is consistently 160 mmHg or higher, or diastolic blood pressure is consistently 100 mmHg or higher.

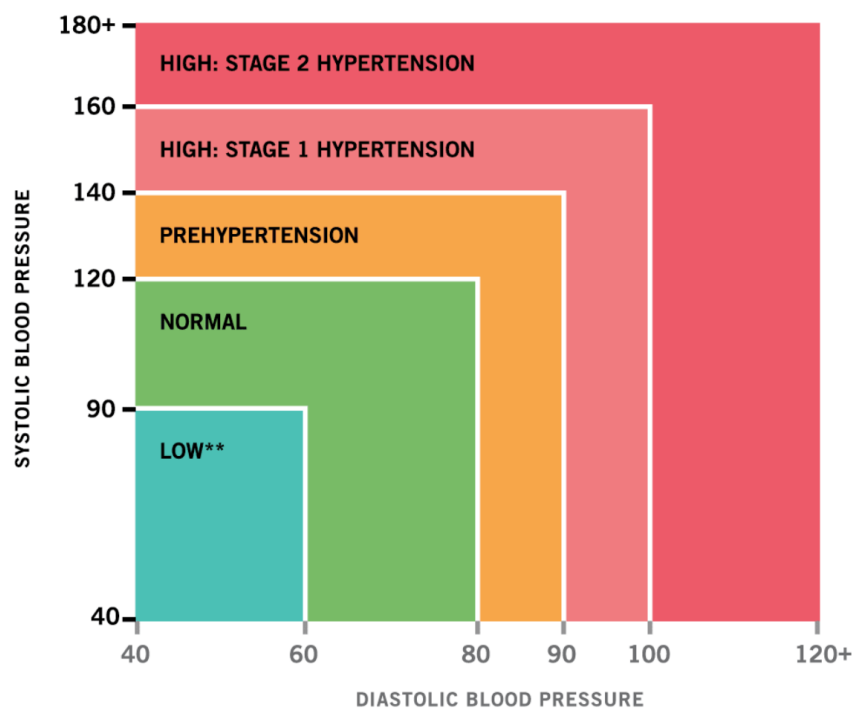


Figure 14 Blood pressure chart indicating the relevant ranges for each category of measurements.[65]

2.5.1. Established Methods

The sphygmomanometer is the most conventional form of blood pressure apparatus, and it can be considered the non-invasive gold standard in the health industry. Sphygmomanometers provide accurate and reliable readings when used correctly. These devices consist of several essential components and operate on a fundamental principle known as the auscultatory method. [66]

The cuff is typically made of fabric or rubber and is wrapped around the upper arm, positioned over the brachial artery. It is designed to temporarily occlude blood flow in the artery during the measurement process. The pressure gauge is connected to the cuff and measures the pressure within the cuff. The gauge may be an analogue mercury manometer or a digital display in modern devices. A stethoscope is used to listen to the Korotkoff sounds. The diaphragm of the stethoscope is placed over the brachial artery, which allows the healthcare professional or trained individual to listen to the sounds.

As the cuff pressure gradually exceeds the systolic blood pressure it begins to surpass the pressure within the artery. Blood is momentarily unable to flow through the artery, leading to its complete occlusion. At this point, the cuff pressure starts to decrease slowly.

As the cuff pressure falls below the systolic pressure, blood begins to flow through the partially constricted artery, producing turbulent blood flow. This turbulence generates distinctive sounds known as Korotkoff sounds, which can be heard through the stethoscope placed over the artery. The onset of these sounds corresponds to the systolic blood pressure, indicating that the pressure in the cuff has dropped below the pressure within the artery.

The cuff pressure continues to decrease, and the Korotkoff sounds change in character. The point at which the Korotkoff sounds disappear or return to a steady, less turbulent flow corresponds to the diastolic blood pressure.

Sphygmomanometers provide a highly accurate means of measuring blood pressure and are often used in clinical settings. The auscultatory method relies on the detection of Korotkoff sounds, and the trained ear is instrumental in obtaining precise readings. Proper cuff placement, inflation, and deflation are crucial for accurate results, making the sphygmomanometer a reliable tool in healthcare for diagnosing and monitoring blood pressure[66], [67]

Automated blood pressure monitors are commonly used in clinical settings and homes due to their convenience and accuracy. These instruments operate through one of the following methods:

Oscillometric Method: Automated monitors using the oscillometric method measure changes in the oscillations of arterial blood flow as the cuff pressure is gradually deflated. The monitor detects the systolic and diastolic pressures and displays the readings on a digital screen.[66]

Auscultatory Method: Some automated devices incorporate a stethoscope-like sensor that detects Korotkoff sounds, similar to the manual sphygmomanometer. However, instead of a human listener, the instrument electronically processes and records the sounds to determine blood pressure.[66]



Figure 15 Model demonstrating an automatic sphygmomanometer.[68]

2.5.2. Cuffless Methods

Sphygmomanometers have been the gold standard for non-invasive blood pressure measurement. However, they require the trained auscultatory technique, proper patient positioning, and cuff size selection. Over the past several decades, numerous research groups worldwide have devoted significant time and effort to develop non-invasive, cuff-less, and

continuous blood pressure monitoring[69]. The motivation behind this research is to replace current cuff-based blood pressure devices. Cuff-based devices often necessitate the presence of trained personnel, and they can cause irritation and inconvenience for patients due to cuff inflation and deflation. Furthermore, cuff-based methods do not offer continuous blood pressure measurements and are occasionally prone to inaccuracies. Consequently, existing clinical cuff-based blood pressure devices are not ideal for continuous blood pressure monitoring, which could play a significant role in early cardiovascular disease detection, among other applications. One approach to overcoming these challenges is the utilization of photoplethysmography (PPG). PPG finds wide application in healthcare, providing predictions for various vital health-related parameters. For example, PPG has been employed in determining heart rate, arterial stiffness, blood oxygen saturation, and blood glucose levels, as well as measuring blood pressure[70], [71]

Pulse Transit Time (PTT)

One approach for cuff-less non-invasive blood pressure (BP) measurements is Pulse Transit Time (PTT). PTT is defined as the time it takes for a pressure wave to travel between two arterial sites. An inverse proportional relationship between PTT and BP is often observed. PTT can be measured using two photoplethysmography (PPG) sensors placed on two distant sites on the body. This parameter is estimated as the time delay between the proximal and distal PPG waveforms. It's worth noting that in the literature, many papers refer to pulse arrival time as PTT; however, PTT is a less explored parameter [72]

Pulse Arrival Time

Pulse Arrival Time (PAT) is defined as the time interval between the electrical activation of the heart and the arrival of the pulse wave at a specific location on the body, such as the finger, toe, or forehead. In essence, PAT encompasses the sum of Pulse Transit Time (PTT) along with the ventricular electromechanical delay and the isovolumic contraction period, known as the Pre-ejection Period (PEP) delay. PEP can be influenced by factors such as stress, age, emotion, and movement.

The measurement of PAT necessitates the use of two sensors: an electrocardiogram (ECG) and a photoplethysmography (PPG) sensor. It's important to note that this method shares the same disadvantages mentioned in the PTT section. For example, PAT involves the use of two different sensors, ECG and PPG, each with different sampling rates. Both sensors are susceptible to motion artifacts, requiring signal processing, which can be intricate, particularly when continuous blood pressure monitoring is desired alongside intermittent measurements. Additionally, PAT, like PTT, necessitates calibration for different individuals.[73]

Pulse Wave Velocity

Another cuff-less method for blood pressure estimation is Pulse Wave Velocity (PWV). PWV represents the speed of pressure wave propagation in blood vessels and is based on the principles of wave propagation in elastic pipes. The fundamental idea behind this approach is that blood pressure can be inferred from the velocity of the heartbeat pulse[69].

PWV is determined by employing two photoplethysmography (PPG) sensors positioned on the same arterial branch, with a known distance separating them. The calculation of PWV is as follows: $PWV = D / PTT$, where D represents the length of the artery between the two reference points, and PTT is the pulse transit time

For instance, McCombie et al. [74] harnessed the relationship between blood pressure and arterial elasticity to derive blood pressure estimates using the PWV approach with two PPG signals. However, non-invasive PWV measurements pose several challenges. It requires measurements from two sensors, and arterial elasticity varies among individuals and is influenced by factors like age and diet. Additionally, the length of the artery necessary for the equation varies from person to person, necessitating frequent calibration due to the disparities in physiological parameters between individuals and the expiration of calibration over a short period. Furthermore, calibration procedures are not aligned with healthcare standards.

Machine Learning Algorithms

PPG signals carry a wealth of information about BP, embedded within various waveform features. These features, such as the amplitude of the PPG waveform, the timing intervals between specific points (e.g., systolic peak, diastolic notch), and the waveform's shape, serve as critical inputs for algorithms. Researchers often leverage these features in conjunction with regression models or machine learning techniques to estimate BP accurately [75], [76].

The use of machine learning algorithms has gained prominence in deriving BP from PPG signals. These algorithms are trained using PPG data in conjunction with simultaneously collected reference BP measurements. By considering a wide array of features extracted from PPG waveforms, such as pulse amplitude, pulse shape, and timing characteristics, machine learning models predict BP values with high precision. Machine learning approaches hold great promise for personal health monitoring, enabling individuals to access valuable BP data without the need for traditional cuffs [77].

While these methods show great promise, there are inherent challenges in deriving BP from PPG signals. Factors such as skin tone, ambient light, and motion artifacts can influence the accuracy of PPG-based measurements. Moreover, wearable devices and algorithms must undergo rigorous validation and calibration to ensure their reliability in clinical and real-world settings. Ongoing research aims to address these challenges, further enhancing the accuracy and accessibility of PPG-based BP estimation methods [78].

Conclusion

The chapter began with an in-depth overview of the anatomy and physiology of the cardiovascular system, highlighting the key roles of the heart, blood vessels, and the automatic regulation provided by the brain. This foundational knowledge is crucial for understanding the mechanisms behind blood flow dynamics and light propagation, both of which are essential components of PPG signal production.

The detailed discussion on the various types of blood vessels – arteries, veins, and capillaries – shed light on the complexities of blood flow throughout the body and its significance in the context of PPG research. Pathology was another critical area covered in this chapter, emphasizing the importance of blood pressure as a vital physiological parameter. The exploration of primary pathologies disrupting blood pressure balance, such as cardiovascular diseases, provided insights into how these conditions impact the cardiovascular system and influence PPG signals.

The chapter also delved into various methods for measuring blood pressure, highlighting their mechanisms, advantages, and limitations. This discussion was instrumental in understanding the traditional and novel approaches to blood pressure measurement and their relevance in PPG signal analysis.

This chapter offered a comprehensive understanding of the intricate relationship between blood pressure and PPG signals. The knowledge presented in this chapter forms a solid foundation for further research and development in the field of PPG, particularly in the pursuit of non-invasive, accurate, and calibration-free blood pressure monitoring methods. The insights gained here are not only pivotal for advancing PPG technology but also hold significant implications for improving cardiovascular health monitoring and diagnosis.

3

Principles of Photoplethysmography

3.1. INTRODUCTION	34
3.2. LIGHT TISSUE INTERACTION	35
3.2.1. ABSORPTION	36
3.2.2. SCATTERING	40
3.3. PRINCIPLES OF PHOTOPLETHYSMOGRAPHY	41
3.3.1. WAVEFORM CHARACTERISTICS	42
3.3.2. HISTORY OF THE PPG ORIGIN	47
3.4. PPG LIMITATIONS	47
3.5. PPG APPLICATIONS	49
CONCLUSION:	51

Introduction

3.1.

Photoplethysmography (PPG) is a non-invasive optical measurement technique that detects volumetric variations in blood within the peripheral circulation. This technology, first established in 1937, uses an infrared light source and a photodetector to measure various subcutaneous haemodynamic properties, with a rich history of clinical monitoring applications. The principle of PPG relies on a simple sensor transmitting and detecting light through a volume of tissue. During the cardiac cycle, blood vessels contain more blood in systole than in diastole, causing variations in the absorption of photons and resulting in the distinctive PPG waveform [70], [79].

The prominence of PPG in the medical field is attributed to two main factors: the accessibility and affordability of sensor components, and the robustness of its unobtrusive operation, which minimizes user error. These advantages have been pivotal in the recent expansion of the field, introducing innovative non-invasive techniques in physiological monitoring and vascular assessment [71]. The burgeoning interest in wearable technology has further propelled the use of PPG, leading to significant growth in consumer electronics that leverage this technology for health monitoring [80].

PPG's integration into wearable devices has revolutionized patient monitoring by enabling real-time, continuous tracking of vital parameters like blood oxygen saturation and heart rate, extending beyond traditional clinical settings. This advancement is particularly valuable in managing chronic conditions such as hypertension and cardiovascular diseases, necessitating regular monitoring [81].

Despite its apparent simplicity and non-invasive nature, PPG technology faces challenges related to signal accuracy and susceptibility to artifacts. Factors such as motion, skin tone variations, and ambient light conditions can substantially impact the reliability of PPG measurements. Addressing these challenges is a key area of ongoing research and development in the field[82], [83].

In addition to exploring the basic operational principles and established applications of PPG in modern medicine, this chapter will delve into the history of PPG to understand the true origin of the signal and the questions that still surround it. The interaction of light with biological tissues is a critical aspect of PPG, necessitating a thorough understanding of various properties of light. This chapter will discuss the relevant definitions, laws, and observations concerning the absorption, scattering, and refraction of light.

3.2.

Light Tissue Interaction

The study of light, a form of electromagnetic radiation, is fundamental in understanding photoplethysmography (PPG). Light's behaviour, governed by its physical properties such as wavelength, intensity, and polarization, directly influences its interaction with biological tissues. In the context of PPG, the way light traverses and interacts with skin and blood vessels is critical for accurate signal acquisition.

The interaction of light with matter is a complex phenomenon involving absorption, reflection, refraction, and scattering. When light encounters a material, some of its energy is absorbed, while the rest may be scattered or reflected. In biological tissues, these interactions are influenced by the properties of the tissue itself, such as composition and structure.[84]

3.2.1. Absorption

Absorption is a fundamental phenomenon in photoplethysmography (PPG) where light interacts with biological tissues, especially blood. When light, emitted from a source like an LED in a PPG sensor, penetrates the skin, it encounters blood vessels. Here, the light is partially absorbed by blood components, particularly haemoglobin. The extent of this absorption is not random but follows precise laws and principles, central among which is the Beer-Lambert Law[79].

The Beer-Lambert Law is pivotal in understanding how light absorption works in PPG. It describes the relationship between the concentration of an absorbing substance (in this case, blood components) and the intensity of light absorbed. According to this law, the amount of light absorbed by a medium is directly proportional to the concentration of the absorbing substance and the path length of the light through the medium. This relationship forms the basis for quantifying blood characteristics, such as oxygen saturation, in PPG measurements. As we delve deeper into absorption, understanding the Beer-Lambert Law will be crucial in interpreting how PPG devices measure and analyse physiological parameters.

Lambert's law states that the decrease in intensity of light passing through an absorbing medium is directly proportional to the intensity of the light itself. Mathematically, this relationship is expressed by considering the thickness x of the medium. The law is usually formulated as a differential equation, showing that the rate of decrease in light intensity I with respect to the thickness x is proportional to the intensity I at that point. This can be represented mathematically as:

$$-\frac{dI}{dx} \propto I$$

or,

$$\frac{dI}{dx} = -k_1 \cdot I$$

Eq. 3.1

Here, $\frac{dI}{dx}$ represents the rate of change of intensity I with respect to the thickness x , and k is the proportionality constant, often referred to as the absorption coefficient. This fundamental law is critical in understanding light behaviour in various mediums, including its application in photoplethysmography.

Integrating the left hand side between the minimum and maximum light intensity ($I = I_0$ and $I = I_t$), and the right hand side between the minimum and maximum pathlengths traversed by light ($x = 0$ to $x = d$), Eq. 3.1 reduces to:

$$\int_{I_0}^{I_t} \frac{dI}{I} = -k_1 \int_0^d dx$$

$$\Rightarrow \ln\left(\frac{I_t}{I_0}\right) = -k_1 \cdot d$$

Eq. 3.2

According to Beer's law, the light attenuation also depends on the concentration C of the attenuating species. Therefore, similar to Eq. 3.2, the decay in the intensity of light can be expressed as:

$$\ln\left(\frac{I_t}{I_0}\right) = -K \cdot d \cdot C$$

Eq. 3.3

In the equations, k_1 , and K are the proportionality constants.

In the general form of the Beer-Lambert law, the "absorbance" A of light passing through a medium containing a single type of absorber is defined as the product of the extinction coefficient ϵ , the concentration C of the absorbing species, and the optical path length d which is equivalent to the thickness of the absorbing medium. This relationship is typically expressed in the following manner.

$$A = \epsilon \cdot d \cdot C \quad \text{Eq. 3.4}$$

Through a few algebraic steps from Eqs. 3.3 and 3.4, the decay in the intensity of light traversing through a medium is expressed as:

$$I_t = I_0 e^{-A} = I_0 e^{-\epsilon \cdot d \cdot C} \quad \text{Eq. 3.5}$$

Transmittance T of light travelling through an absorbing medium is defined as the ratio between the transmitted and incident light intensity, that is, $= \frac{I_t}{I_0}$. From Eq. 3.4 and 3.5, therefore, the relationship between the transmittance and absorbance is obtained as:

$$A = -\ln(T) \quad \text{Eq. 3.6}$$

Equations 3.4, 3.5, and 3.6 are three commonly used expressions of the generic Beer-Lambert law.[79]

Biological tissue, composed of various absorbers like blood and melanin, and scatterers such as collagen, presents a complex, heterogeneous medium. The standard Beer-Lambert law, which does not account for scattering, is thus inadequate for biological applications. Recognizing this, Delpy and colleagues adapted the law to include scattering effects, making it applicable to near-infrared spectroscopy[85].

In an absorption only medium, the sample thickness equals to the optical pathlength ($l = d$). However, in a scattering-absorbing medium like tissue, the optical pathlength is not equal to the material thickness, rather related by a multiplicative term known as the "differential pathlength factor" DPF (i.e., $l = \text{DPF} \cdot d$). In this context, the optical path length in tissue is

determined not just by the sample thickness but is modified by the differential pathlength factor (DPF), a value greater than 1 indicating that the optical path in tissue exceeds the source-detector distance. The modified Beer-Lambert law incorporates this factor and a scattering-dependent parameter to define absorbance at a given wavelength. The modified Beer-Lambert law defines the absorbance (A) of light through a scattering & absorbing medium (i.e., tissue) at a certain wavelength (λ) using the following equation:

$$A_{\lambda} = \epsilon_{\lambda} \cdot l_{\lambda} \cdot C + G_{\lambda} = \epsilon_{\lambda} \cdot d \cdot DPF \cdot C + G_{\lambda}$$

Eq. 3.7

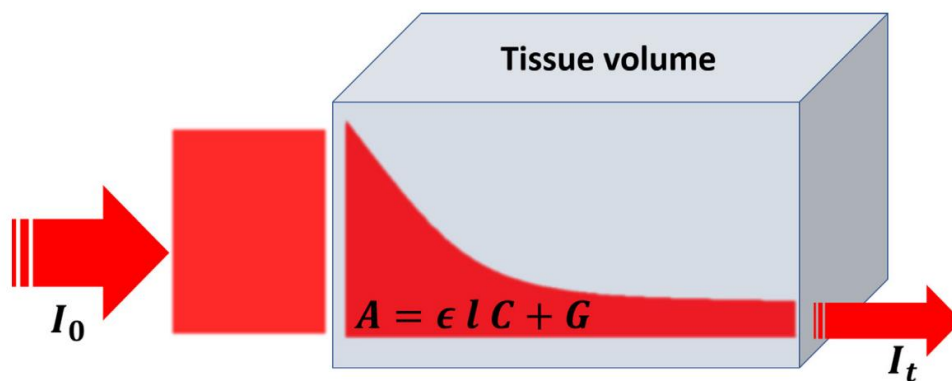


Figure 16 The Beer-Lambert law for PPG is visually depicted in a schematic where incident light intensity (I_0) undergoes exponential attenuation within the tissue (illustrated in red), resulting in a transmitted intensity (I_t). The law quantifies this attenuation as a function of the medium's extinction coefficient (ϵ), the optical path length (l), and the concentration (C) of the absorber in the tissue. Additionally, the term G represents a parameter that varies with the system.

where ϵ and C are the extinction coefficient and concentration of the absorber; d is the source detector separation; l is the optical pathlength; DPF is the “differential pathlength factor” and G is a scattering-dependent parameter (Hiraoka et al., 1993). A schematic is presented in Figure 16 The Beer-Lambert law for PPG is visually depicted in a schematic where incident light intensity (I_0) undergoes exponential attenuation within the tissue (illustrated in red), resulting in a transmitted intensity (I_t). The law quantifies this attenuation as a function of the medium's extinction coefficient (ϵ), the optical path length (l), and the concentration (C) of the absorber in the tissue. Additionally, the term G represents a parameter that varies with the system. to explain the exponential decay of light intensity through tissue using the modified Beer-Lambert law.

3.2.2. Scattering

Light scattering can be elastic or inelastic. This section will highlight elastic scattering which has major significance in PPG. In the elastic scattering, such as Rayleigh scattering and Mie scattering, the photon experience changes in direction without loss in energy of the scattered light whereas inelastic scattering, such as Raman scattering, occurs when there is an interaction that causes loss or gain of energy. Scattering is described by considering the incident light as a plane wave of uniform amplitude in any plane perpendicular to the direction of propagation with size scale larger than the scattering particles[86].

In Rayleigh scattering, the key criterion is the relative size of the scattering particles: they must be significantly smaller than the wavelength of the incident light, typically less than one-tenth. One of the hallmark characteristics of this scattering is its dependence on the wavelength of light. The scattering intensity is inversely proportional to the fourth power of the wavelength. This relationship, known as Rayleigh's scattering law, implies that shorter wavelengths, such as blue and violet, are scattered more efficiently than longer wavelengths like red. The scattering process is elastic, meaning that the scattered photons retain the same energy, and consequently the same wavelength and frequency, as the incident photons, but their direction is changed. This change in direction without an energy shift is a cornerstone of Rayleigh scattering[87], [88].

Mie scattering is integral in understanding photoplethysmography (PPG), especially when considering the interaction of light with various tissue components. In PPG, light often encounters particles such as blood cells, which are comparable in size to the wavelength of the light used. Unlike Rayleigh scattering, Mie scattering doesn't preferentially scatter certain wavelengths, leading to more uniform diffusion of light within the tissue[89].

3.2.3. Refraction

Refraction and reflection are phenomena of significant interest in photoplethysmography (PPG), as they crucially influence how light travels through the skin and underlying tissues. When light from a PPG sensor enters the skin, it transitions from a less dense medium (air) to

a denser medium (skin and tissue). This change in medium leads to refraction, a shift in the light's direction, governed by Snell's law:

$$v_1 \cdot \sin(\theta_1) = v_2 \cdot \sin(\theta_2)$$

Eq.3.8

Additionally, at each interface – air to skin, skin to subcutaneous layers, and within blood vessels – a portion of the light is also reflected. This reflection depends on the differences in refractive indices between the layers and the angle of incidence. The complex interplay of refraction and reflection is critical in understanding light behaviour in biological tissues.[88]

The tissue's heterogeneous structure, consisting of various layers each with distinct refractive indices, significantly influences how light is transmitted, bent, and reflected within it. As light from sources like PPG sensors penetrates the tissue, it undergoes multiple refractions and reflections at different tissue interfaces. This behaviour impacts the accuracy of optical diagnostic tools, affecting both the light's penetration depth and the path length. Reflections can lead to scattering and loss of light intensity, complicating the measurement and analysis process in applications like photoplethysmography.[88]

3.3.

Principles of Photoplethysmography

A typical PPG sensor is composed of a light source and a photodetector. The light emitted interacts with the tissue, undergoing reflection, refraction, scattering, and absorption. Variations in blood flow, induced by the cardiac cycle, alter the light's intensity, which is then detected by the photodetector. This concept forms the basis of photoplethysmography. PPG sensors operate in two modes: Transmission mode, where the light source and detector are on opposite sides of the tissue (used in devices like finger pulse oximeters), and Reflection mode, with both elements on the same side of the tissue, offering more flexibility in sensor placement. The modes are both illustrated in Figure 17. The red dotted lines represent the path of light from the source to the detector through the tissue[79].

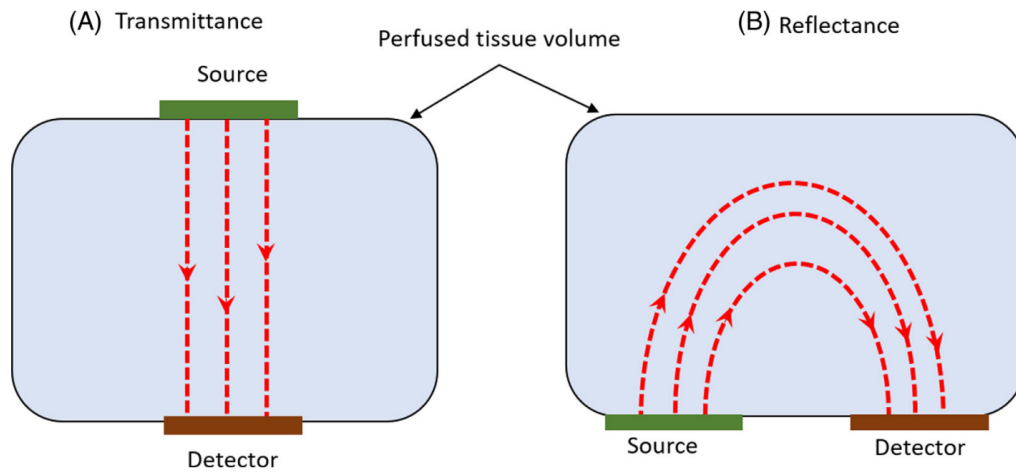


Figure 17 Diagram illustrating PPG techniques: (A) Transmittance; (B) Reflectance. This illustration depicts only the primary paths of photons that are eventually detected.[79]

3.3.1. Waveform Characteristics

The light intensity captured by the photodetector in PPG, whether in transmission or reflection mode, is the result of absorption, scattering, and reflection by various tissue components. Anatomical structures like bone, tissue, and venous blood mainly contribute to a consistent level of absorption, while the fluctuating aspect of the PPG signal is largely due to the pulsatile nature of arterial blood flow[90]. These are the two main components of the PPG signal:

- 1) The steady or non-pulsating part of the PPG signal, known as the 'DC PPG' component, is determined by the characteristics of the tissue through which the light travels. This component typically presents as a constant voltage offset in the signal. Its slow variations, with frequencies below 0.5 Hz, are primarily linked to physiological processes such as respiration, thermoregulation, and activities of the sympathetic nervous system.
- 2) The pulsatile 'AC PPG' component is synchronous to the heart rate and is often attributed to the changes that occur in arterial blood flow during the cardiac cycle. Typically, the AC PPG is considerably smaller in amplitude than the DC PPG and can be isolated with a bandpass filter (0.5 Hz to 20 Hz). The morphology of the AC PPG is indicative of cardiovascular haemodynamics.

- 2) The second 'Catacrotic' phase being the falling edge of the pulse, caused by the diastolic pressure and reflected waves from the periphery.

The anacrotic phase of the PPG waveform, beginning with a low point and culminating in the systolic peak, is largely influenced by the left ventricular ejection and the arterial compliance of the aorta. Various factors can impact the amplitude of the systolic peak. A decrease in blood volume, due to factors like the relative elevation of the measurement site or severe hypovolemia, can diminish the peak's amplitude. Similarly, local hypothermia or the use of vasoconstrictive drugs, such as Noradrenaline, which cause peripheral vasoconstriction, also lower the peak amplitude. Conversely, an increase in cardiac output or the use of anaesthetics leading to peripheral vasodilation can enhance the systolic peak amplitude.

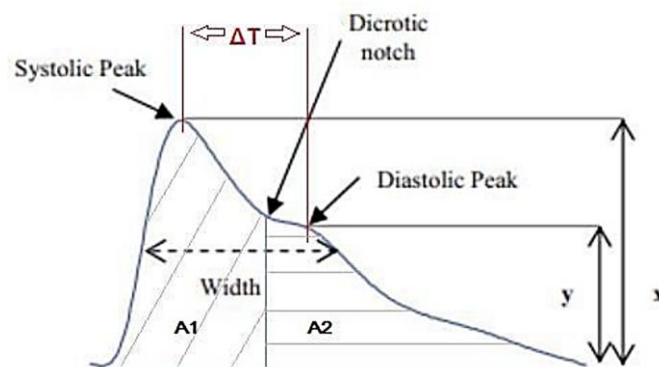


Figure 19 A PPG pulse and its common features.[92]

The main feature of the catacrotic phase is the diastolic peak which is caused by the reflections at the bifurcations of the arterial tree. The dicrotic notch is apparent in healthy subject with compliant arteries and is the most noticeable feature that changes with age. Studies have concluded that with increasing age the PPG waveform becomes more rounded with the diastolic peak reduced and the dicrotic notch less pronounced.

The following features have been described in literature and are the primary features extracted when analysing the PPG waveform [79], [92]:

1) Systolic Amplitude:

The signal's amplitude, measured from its base to the initial peak, serves as an indicator of the pulsatile changes in arterial blood volume. This amplitude is linked to stroke volume and is directly proportional to the local vascular distensibility.

2) Pulse Width:

The width of the signal taken at half the systolic amplitude. Awad et al suggests this correlates with systemic vascular resistance than systolic amplitude.[93]

3) Pulse Area:

The area under the PPG waveform. Pulse area has been found to reflect vascular tone changes.[94]

4) Inflection Point Area Ratio (IPA):

The area under the waveform is split into two at the dicrotic notch. Wang et al found that the ratio of the two areas can be indicative of total peripheral resistance [95]. It is defined as

$$IPA = \frac{A2}{A1}$$

Eq. 3.9

5) Peak to Peak Interval:

The distance between two systolic peaks. This interval is used to detect heart rate. The number of peaks in a period of time or the time between single peaks can be used to calculate heart rate.

6) Pulse Interval:

The distance between the start of the PPG waveform and its end. Often used when the systolic peaks are less clear. Lu et al found a strong correlation between pulse interval and ECG R-R intervals, strongly suggesting that for HRV, PPG signals could be an alternative measurement.[96]

7) Augmentation Index (AI) & Reflection Index (RI):

The AI & RI are ratios between systolic and diastolic peak amplitudes and relates the contribution the reflected waves make to systolic arterial pressure. Reduced elastic

artery compliance causes an early return of the reflected waves that cause a rise in the systolic peak. These indexes therefore relate directly to vascular dynamics.

$$RI = \frac{y}{x}$$

Eq. 3.10

$$AI = \frac{x - y}{x}$$

Eq. 3.11

8) Large Artery Stiffness Index (SI):

When using the finger as the site of measurement, the anacrotic phase arises mainly from the forward pressure wave produced by the left ventricle. The catacrotic phase arises mainly from the reflections that originate in the smaller arteries of the lower body, that travel back up to the aorta which then travels to the finger. The finger therefore is indicative of the forward and reflected waves. The time between the systolic and diastolic peaks is related to the transit time of pressure waves from the subclavian artery to the location of reflection and back to the subclavian artery. This pathlength is proportional to the patient's height (h). The formulated stiffness index by Millasseau *et al* was applied to PPG signals from different age ranges and proved that the SI increases with age [97].

$$SI = \frac{h}{\Delta T}$$

Eq. 3.12

The morphology of the PPG waveform is a rich source of physiological information, reflecting the intricate dynamics of the cardiovascular system. Its analysis, both in clinical and non-clinical settings, offers valuable insights into an individual's health status. As technology evolves, the potential applications of PPG waveform analysis continue to expand, promising to play a significant role in the future of health monitoring and diagnostics.

3.3.2. History of the PPG Origin

The origin of the photoplethysmography (PPG) signal is a subject of intricate detail and complexity. Initially, the PPG signal was understood as a reflection of blood volume changes within the tissue, as per the volumetric model. This model suggests that during systole, when blood volume in the arteries increases, there is greater light absorption, and during diastole, the reduced blood volume results in decreased light absorption. However, this explanation has been found to be an oversimplification [90].

Further studies, including Challoner's experiment in 1971, revealed that factors beyond mere volumetric changes contribute to the PPG signal [98]. This study showed that even when blood was pumped through a rigid glass tube, a PPG waveform was still detected, suggesting that changes in the orientation of erythrocytes (red blood cells) could influence the PPG signal. The orientation of erythrocytes changes during the cardiac cycle, leading to variations in light absorption along the light path.

Recent research has expanded the understanding of the PPG signal's origins. Various hypotheses have been proposed, including the impact of the mechanical properties of capillaries and the movement of erythrocytes in capillaries on the PPG waveform. Advanced computational simulations have provided deeper insights into the interaction of photons with tissue, contributing to a more comprehensive understanding of the PPG signal's origin [99],

3.4. [100], [101].

PPG Limitations

The effectiveness of PPG sensors is often challenged by several limitations that can impact their accuracy and reliability. A primary limitation of PPG sensors is their susceptibility to motion artifacts. Movement, especially common in wearable devices, can significantly distort the PPG signal. This distortion leads to inaccurate readings of heart rate, blood oxygen saturation, and other vital parameters [102]. The challenge lies in distinguishing the true physiological signals from those altered by movement, a task that often requires complex

algorithms and can limit the practicality of PPG sensors in active or uncontrolled environments.

Another notable challenge is the impact of ambient light. External light sources can interfere with the optical detection process of PPG sensors, leading to erroneous readings. This limitation is particularly problematic in environments with fluctuating light conditions, where the consistency of PPG measurements can be compromised[103].

The accuracy of PPG sensors also varies across different skin tones. This variation is due to the differing levels of melanin, which affects the absorption and reflection of the light used in PPG. Consequently, individuals with darker skin tones might receive less accurate measurements due to the higher melanin concentration in their skin, highlighting a need for calibration and adjustment in PPG technology to accommodate these differences[104].

Another limitation is the depth of penetration of PPG sensors. As they rely on optical methods, they can only measure from superficial blood vessels. This restriction limits the range of physiological parameters that PPG sensors can accurately measure[105].

Furthermore, PPG sensors can be less effective in situations of low or compromised perfusion. In conditions where blood flow is reduced or irregular, such as in patients with peripheral vascular disease or during hypothermic states, PPG sensors may struggle to obtain accurate readings[106]. This limitation underscores the necessity of considering circulatory dynamics when evaluating PPG sensor performance and the potential need for sensor adaptation in such scenarios.

The effectiveness of PPG sensors is highly dependent on their placement and the quality of contact with the skin. Inconsistent contact or inappropriate placement can lead to inaccurate readings, emphasizing the need for proper sensor design and user education.

PPG Applications

This section delves into the diverse applications of PPG, ranging from basic heart rate monitoring to advanced diagnostic and emerging novel uses, highlighting the technology's versatility and the challenges it aims to overcome.

Heart Rate and Pulse Oximetry Monitoring:

PPG has become a low-cost, non-intrusive modality for continuous heart rate monitoring. Its integration into a variety of wearable devices like smartphones and smartwatches has made it accessible for widespread use. The technology is not limited to heart rate monitoring; it also plays a critical role in arterial blood oxygen saturation (SpO₂) estimation through pulse oximetry. SpO₂, a measure of oxygen saturation in arterial blood, is crucial in assessing a patient's respiratory function and is typically measured using PPG [107], [108], [109].

Advanced Diagnostic Applications:

Beyond basic monitoring, PPG is employed for advanced diagnostic applications. It can be used to assess cardiac function, arterial stiffness, autonomic nervous system responses, and even detect apnoea [110]. Heart rate variability (HRV), a metric derived from PPG, provides insights into the interaction between the brain and cardiovascular system. Other hemodynamic parameters, like augmentation index (AIx) and pulse wave velocity (PWV), key markers of arterial stiffness, can be estimated through PPG analysis [111].

Emerging applications

Emerging applications of Photoplethysmography (PPG) are expanding the technology's horizon, demonstrating its versatility beyond traditional clinical settings. These new applications harness PPG's ability to non-invasively measure blood volume changes in the microvascular bed of tissue, offering insights into various physiological parameters:

- **Mental Health Monitoring:** PPG is being explored for its potential in monitoring mental health, especially stress and anxiety levels. By analysing heart rate variability (HRV) derived from PPG signals, it's possible to gain insights into the autonomic nervous system's state, providing valuable data for the assessment of emotional and mental well-being.[112]

- **Sleep Analysis:** PPG is increasingly used in sleep monitoring devices to track sleep patterns, quality, and disturbances. This application is particularly valuable in diagnosing and managing sleep disorders like sleep apnea, where PPG can help monitor changes in blood oxygen levels and heart rate during sleep.[113]
- **Hydration Status Monitoring:** Emerging research suggests PPG could be used to monitor hydration status. Changes in blood volume and flow, as detected by PPG, can be indicators of hydration levels, potentially offering a non-invasive method to monitor fluid balance in the body.[114]
- **Early Detection of Sepsis:** In clinical settings, PPG technology is being investigated for early detection of sepsis. By continuously monitoring changes in blood perfusion and oxygenation, PPG could provide early warning signs of this potentially life-threatening condition.[115]
- **Chronic Disease Management:** In diseases like diabetes and hypertension, continuous monitoring of physiological parameters via PPG can aid in better disease management. For instance, changes in PPG signals could help in monitoring vascular health in diabetic patients.[116]
- **Fitness and Performance Monitoring:** In sports and fitness, PPG is used to assess physical performance and recovery. By tracking heart rate and blood oxygenation during exercise, PPG provides athletes and fitness enthusiasts with data to optimize their training routines.[117]
- **Augmenting Telehealth Services:** With the rise of telemedicine, PPG is becoming an integral part of remote patient monitoring systems, offering a convenient way for healthcare providers to track patients' vital signs remotely.[118]

Despite its widespread use, PPG technology faces challenges, particularly in the accuracy and reliability of data, especially in diverse and dynamic real-world conditions. This limitation underscores the vital nature of further research in this field.

This is where *in vitro* work using phantoms – artificial models that simulate human tissue – becomes crucial. Phantoms offer a controlled environment to study the interactions between light and tissue, allowing researchers to systematically vary parameters and observe the

effects on the PPG signal. This method can lead to a deeper understanding of the nuances of PPG signal formation and propagation.

Conclusion:

Photoplethysmography has already established itself as a versatile and valuable tool in both clinical and non-clinical applications. Its expansion into new areas of health monitoring and its integration into wearable technology signify its growing importance. However, the full potential of PPG can only be unlocked through continued research, particularly focusing on in vitro studies using phantoms. These studies will pave the way for more accurate, reliable, and diverse applications of PPG, further embedding this technology in the fabric of healthcare and beyond.

4

Phantom Technologies

4.1.	INTRODUCTION.....	52
4.2.	TYPES OF PHANTOMS	53
4.3.	DESIGN CONSIDERATIONS FOR PHANTOMS.....	56
4.4.	ADVANCEMENTS IN PHANTOM TECHNOLOGIES	63
4.5.	APPLICATIONS OF PHANTOMS IN PPG RESEARCH	64
4.6.	LIMITATIONS AND CHALLENGES IN PHANTOM RESEARCH	66
	CONCLUSION.....	67

Introduction

4.1. At its core, a phantom is a meticulously crafted replica of biological tissues, such as skin, muscle, and blood vessels. These artificial constructs faithfully replicate the behaviour of light when it interacts with human tissue, making them invaluable for experimentation. Phantoms are engineered to replicate the properties of real human tissue. This means they can scatter and absorb light in a manner like our skin and underlying structures. Phantoms can also mimic the mechanical properties, such as elasticity, of human tissues, allowing researchers to recreate conditions that closely resemble the human body[119], [120].

In clinical and research settings, it's essential to standardize PPG measurements for consistency and comparability. Phantoms facilitate the calibration of PPG sensors, ensuring that measurements are reliable and consistent across different devices and laboratories.

The use of phantoms is paramount in PPG research for several reasons. First and foremost, they provide a controlled environment for experimentation, eliminating the variability associated with human subjects [121]. Researchers can precisely manipulate factors like tissue composition, blood flow rates, and blood pressures to gain deeper insights into PPG signal characteristics[122]. Phantoms offer the flexibility to create scenarios that might be ethically or practically challenging to replicate with human subjects. For example, researchers can simulate extreme conditions or pathological states to study their effects on PPG signals.

Throughout this chapter, we will delve deeper into the various types of phantoms, their design considerations, and their applications in PPG research. By understanding the role of

phantoms in this context, we can appreciate how these artificial models contribute significantly to the advancement of PPG technology and its applications in healthcare and beyond.

Types of Phantoms

The use of phantoms in medical research is not a new concept. Historically, phantoms were developed for radiology and imaging disciplines, where the need to calibrate and standardize equipment without exposing humans to unnecessary risks was evident[123]. The earliest phantoms were simple, often just geometric shapes made of uniform materials. Over time, as the complexity of medical imaging and sensing technologies grew, so did the sophistication of phantoms. Today's phantoms can exhibit highly detailed and varied properties, ranging from basic optical phantoms for calibrating sensors to advanced models that mimic the dynamic behaviour of human tissues.

The use of phantoms in the medical field is diverse and multifaceted, catering to various applications ranging from imaging to therapy. Here, we categorize these phantoms based on their primary uses and characteristics:

Radiological Phantoms

Radiological phantoms are vital in the domain of imaging. Designed to mimic the response of human tissues to different imaging modalities like X-rays, MRI, and CT scans, these phantoms are indispensable for calibrating imaging devices and ensuring accurate diagnostics. Simple geometric phantoms, often comprising homogenous materials, serve as the foundation for basic calibration. However, the complexity of human anatomy necessitates more sophisticated models. Anthropomorphic phantoms, for instance, replicate the intricacies of bone, muscle, and organ structures. These advanced models are crucial not only for equipment calibration but also for optimizing radiation doses and training radiologists, thus playing a significant role in both safety and education [124].

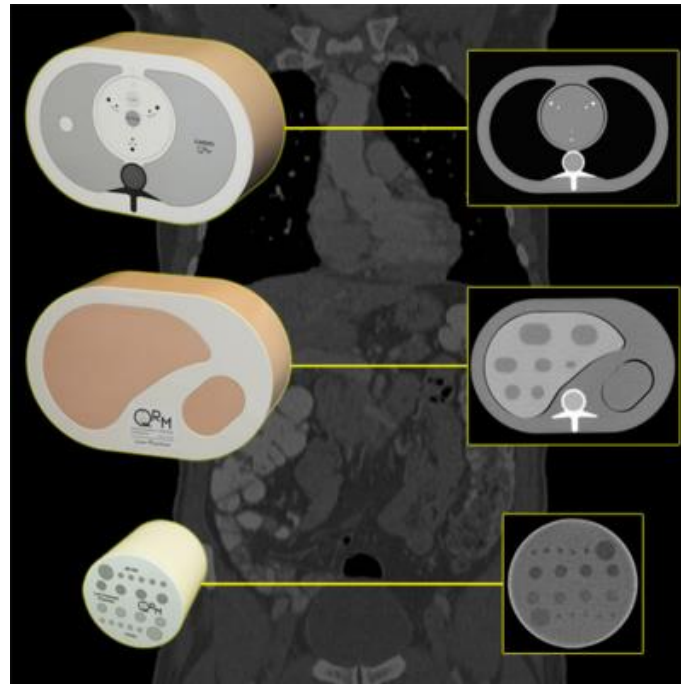


Figure 20 Phantoms for measuring coronary artery calcification, liver lesions and low contrast capability of CT scan protocols. [125]

Ultrasound Phantoms

In ultrasound imaging, phantoms that simulate the acoustic properties of human tissues are essential. Basic tissue-mimicking phantoms are routinely used for testing and calibrating ultrasound machines. More advanced versions, equipped with Doppler flow capabilities, emulate blood flow, thereby facilitating the training and testing of Doppler ultrasound techniques [126], [127], [128]. These phantoms are instrumental in the calibration of ultrasound devices and the training of sonographers, ensuring that ultrasound imaging remains a reliable diagnostic tool.



Figure 21 deal flow phantom for Doppler and color Doppler flow research and development applications. [129]

Optical Phantoms

Optical phantoms are designed to mimic the light absorption and scattering properties of biological tissues. These are particularly crucial in technologies like photoplethysmography (PPG), near-infrared spectroscopy (NIRS), and other optical sensing methods. The phantoms range from basic tissue-simulating models, used in the development and calibration of optical diagnostic tools, to more complex dynamic flow phantoms that incorporate fluid movement to simulate blood circulation [120], [130], [131], [132]. This latter type is vital for testing dynamic optical measurements and for research that delves into the interactions between light and living tissues.

Therapeutic Phantoms

In therapeutic settings, particularly radiation therapy, phantoms simulate patient responses to various treatments [133], [134], [135]. Static phantoms are used for basic dosimetry and equipment calibration, while dynamic phantoms, which can simulate physiological movements like breathing, are essential in assessing the efficacy of treatments under realistic conditions. These phantoms are central to the planning and optimization of radiation therapy treatments, ensuring that doses are accurately and safely delivered to patients.

Training and Surgical Phantoms

Phantoms used for medical education and surgical training provide a safe, realistic environment for learning and practicing medical procedures. Basic training phantoms allow for simple procedural practice like injections or suturing [136], [137]. More complex surgical phantoms, replicating specific anatomical regions, are used for advanced surgical training, sometimes incorporating haptic feedback to enhance the learning experience [138], [139]. These phantoms are widely employed in medical schools and training programs, playing a critical role in hands-on practice and procedural learning [140].

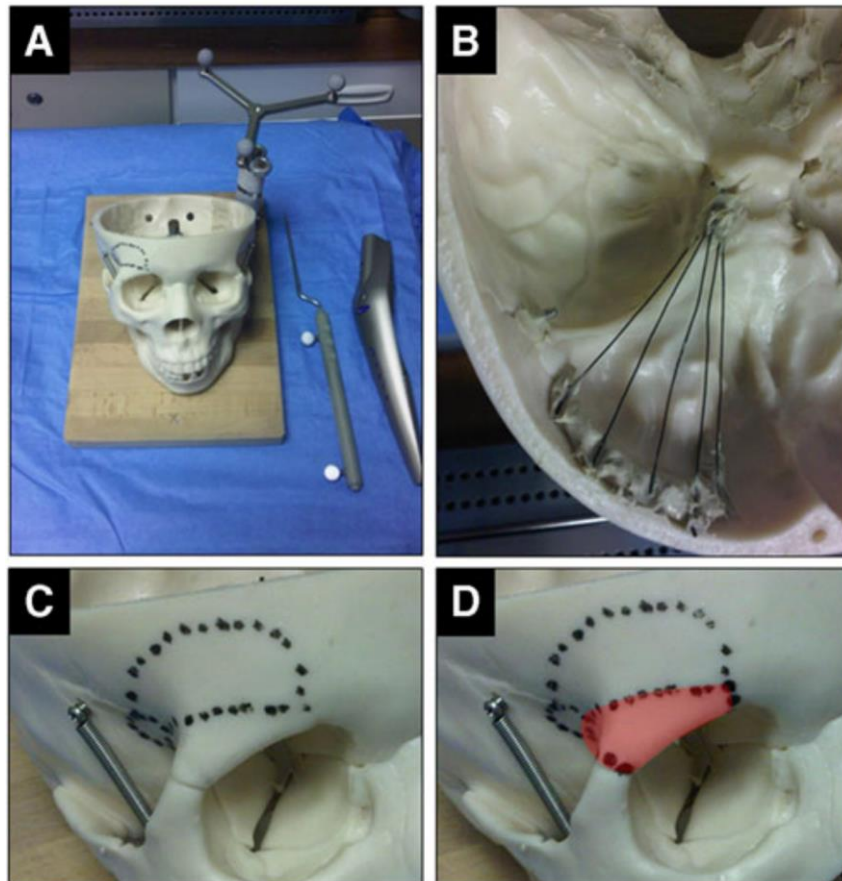


Figure 22 Simulation of the eyebrow craniotomy and surgical corridor using a surgical phantom. [139]

Hybrid and Specialized Phantoms

Finally, the category of hybrid and specialized phantoms encompasses models designed for unique research needs or advanced medical applications. Patient-specific phantoms, often created using 3D printing technology, are tailored to individual patient anatomy, playing a significant role in personalized medicine[136]. Multimodality phantoms combine features of different types, proving useful in integrated imaging systems and advanced diagnostic

4.3. research.

Design Considerations for Phantoms

This section thoroughly examines the key design aspects of PPG phantoms, drawing on recent studies to inform on material selection, optical and mechanical properties, geometry, and vasculature.

4.3.1. Materials: Silicone vs Gelatine

In the realm of PPG phantom design, the choice of material is foundational [120]. Silicone emerges as a robust option, celebrated for its longevity and consistency, which are essential for devices used over extended periods. Its ability to be fine-tuned for specific mechanical and optical properties allows for a wide array of applications, crucial for replicating different skin types and conditions. However, silicone's higher cost and complex processing requirements pose challenges, alongside its potential limitations in biochemical interaction simulation.

On the other hand, gelatine offers an economically viable alternative, with its high biological fidelity closely mimicking human tissue's optical and mechanical properties. Its ease of manipulation and modification makes it a practical choice for varied research settings. Yet, gelatine is not without its drawbacks, including environmental sensitivity and batch-to-batch variability, which can impact the reproducibility and standardization of experiments.

Table 2: Comparative Analysis of Gelatine-Based and Silicone-Based Phantoms in PPG Applications. This table outlines key characteristics of gelatine and silicone when used in the fabrication of photoplethysmography (PPG) phantoms, highlighting their respective durability, cost, biological fidelity, customizability, processing requirements, stability, optical properties, and mechanical properties. The comparison serves to inform material selection based on specific requirements and objectives in PPG phantom development. [119], [120], [124], [127]

Characteristic	Gelatine-Based Phantoms	Silicone-Based Phantoms
Durability	Less durable; susceptible to degradation and environmental factors such as temperature and humidity. (degrades over days to weeks, environmentally sensitive)	Highly durable; maintains properties over time, suitable for long-term use. (remains stable for months to years, resistant to environmental factors)
Cost	Generally, more affordable and readily available, making it a cost-effective choice for laboratory use.	More expensive, with potentially higher costs for processing and fabrication.
Biological Fidelity	High biological fidelity due to its water content and texture, closely resembling human tissues.	May not fully capture certain biochemical interactions of biological tissues.
Customisability	Easily modifiable with additives to simulate various conditions; however, batch-to-batch variability can be an issue.	Offers customizable mechanical and optical properties, allowing for diverse applications and simulations.
Processing and Fabrication	Easier to prepare and mold in laboratory settings but may lack consistency in properties.	Requires more sophisticated processing techniques, which can be a limiting factor in certain settings.

Stability and Consistency	Environmental sensitivity can affect consistency, leading to variability in long-term studies.	Exhibits high consistency in production, essential for standardizing experiments and calibrations.
Optical Properties	Can be adjusted with additives to mimic human tissue optical properties but may not be as stable over time.	Optical properties can be finely tuned, making it versatile for simulating different skin types and optical conditions.
Mechanical Properties	Can closely mimic the mechanical properties of human tissues but may degrade over time, affecting its mechanical fidelity.	Adjustable mechanical properties, including elasticity and hardness, suitable for a wide range of tissue simulations.

4.3.2. Mechanical Properties:

The mechanical properties of materials used in photoplethysmography (PPG) phantoms are vital for accurately simulating not only the general characteristics of human tissue but also specific pathophysiological conditions, particularly those affecting the cardiovascular system. The hardness of a PPG phantom, often determined by the material's Young's modulus, directly influences how the phantom responds to pressure applied by PPG sensors. This response is a key factor in simulating the mechanical properties of human tissues, especially the skin and underlying vascular structures.

Soft phantoms, which simulate more elastic and compliant tissue akin to more popular PPG measurement sites, allow for greater deformation under sensor pressure. This deformation can lead to variations in the sensor-skin contact area, potentially affecting the light penetration and, consequently, the PPG signal.

The mechanical properties of photoplethysmography (PPG) phantoms, particularly those made from silicone and gelatine, are fundamental in simulating the biomechanical behaviour of human tissues. Both materials offer unique attributes and challenges in replicating tissue properties, which are crucial for accurate PPG signal analysis. Here is how mechanical properties can be tailored in silicone and gelatine-based phantoms to enhance their efficacy in PPG applications [120], [141]:

Silicone-Based Phantoms

Silicone, owing to its versatility and durability, is a popular choice for creating PPG phantoms with specific mechanical properties.

- **Adjusting the Silicone Composition:** The mechanical properties of silicone can be fine-tuned by varying the ratio of the base polymer to the curing agent. Changing this ratio alters the cross-linking density within the silicone, which can significantly impact its elasticity and stiffness. A higher concentration of curing agent typically leads to a stiffer material, simulating conditions like arterial stiffness.
- **Incorporating Additives:** To further tailor the mechanical properties, different additives can be introduced into the silicone mixture. For instance, adding certain types of oils can increase flexibility, while incorporating micro-fillers or fibres can enhance strength and mimic the anisotropic nature of biological tissues.
- **Controlled Curing Process:** The curing process and conditions (such as temperature and humidity) also play a role in defining the final mechanical properties of the silicone phantom. Controlled curing can help achieve consistent and repeatable mechanical characteristics.

Gelatine-Based Phantoms

Gelatine is another widely used material in PPG phantom fabrication, favoured for its biological similarity to human tissues.

- **Concentration Variability:** The mechanical properties of gelatine phantoms are primarily influenced by the concentration of gelatine in the mixture. Higher concentrations result in stiffer phantoms, which can be used to simulate less compliant tissues or pathological conditions.
- **Thermal Processing:** The temperature and duration of the heating process during gelatine preparation can affect the strength and elasticity of the final phantom. Precise thermal control is necessary to ensure consistent mechanical properties.
- **Cross-linking Agents:** The introduction of cross-linking agents to the gelatine mixture can enhance its mechanical stability and longevity. These agents can create stronger bonds within the gelatine, increasing its resistance to deformation and degradation.
- **Addition of Other Components:** Incorporating other substances, such as glycerol or agar, can modify the mechanical properties of gelatine. Glycerol, for example, can

increase the flexibility and moisture retention of the phantom, while agar can add firmness.

The design of mechanical properties in silicone and gelatine-based PPG phantoms is a sophisticated process that requires careful consideration of material composition, additives, and processing techniques. By precisely controlling these factors, researchers can create phantoms that closely mimic the mechanical behaviour of various human tissues under different physiological and pathological conditions[142]. These tailored phantoms are invaluable in the development and calibration of PPG devices, contributing significantly to advancements in non-invasive diagnostic technologies.

4.3.3. Geometry

The geometric design of photoplethysmography (PPG) phantoms is a critical aspect that significantly impacts the accuracy and effectiveness of PPG simulations. The detailed replication of tissue layers in terms of thickness, texture, and density ensures that the interaction of light with the phantom closely resembles that with actual human tissue, which is vital for reliable PPG signal analysis. Furthermore, replicating the complex anatomical features of areas where PPG sensors are commonly applied, such as the wrist or finger, is crucial. These specific contours and structures must be accurately mirrored in the phantom design to ensure a realistic sensor-phantom interaction.

However, the design process faces challenges, including striking a balance between the need for standardized models and accommodating individual anatomical variability. Creating phantoms that can adapt to a range of anatomical differences is key for their broad applicability in PPG research and clinical use [143]. Additionally, manufacturing constraints, particularly in advanced techniques like 3D printing, pose limitations in terms of resolution and material properties, which can affect the geometric accuracy of the phantoms.

Recent advancements in phantom design have seen the application of 3D printing technology to create customized models that accurately mimic specific patient anatomies [136]. This approach is particularly beneficial for developing phantoms used in testing wearable PPG

devices, ensuring compatibility with variations in human anatomy. Moreover, research focusing on the optical properties of different skin layers has led to the development of multi-layered phantoms. These models not only replicate the structural complexity of human skin but also provide valuable insights into the contribution of each layer to the overall PPG signal [132], [141], [144].

In conclusion, the geometric design of PPG phantoms is a pivotal element in their development, demanding precision and careful consideration. Advances in fabrication technologies are facilitating more accurate and customized designs, enhancing the realism and effectiveness of these phantoms. As PPG technology continues to evolve, the role of accurately designed phantoms remains crucial in the development and application of non-invasive physiological monitoring devices.

4.3.4. Vasculature

The design of the vascular system in PPG phantoms is not just about replicating the appearance of blood vessels but also their functional attributes. Accurately mimicking the pulsatile nature of human arteries and veins is particularly critical. This involves creating phantoms with vascular channels or tubes that can simulate the rhythmic expansion and contraction of vessels as blood flows through them. This feature is vital for testing PPG sensors in conditions that closely resemble physiological blood flow, where the dynamics of pulsatile pressure play a significant role in the quality and interpretation of PPG signals.

Moreover, the mechanical properties of these artificial vessels, such as their ability to expand and contract in response to varying pressures, are key factors in the design process. This aspect is crucial in creating phantoms that can mimic the response of human vascular systems under different physiological and pathological states, such as hypertension or arterial stiffness. By replicating these conditions, phantoms can provide a more comprehensive testing environment for PPG devices, ensuring their accuracy and reliability in real-world applications.

While there have been notable advancements in phantom technology, current research projects face significant limitations, particularly in the replication of the elastic properties of human vasculature. A primary challenge lies in the use of commercially available silicone tubing. This tubing often exhibits a high Young's modulus, indicating a stiffness that does not accurately represent the flexibility of human blood vessels [122], [141]. Additionally, the wall thickness of this tubing is typically greater than that of human vessels, further deviating from physiological accuracy.

Some projects have attempted alternative approaches, such as casting micro-tunnels directly within the phantoms, which allows for the creation of micro-meter scale vessels. This method shows promise in mimicking the finer aspects of the vascular network [145]. However, these fabricated vessels still face challenges in replicating the dynamic mechanical properties of human vasculature, particularly under pulsatile flow conditions that simulate human blood pressure.

So far, these projects have not been able to achieve a pulsatile flow that accurately reflects the range and rhythm of human blood pressures. Additionally, the mechanical properties of these artificial vessels, such as their compliance and response to varying pressures, often do not match those of natural human vessels. This discrepancy poses a significant hurdle in creating phantoms that can reliably mimic human vascular behaviour, especially under different physiological and pathological states.

The ongoing research in this field is crucial, as overcoming these limitations will enhance the realism and applicability of PPG phantoms. Achieving a closer match to the mechanical properties of human blood vessels will significantly improve the testing and validation of PPG devices, ensuring their effectiveness in real-world diagnostic and monitoring applications.

Advancements in Phantom Technologies

The field of photoplethysmography (PPG) has seen significant advancements in phantom development, driven by the need for more accurate and diverse simulations of human physiological conditions. Recent innovations in PPG phantom development are not just enhancing the realism of these models but also expanding their capabilities in replicating complex biological processes. This section highlights some of the cutting-edge techniques and materials being employed in the latest PPG phantom development.

Multi-Layered Phantoms

Recent developments have seen a shift towards the creation of multi-layered phantoms that more accurately represent the stratified structure of human skin and underlying tissues. These phantoms use a combination of different materials to mimic the varying properties of the epidermis, dermis, and hypodermis, along with the embedded vascular network.

Each layer in these phantoms can be designed to have specific optical and mechanical properties, aligning closely with those of natural human tissues. This approach is particularly beneficial in studying how light interacts with multi-layered tissues in PPG analysis [132], [144].

Integration of Dynamic Blood Flow Systems

Incorporating dynamic systems that simulate blood flow within the phantom is a notable advancement. These systems use fluidic channels or tubes, often made from flexible materials to mimic blood vessels with pulsatile flow. By incorporating microfluidic systems or piezo-electric actuators, phantoms can now simulate the pulsatile flow of blood. This feature is crucial for testing PPG sensors under more realistic physiological conditions, where blood flow dynamics play a significant role [122]. Advanced phantoms allow for the adjustment of flow rates and pressure within the simulated vessels, enabling studies under various physiological and pathological states, such as hypertension or arterial stiffness.

Use of Smart and Responsive Materials

The application of smart materials, which respond to external stimuli like temperature, pH, or electromagnetic fields, is an exciting area in phantom development [146], [147]. These materials can change their properties in response to temperature variations, enabling the simulation of thermoregulation or inflammatory responses in human tissues. Materials that respond to electrical stimuli can be used to simulate muscle contractions or changes in tissue properties due to electrical activity, adding another layer of realism to the phantoms.

3D Printing and Custom Fabrication

3D printing technology has revolutionized the way PPG phantoms are created, allowing for precise and customizable fabrication. 3D printing enables the creation of phantoms with complex anatomical structures, tailored to specific research needs or diagnostic scenarios.

With advances in 3D printing, a wide range of materials can be used, including hydrogels, photopolymers, and composites, each contributing different properties to the phantom [137], [148], [149].

The recent advancements in PPG phantom development are a testament to the evolving landscape of biomedical engineering and medical diagnostics. These sophisticated phantoms, with their enhanced realism and dynamic capabilities, are not only pivotal in the advancement of PPG technology but also play a crucial role in the broader field of non-invasive physiological monitoring and diagnostic research. As these technologies continue to mature, they promise to offer even more precise and versatile tools for healthcare and medical

4.5. research.

Applications of Phantoms in PPG Research

Phantoms may play a vital role in the field of photoplethysmography (PPG), offering essential tools for various key applications including sensor validation, noise reduction, signal enhancement, calibration, and standardization. Their versatile use significantly contributes to

the advancement of PPG technology, as they provide controlled environments for testing and research.

In the realm of sensor validation, phantoms are particularly instrumental [150]. They offer a controlled setting where the accuracy and performance of PPG sensors can be thoroughly assessed. For instance, through the use of multi-layered silicone phantoms, researchers can simulate different skin types and vascular conditions to evaluate how well PPG sensors capture blood flow and volume changes. This type of testing is crucial for determining the sensitivity and specificity of sensors. An example of this application was demonstrated in a study where a multi-layered silicone phantom was used to test the accuracy of a new PPG sensor, revealing its precision and reliability in detecting subtle changes in blood volume[151].

Phantoms also play a critical role in isolating and understanding noise sources in PPG signals, which is key to signal enhancement. By simulating conditions like motion artifacts or varying ambient light, phantoms enable researchers to pinpoint specific noise sources that may affect PPG readings. This capability is vital for developing algorithms and sensor designs that improve the signal-to-noise ratio, enhancing overall signal quality. A notable research effort in this area involved using a phantom to simulate motion artifacts in PPG signals, leading to the development of an algorithm that effectively filtered out the noise for clearer PPG readings [152].

Calibration and standardization of PPG measurements are other crucial areas where phantoms prove indispensable. They provide benchmarks for calibrating PPG devices, ensuring consistent and accurate readings across different units and setups. In clinical and research settings, phantoms help maintain standardized methodologies for PPG measurements, promoting comparability and reproducibility of results.

Limitations and Challenges in Phantom Research

While phantoms are invaluable tools in photoplethysmography (PPG) research, their use is not without limitations and challenges. Understanding these constraints is crucial for 4.6. advancing the field and for the accurate interpretation of PPG data obtained from phantom studies.

One of the primary challenges in phantom development is the trade-off between achieving high accuracy and managing the complexity of the phantom. Highly accurate phantoms that meticulously replicate human tissue properties can be extremely complex to design and fabricate. This complexity often involves sophisticated materials and intricate fabrication processes, which can be time-consuming and costly. For instance, creating a phantom that accurately mimics the layered structure of human skin, complete with realistic vascular networks and variable tissue properties, requires significant expertise and resources. While these high-fidelity phantoms offer detailed insights, their complexity can limit their widespread use and practicality, especially in routine testing or educational settings.

Another significant challenge is the inherent variability in human tissue properties. Human tissues exhibit a wide range of characteristics due to factors like age, ethnicity, health status, and individual physiological differences[153], [154]. Accurately replicating this diversity in phantoms is a daunting task. Phantoms typically represent an averaged or standardized model of human tissue, which may not capture the nuances of individual variability. This limitation can impact the generalizability of the findings obtained from PPG studies using phantoms, as they might not fully represent the range of conditions encountered in clinical practice.

The validity of phantoms as models for human tissues is another crucial consideration. Ensuring that phantoms accurately replicate the properties they are intended to simulate requires rigorous validation. This validation process often involves comparing the phantom's properties with real human tissues under various conditions and ensuring that they respond similarly. The process can be complex and requires a multidisciplinary approach, combining

expertise in materials science, biomedical engineering, and clinical knowledge. Without thorough validation, there is a risk that the phantoms might not provide reliable or relevant data for PPG research.

Conclusion

This chapter has comprehensively examined the crucial role of phantoms in photoplethysmography (PPG) research. We have explored their diverse applications in sensor validation, noise reduction, signal enhancement, calibration, and standardization. These applications underscore the indispensable nature of phantoms in refining and advancing PPG technology. Case studies highlighted throughout the chapter demonstrate the practical impact of phantoms in enhancing the reliability and accuracy of PPG measurements.

Advancements in phantom development, including the use of multi-layered structures, dynamic blood flow simulation, and innovative materials like smart composites, mark significant strides in the field. These advancements are pivotal in creating more realistic and versatile phantoms that closely mimic human physiological and pathological conditions.

However, the chapter also addressed the inherent limitations in phantom design and application. Challenges such as balancing accuracy with complexity, replicating the diversity of human tissues, and ensuring rigorous validation of phantoms are crucial areas for ongoing research and innovation.

In conclusion, while phantoms are invaluable in PPG research for their ability to simulate various aspects of human physiology, attention to their limitations is essential. Addressing these challenges will be key in further harnessing the potential of phantoms to improve PPG technologies and their applications in non-invasive medical diagnostics.

5

Development of Measurement Systems

5.1	INTRODUCTION	68
5.2	BASIC PROBES	69
5.3	DYNAMIC PPG SYSTEM (DPPGS)	71
5.3.1	DPPGS VERSION ONE.....	71
5.3.2	DPPGS VERSION TWO.....	73
5.4	PPG PROCESSING AND ACQUISITION SYSTEM	77
	SUMMARY	79

5.1 Introduction

In the realm of photoplethysmography (PPG) research, the precision and adaptability of measurement systems play a pivotal role. Recognizing this, the measurement systems developed for this thesis were intricately designed to offer unprecedented user control over critical sensor parameters. These include the ability to adjust the wavelength, fine-tune the distance between the photodiode and LED, and precisely regulate the applied transmural pressure. Such control is not just a matter of convenience but a necessity for tailoring measurements to diverse experimental conditions, thereby enhancing the accuracy and applicability of PPG data in studying pulsatile phantoms.

This chapter delves into the intricate details of the design, mechanical fabrication, and implementation of these advanced systems. Central to our discussion is the Dynamic PPG System (DPPGS), an innovative solution developed to overcome the limitations of conventional PPG sensors. In its various iterations, the DPPGS embodies the synthesis of precision engineering and practical functionality, offering insights into both the challenges and breakthroughs encountered during its development. By revealing these aspects, the chapter aims to contribute not only to the field of biomedical engineering but also to the broader scientific understanding of PPG technology and its applications in simulating and studying vascular dynamics.

Through this exploration, we seek to underscore the importance of customizable measurement systems in PPG research and their impact on producing stable, repeatable, and clinically relevant PPG signals. The journey from conceptualization to realization of these systems reveals a blend of technical ingenuity and methodical rigor, aligning closely with the overarching objectives of this thesis to advance the field of photoplethysmography through novel pulsatile phantom studies.

5.2 Basic Probes

The foundation of photoplethysmography (PPG) measurement lies in the basic PPG probe, a simple yet essential device comprising an optical emitter (LED) and a detector (Photodiode) mounted on a small PCB. This fundamental setup plays a crucial role in capturing PPG signals, a process where light emitted by the LED is absorbed or reflected by the skin, and the changes in light intensity are detected by the photodiode. This basic mechanism underpins the standard PPG measurement, providing insights into vascular properties.

In typical configurations, the basic probe maintains a separation distance between the LED and photodiode of 2 to 5mm. This distance is critical as it influences the depth of light penetration and, consequently, the quality of the PPG signal obtained. Additionally, the wavelengths used in these probes are selected based on their penetration capabilities and the specific application of the PPG signal, ranging from visible to near-infrared spectra. A standard PPG Probe design is show in Figure 23.

While effective for standard applications, the basic PPG probe exhibits significant limitations when employed in advanced PPG research, especially in the context of studying novel pulsatile phantoms. The fixed separation distance and wavelength of the LED in these probes limit the scope of experimentation. For instance, adjusting the distance and wavelength is crucial for simulating various physiological conditions and exploring different aspects of the PPG signal, an aspect critical in my research. These limitations constrain the depth and

breadth of potential investigations, necessitating a more adaptable and sophisticated measurement system.

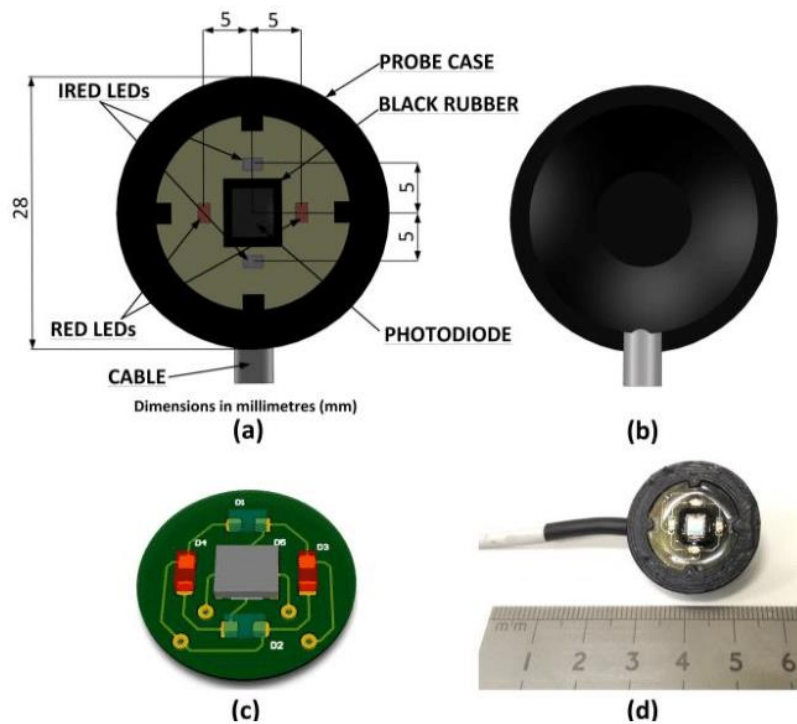


Figure 23 Reflectance PPG Probe. (a) Assembly 3D model of probe front, optical components and dimensions. (b) Assembly 3D model of probe backside. (c) Probe PCB model. (d) Final manufactured PPG reflectance probe. [155]

The inherent limitations of the basic PPG probe underscore the necessity for a more advanced system, leading to the development of the Dynamic PPG System (DPPGS). The DPPGS, conceptualized as a solution to these challenges, offers flexibility in adjusting both the separation distance and the wavelength of the LED. This adaptability is pivotal in expanding the horizons of PPG research, particularly in the detailed and nuanced exploration of pulsatile phantoms. The following sections delve into the development and functionalities of the DPPGS, marking a significant leap from the basic probe to a more tailored and precise PPG measurement approach in biomedical research.

5.3 Dynamic PPG System (DPPGS)

A basic PPG probe, typically comprising an optical emitter (LED) and a detector (Photodiode) fixed onto a small PCB board at a set separation distance of 2-5mm, serves as the cornerstone in standard photoplethysmography measurements [156], [157]. However, our investigation, focusing on the impact of separation distance on PPG signals, necessitated a more flexible approach. The fixed nature of the probe's components limited the scope of exploring varied separation distances. A potential solution involving a PCB with multiple LEDs at different distances was considered but was quickly deemed impractical due to the restricted minimum interval between components and the need for multiple boards for different wavelength emitters. To achieve the desired resolution of data points for separation distance and to incorporate multiple wavelengths, a novel approach was essential. This led to the development of the Dynamic PPG System (DPPGS), an innovative design that successfully addresses these limitations, introducing a new era of flexibility and precision in PPG signal investigation.

5.3.1 DPPGS Version One

The initial iteration of the Dynamic PPG System (DPPGS) Version 1 was developed with a focus on user interactivity and adaptability, a cornerstone in advancing photoplethysmography research. Central to its design was a user-controlled linear stage, a novel feature enabling precise adjustment of the separation distance between the optical emitter and the detector. This customization was pivotal in exploring the nuances of PPG signals under varying spatial configurations.

DPPGS V1 featured a groundbreaking modular design. The emitter (LED) and the detector (Photodiode) were strategically separated onto individual boards, enhancing the system's versatility. This separation was visualized in Figure 24 PPG sensor components cartridges. (A) top-view of photodiode and LED cartridge. (B) Side-view of cartridge. (C) Bottom-view of cartridge inserted into bridge arm., showcasing the 'cartridge' format of these components. Such a modular approach not only facilitated control over the separation distance but also allowed for the swift exchange of emitter cartridges. This was especially beneficial in

experiments requiring different wavelengths, thereby expanding the system's application scope.

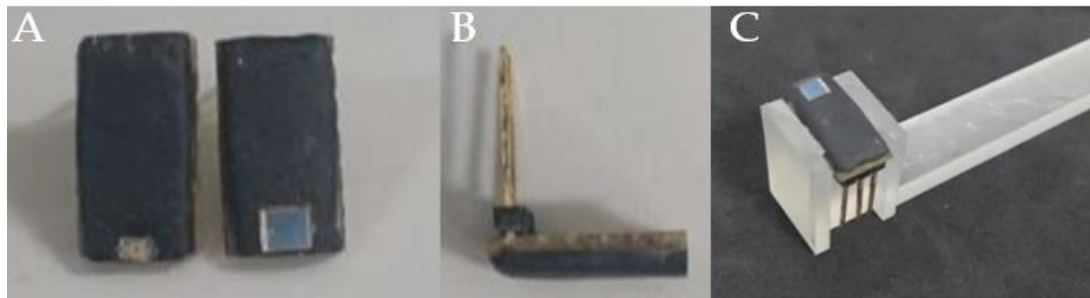


Figure 24 PPG sensor components cartridges. (A) top-view of photodiode and LED cartridge. (B) Side-view of cartridge. (C) Bottom-view of cartridge inserted into bridge arm.

The detector's placement was governed by a motor-controlled linear stage, offering an unprecedented level of precision in distance adjustment. Control over this mechanism was entrusted to a microcontroller, specifically an Arduino, which managed the separation distance with high accuracy. This setup was seamlessly integrated into a custom-built PPG processing system (ZenPPG). Figure 25 provided a comprehensive view of the entire DPPGS V1 assembly.

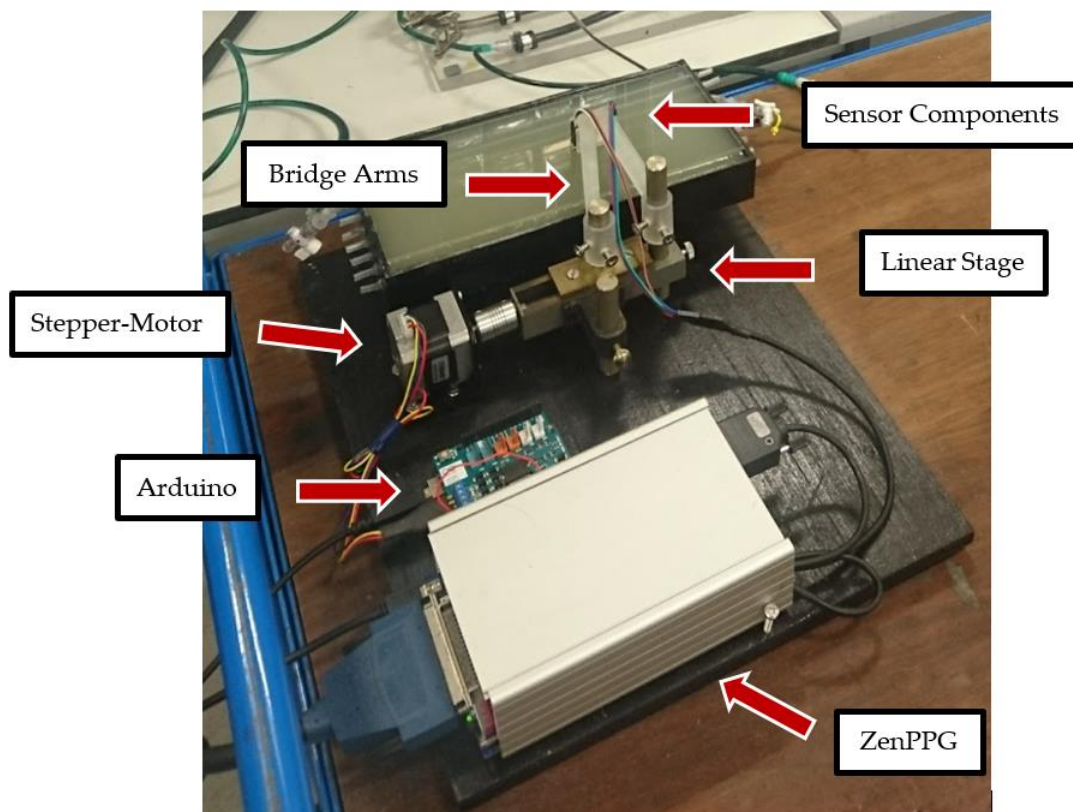


Figure 25 DPPGS V1. The first dynamic system that was developed to control the separation distance of a PPG sensor.

A significant advancement in DPPGS V1 was its semi-automated functionality. By interfacing both the Arduino and ZenPPG with LabView, a sophisticated code was developed. This code enabled automated adjustment of the bridge arm, moving in predetermined steps, and pausing to record signals at each interval. This level of semi-automation was not just a technological achievement but also a practical one, simplifying the experimental protocol and markedly reducing the likelihood of human error in these intricate measurements.

The primary aim in designing DPPGS V1 was to grant unparalleled control over a critical variable - the separation distance between the PPG system's core components. The ability to adjust this parameter with precision opened new avenues in PPG research, allowing for a more nuanced exploration of the PPG signals. The inclusion of semi-automation via LabView further elevated DPPGS V1 from a mere measurement tool to an integral part of sophisticated PPG research methodologies. This advancement signified a leap forward in the pursuit of accurate and repeatable PPG data, aligning with the goals of the research.

5.3.2 DPPGS Version Two

During our initial investigation involving DPPGS V1, we encountered several noteworthy limitations. This system had been derived from a non-specific component and subsequently repurposed for our specific application. Consequently, it exhibited suboptimal resolution and a proclivity for operational failures. As we advanced our research endeavours, it became evident that our investigative requirements not only necessitated precise distance control but also the capability for compression. Thus, we embarked on the development of a novel iteration, DPPGS V2, designed to accommodate multiple functionalities.

In this section, we introduce DPPGS V2 along with its two distinct configurations. The construction of this system employed a linear actuator (TRA-25CC, Newport, UK) due to its exceptional motion resolution, integrated position feedback mechanisms, and ease of integration with LabVIEW software, thereby facilitating seamless automation. An auxiliary

attachment was meticulously engineered to affix to the travel pin of the actuator, enabling the secure attachment of sensors with bidirectional travel capability. This attachment boasts adaptable modules that enable seamless switching between separation distance control and compression functionalities.

The separation distance control mode closely emulates the design principle employed in DPPGS V1, where specialized cartridges are employed to spatially isolate individual system components. During operation, as the linear actuator propels its shaft forward, the LED cartridge affixed to a plate is gradually displaced towards the stationary photodiode. Upon actuator retraction, the application of spring forces ensures the return of the LED cartridge plate into contact with the receding actuator shaft. In this mode, the linear actuator is oriented parallel to the phantom, see **Error! Reference source not found.**

To enable versatile positioning at different orientations and heights, a custom aluminium extrusion frame was meticulously crafted to securely accommodate the actuator.

Transitioning into compression mode involves a pivotal rotation of the actuator, orienting it perpendicularly to the phantom. In this configuration, the cartridge plates are removed, making way for the direct attachment of a PPG sensor module onto a purpose-built plate designed for secure fixation. The actuator's shaft exerts compressive force upon the plate, thereby pressing the PPG sensor firmly against the phantom. For precise force measurement during compression, the phantom is situated atop a platform housing a load cell, facilitating accurate force quantification, see Figure 26. Table 3 provides the detailed specifications for all the systems components.

The integration of the linear actuator and the load cell into the LabVIEW software framework represents a pivotal aspect of our experimental setup. This integration grants us the capability to exert precise control over the linear actuator's movements with exceptional precision. Moreover, it enables the automation of actuator motion, which can be dynamically adjusted

based on real-time feedback data obtained from the load cell. This closed-loop control mechanism ensures that compression forces applied to the phantom are carefully regulated, allowing for precise and repeatable experiments.

Furthermore, the LabVIEW software platform seamlessly facilitates concurrent data acquisition from the PPG sensor. This synergy enables us to not only monitor the live feedback data from the load cell but also to simultaneously collect and record valuable physiological information from the PPG sensor. By synchronizing these diverse data streams within a unified software environment, we achieve a comprehensive understanding of the experimental conditions and their impact on the measured physiological parameters. This integrated approach not only enhances the precision of our experiments but also streamlines data analysis and interpretation, ultimately advancing the quality and depth of our research outcomes.

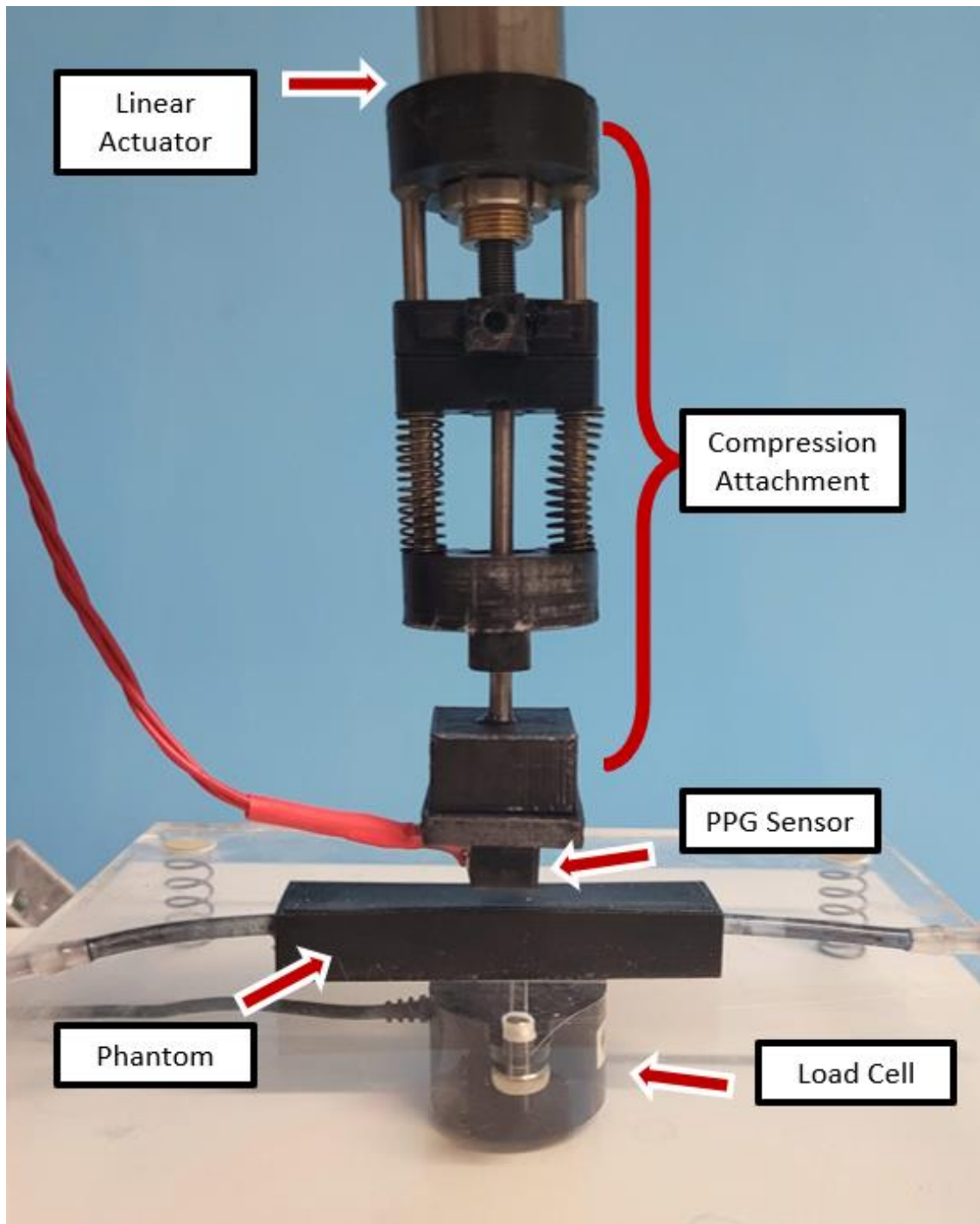


Figure 26 DPPGS V2 in Compression mode.

Table 3 Specifications for all DPPGS V2 system components

PPG Sensor OSRAM SFH 7050	
Peak Emission Wavelengths ($I_F = 20 \text{ mA}$)	660 nm, 950 nm, 525 nm (unused)
Power Source (supply voltage = 5 V)	Dual current source (multiplexed 2 wavelengths) 0 – 80 mA adjustable OR Single current source for one wavelength operation (non-multiplexing) 0 – 80 mA
System Resolution	16 bit ($\pm 5 \text{ V}$ voltage span) = 152.6 μV
Amplifier Gain	105.1 dB
TRA-25CC Linear Actuator	
Push Force	60 N
Travel Range	25 mm
Minimum incremental Motion	0.2 μm
Maximum Speed	0.4 mm/s
Typical Accuracy	$\pm 2.5 \mu\text{m}$
Guaranteed Accuracy	$\pm 5.0 \mu\text{m}$
Encoder Resolution	0.030517578 μm
FC2231-0010 Load Cell	
Operating Force	4.54 Kgf
Output	0.5-4.5 V
Accuracy	$\pm 1 \%$
10 secs No Load	0.5225 V 0.0051 stdev
60 secs Load	1.4554 V 0.0107 stdev

5.4 PPG Processing and Acquisition System

The acquisition system employed in this study, referred to as ZenPPG, is a versatile research photoplethysmographic (PPG) system designed by the Research Group at City University of London [158]. ZenPPG serves as a crucial tool for acquiring raw PPG signals during our in vivo investigations, which will be detailed in subsequent chapters.

This open-source system offers a common architecture that researchers can customize to suit their specific needs. Its key features include the capability to interchange custom-made sensors and precise control over light intensities. While the author of this thesis did not

personally design the system, extensive testing and evaluation were conducted to enhance its performance, particularly focusing on the core board.

ZenPPG is a dual-wavelength, dual-channel PPG system. Its primary functionalities encompass the acquisition of raw PPG signals (both AC and DC components), light intensity adjustment, and compatibility with both custom-made and commercial PPG sensors. The system comprises five distinct boards: the power board, current source board, core board, transimpedance amplifier board, and bus board. The current source board supplies driving currents to the LEDs, while the core board manages intermittent light modulation and the separation of signals by wavelength using multiplexer/demultiplexer components. The transimpedance amplifier board converts photodiode currents into voltage signals, and the power board provides the necessary power supply. The bus board facilitates communication and signal transmission between these components.

To control and monitor light intensities, the ZenPPG system is interfaced with LabVIEW and National Instrument Data Acquisition Cards (DAQ). This configuration ensures precise PPG signal acquisition while affording researchers the flexibility to regulate and record light intensities as needed. The comprehensive structure and functionalities of ZenPPG play a pivotal role in achieving the research objectives of this work, making it an indispensable component of this thesis.

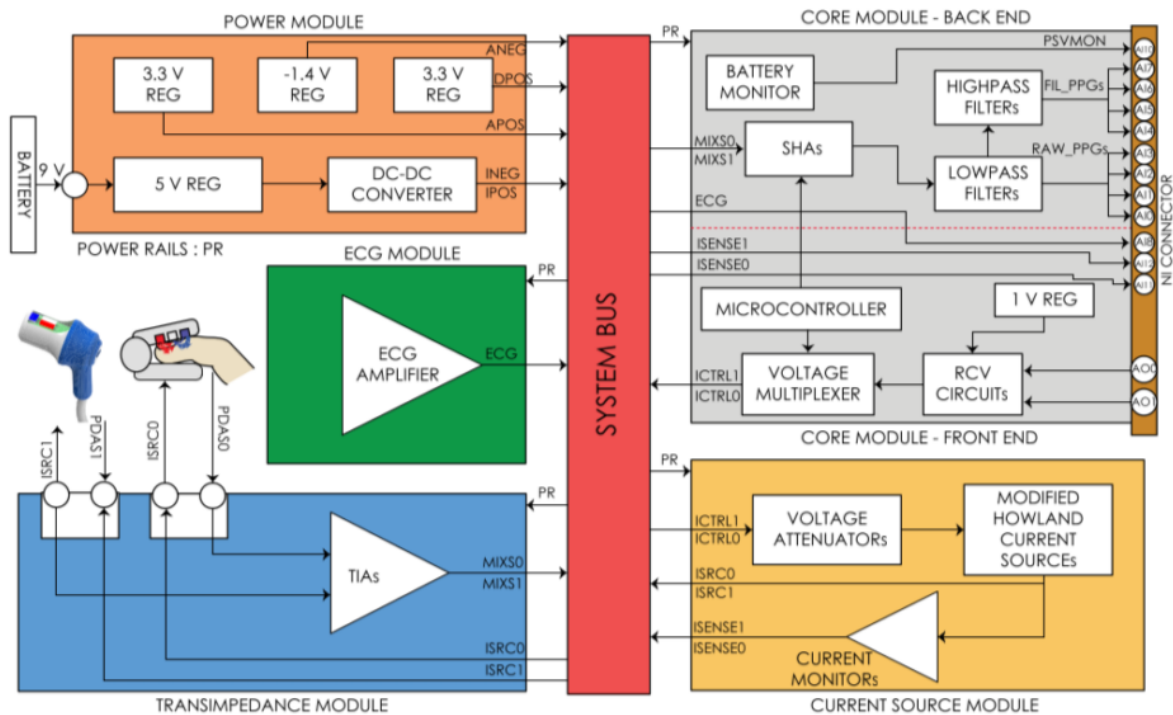


Figure 27 Detailed block diagram showing the architecture of ZenPPG [158].

Summary

This chapter delves into the creation of the Dynamic PPG System (DPPGS) for enhanced photoplethysmography (PPG) research. This chapter outlines the limitations of traditional PPG probes and introduces the DPPGS, a sophisticated system designed for greater flexibility and precision in PPG signal measurement. Key advancements include user control over sensor parameters like wavelength and separation distance, and the integration of advanced features like a linear actuator for improved motion resolution. The DPPGS, evolving through multiple versions, significantly enhances the capability to produce stable, repeatable, and clinically relevant PPG signals, aligning with the thesis's goal to advance PPG research through innovative approaches.

6

Development of Phantoms

6.1	INTRODUCTION	80
6.2	IDEAL SPECIFICATIONS	81
6.3	BRACHIAL GELATINE PHANTOMS	83
6.4	SILICONE PHANTOMS	86
6.5	FABRICATIONS OF CUSTOM VESSEL	91
6.6	VALIDATION OF VESSELS AND TISSUE	94
6.6.1	VESSEL PROPERTIES	94
6.6.2	TISSUE PROPERTIES.....	101
6.6.3	SIGNAL COMPARISON	103
	SUMMARY	104

Introduction

6.1.

The realm of photoplethysmography (PPG) research is rapidly expanding, driven by the need to understand the intricacies of PPG morphology under varying physiological conditions. This ever-expanding field necessitates the use of highly specialized vessel and tissue phantoms, which boast tuneable properties, allowing researchers to simulate and investigate diverse physiological states.

In this chapter, we pivot our focus towards the design, fabrication, and characterization of a pulsatile tissue phantom. This phantom is not just an artificial model; it's a meticulously engineered entity designed to mimic the mechanical and optical properties of the human finger, a prevalent site for PPG measurements. The journey from the selection of materials like gelatine, valued for its high biological fidelity and practicality, to the adoption of silicone for its durability and tunability, underscores the commitment to achieving a balance between realism and functionality in phantom development.

This chapter also delves into the intricacies of custom vessel fabrication, an essential component in the creation of phantoms that accurately replicate the dynamic nature of human

vascular systems. The ability to mimic the pulsatile nature of human arteries and veins is not just a matter of replicating appearance but also function. Our methods in creating these vital components ensure that our phantoms behave like their biological counterparts, both in appearance and functionality.

Finally, we underscore the significance of mechanical validation. Our phantoms are rigorously tested to confirm that they can accurately simulate the conditions necessary for PPG sensor testing, particularly focusing on the simulation of human tissue mechanics under different physiological and pathological states. This validation is a cornerstone in confirming the utility of our in-vitro system for potential investigations of PPG sensor technologies against a pulsatile phantom, where properties of the phantom or the pump can be altered to investigate different pathologies.

In summary, this chapter presents a comprehensive overview of our journey in developing a pulsatile tissue phantom. Our investigations demonstrate the potential of this in-vitro system to be utilized in future explorations of PPG sensor technologies, offering a robust platform for simulating a wide range of physiological conditions and pathologies.

6.2.

Ideal Specifications

It's crucial to define the ideal specifications for such a phantom, particularly in the context of advanced PPG applications. The target characteristics for an advanced PPG phantom should encompass a range of attributes that not only simulate the human physiological environment but also allow for comprehensive testing and analysis of PPG sensor technologies. These specifications include:

- **Optical Properties:** The phantom should closely mimic the optical properties of human skin and underlying tissues. This includes appropriate scattering and absorption coefficients to simulate the interaction of light with human tissue. The phantom should be capable of replicating various skin types and conditions, allowing for diverse PPG signal analysis.

- **Elasticity:** A key characteristic of an advanced phantom is its mechanical flexibility. The material should have an elasticity similar to human skin and vessels, allowing it to deform under sensor pressure in a manner akin to real tissue. This deformation is crucial for accurately simulating the contact area changes between the sensor and skin, which impacts light penetration and PPG signal quality.
- **Pulsatility and Flow Dynamics:** The phantom should have embedded vascular channels or tubes that can simulate the pulsatile nature of human blood flow. These channels should be capable of rhythmic expansion and contraction to mimic the arterial pulse. The flow dynamics within these channels, including the ability to adjust flow rates and pressure, are essential for studying the effects of different physiological and pathological conditions on PPG signals.
- **Durability and Consistency:** Given the need for repetitive testing, the phantom should be durable, capable of withstanding multiple uses without degradation in its properties. Material consistency is also vital to ensure that the phantom can provide reliable and repeatable results across various experiments and testing scenarios.
- **Tuneable Properties:** The ability to tune the phantom's properties, such as its optical and mechanical characteristics, is essential. This tuning capability allows for the simulation of a wide range of physiological conditions, including variations in tissue composition, blood flow rates, and pathological states like arterial stiffness or hypertension.
- **Biocompatibility and Safety:** While primarily used in a laboratory setting, the materials used in the phantom should be non-toxic and safe for handling. Biocompatibility is particularly important if the phantom is to be used in scenarios that mimic clinical settings.
- **Customizability:** The phantom should be designed in a way that allows for customization in terms of size, shape, and internal structure. This adaptability is crucial for creating phantoms that can simulate different body parts and specific conditions required for targeted PPG research.

Brachial Gelatine Phantoms

6.3. B.W. Pogue produced an in-depth review on phantoms and concluded that the most limiting attribute of phantom technology is the discrepancies in the measurement of its optical properties. Measurements by different groups was at best 10-15% in agreement[120] . Multi-modal phantoms incorporate several substances to produce the correct optical and mechanical properties, and with every added substance the error in properties' values increase. Due to the above inaccuracies and inconsistencies of existing phantom technologies and its literature, this work introduces a homogenous phantom with base absorbance and scattering properties. The choice of gelatine as a foundational material in phantom development serves as a crucial first step in this research, providing a reliable and reproducible platform upon which more complex and advanced phantom models can be built. Gelatine's versatility and ease of manipulation make it an ideal candidate for establishing a standard baseline in phantom characteristics. This base model sets a benchmark for absorbance and scattering, essential parameters in PPG studies, ensuring that subsequent developments in phantom technology can be compared and evaluated against a consistent and well-understood standard. A limitation of using reference recipes is the potential differences in optical properties that arise from using ingredients from different suppliers for the recipe. It would be ideal to measure the absorption and scattering coefficients within in the lab to ensure the phantoms were made to specification.

6.3.1. Design and Development

The design of this phantom was made to mimic the upper arm, a common site for blood pressure cuff placement. In this region, the brachial artery is typically surrounded by subcutaneous fat. Our phantom emulates these anatomical characteristics. While various research groups have previously measured the optical properties of human tissues and the corresponding concentrations of additives, their results show slight variations due to differing equipment and methodologies [159], [160]. Our phantom comprises of silicone vessels with a 4 mm outer diameter and 3.5 mm inner diameter (Hilltop Products, UK), possessing elastic

properties representative of a healthy human artery, according to the manufacturer. To mitigate batch inconsistencies, we fabricated a single large phantom embedding multiple vessels. These vessels were strategically placed at uniform intervals, with depths ranging from 3.2 mm to 24.6 mm.

The homogenous dermis mimicking layer was fabricated from a mixture of 18% bovine gelatine, 1% soya milk and 0.06 % India ink solution. The following steps outline the mixing procedure:

- 1) The required amount of distilled water is heated in a beaker on a hot plate to 70 degrees Celsius.
- 2) The heating element is turned off, and the magnetic stirrer is set to 500 rpm.
- 3) The gelatine is measured out and added gradually to the solution, ensuring no lumps are formed.
- 4) Once the temperature has dropped to 50 degrees, milk and ink are added and the stirrer is turned down to 50 rpm. This allows any bubbles formed to rise.
- 5) Let the mixture cool to 40 degrees and skin off the foam layer formed on the surface.
5. Carefully pour the mixture into the phantom container to the desired height, and cover with the lid or glass panel.
- 6) Place the phantom in the fridge for 2 hours to fully set or in the freezer for 30 mins. The faster it sets the more homogenous it is. The heavier particles slowly sink downwards.
- 7) Once set, leave the phantom at room temp for at least 30 mins. Immediate measurements will experience fluctuations due to temperature changes as the phantom reached room temp.
- 8) One at room temp the ends of the vessel can be attached into the pump system.

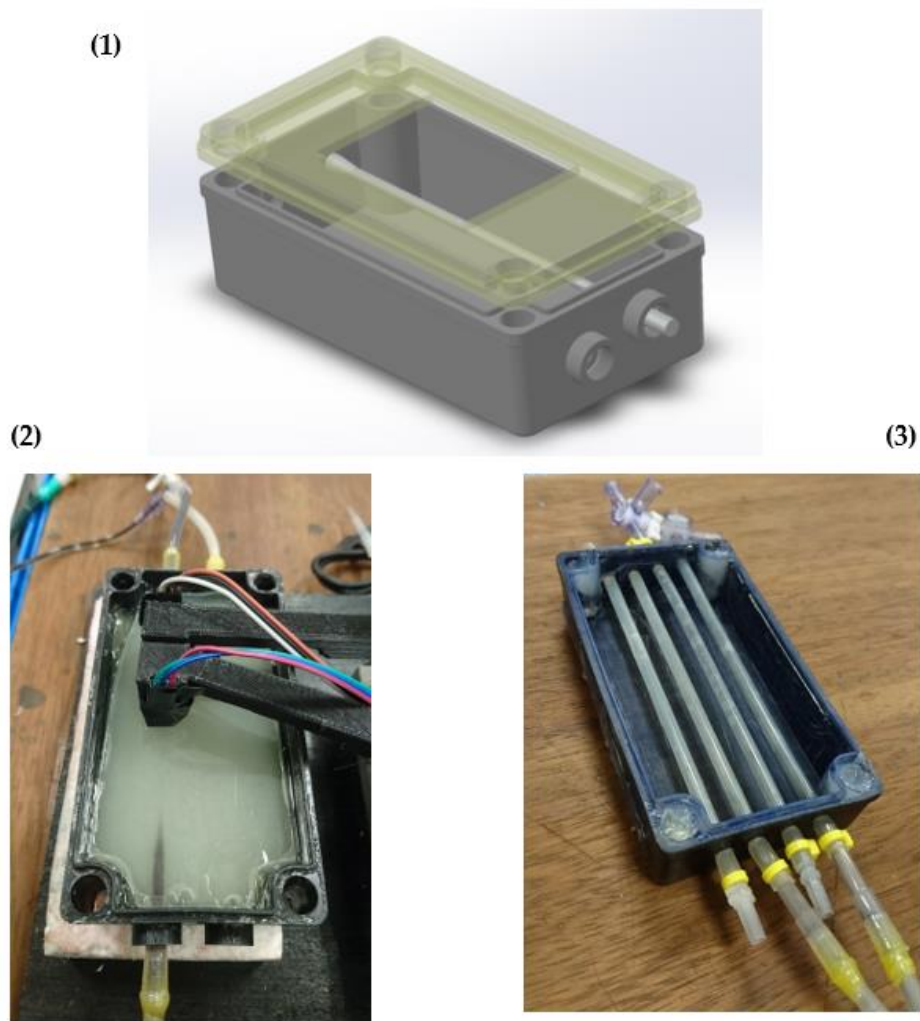


Figure 28 (1) Initial CAD design for a simple dual vessel phantom enclosure. (2) Dual vessel phantom with gelatine tissue and dual silicone vessels connected to the investigation setup. (3) A 3D printed enclosure with a modified design with further vessels added.

An aspect of this development was the use of 3D design software, which enabled precise modelling of the phantom's internal architecture. Through this technology, we could visualize and adjust the spatial arrangement of the vessels within the phantom, ensuring optimal placement and depth, and print the custom enclosure. Figure 29 shows design iterations with a dual vessel and quadruple vessel model. This integration of 3D design and printing not only expedited the prototyping process but also allowed for a high degree of customization, adapting to the specific requirements of our research. After experimentation and evaluation, informed by both the theoretical insights and practical feedback gained from our process, we settled on a single, cohesive design: a phantom featuring nine distinct vessels, each

strategically placed at varying depths. The varying depths of these vessels enable us to closely mimic the nuanced layers of human vasculature, providing a robust platform for testing and analysis of the effect of vessel depth on the PPG signal.

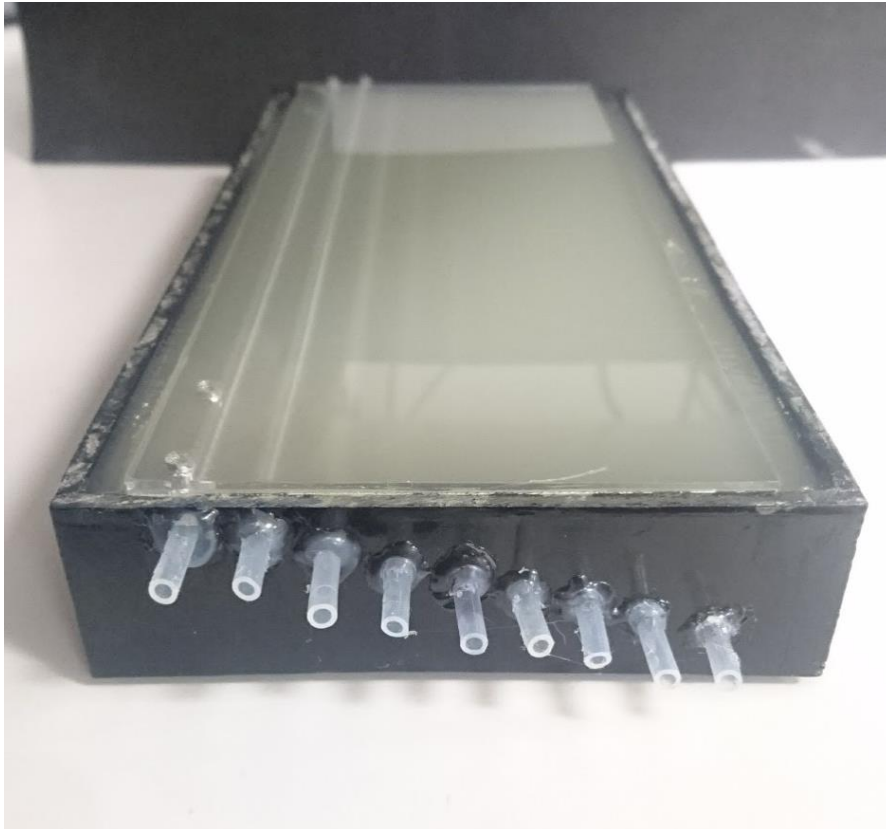


Figure 29 Nine vessel gelatine brachial phantom.

6.4.

Silicone Phantoms

While gelatine phantoms have been instrumental in initial photoplethysmography (PPG) research due to their simplicity and basic tissue mimicry, their limitations necessitate the exploration of more advanced materials. Key drawbacks of gelatine phantoms include their instability over time, limited durability, and inadequate replication of the complex mechanical and optical properties of human tissue. These factors lead to inconsistent PPG readings and restrict their use in sophisticated PPG applications.

Given these constraints, silicone emerges as a superior alternative for phantom development. Unlike gelatine, silicone offers enhanced durability, stability, and a closer approximation to human tissue properties. It provides greater versatility for embedding complex vascular structures and customizing optical characteristics, crucial for accurate PPG sensor testing. The next section explores the design and development of silicone phantoms, highlighting their advantages over gelatine models in advancing the realism and applicability of PPG research.

6.4.1. Design and Development

PPG measurements, frequently taken from the finger, are particularly convenient for personal health monitoring devices. The finger, comprising of digital arteries embedded within fat and tendons, exhibit diverse optical and mechanical properties. For the current phase of the phantom design, we have chosen this site to model the phantom after.

While developing the phantoms, several preliminary iterations were conducted using clear silicone. This approach was strategically chosen to allow for direct visualization of the internal vessel structures. The transparency of the silicone in these early models was instrumental in observing and understanding the positioning and behaviour of the embedded vessels under various simulated conditions, see Figure 30. This visual access provided critical insights into the effectiveness of the vessel integration and the dynamic fluid flow within the phantom. These trials with clear silicone significantly informed subsequent design refinements, ensuring optimal alignment and functionality of the internal structures in the final product.

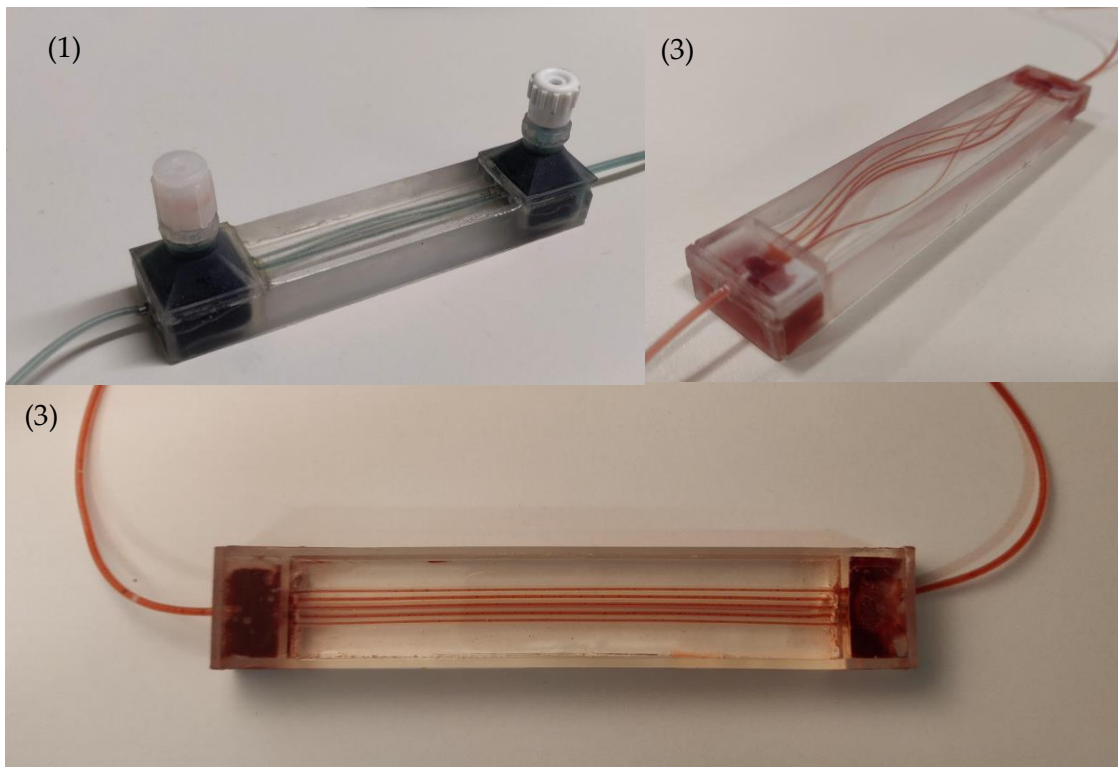


Figure 30 Phantom prototypes. (1) a multivessel finger phantom with bleed ports in the connecting chambers. (2) multivessel phantom exhibiting undesired warping. (3) Version 1 of a working multivessel phantom.

In the progression from preliminary trials to the final phantom design, significant attention was given to formulating the silicone tissue solution, crucial for replicating the physiological properties of human tissue. Here are the refined steps of this process:

1. **Base Preparation:** Starting with medical-grade polydimethylsiloxane (PDMS), we meticulously prepared the base mixture, adhering to precise ratios of pre-polymer and curing agent to achieve the required consistency.
2. **Optical Property Adjustment:** To simulate the light absorption akin to human tissue, an exact amount of India ink, determined by Liu et al.'s [132] formula, was added to the silicone. This step was crucial for matching the absorption coefficients for red and infrared light, mirroring those of subcutaneous fat [5]. At this stage, we have not considered scattering properties to streamline the manufacturing process.

3. **Homogenization:** The mixture, now containing India ink, underwent thorough mixing to ensure uniform distribution, crucial for consistent optical properties throughout the phantom.
4. **De-gassing for Clarity:** A vacuum chamber was used to de-gas the mixture, removing air bubbles that could affect the optical clarity and uniformity of the silicone tissue.
5. **Curing and Inspection:** After pouring into molds or direct application to the phantom, the mixture was cured under controlled conditions. Post-curing, the silicone tissue was examined for any inconsistencies in texture or clarity.
6. **Final Adjustments:** Based on these observations, adjustments to the composition were made in subsequent batches, refining the tissue properties to more closely resemble human tissue.

This formulation process was pivotal in bridging the gap from the clear silicone prototypes to the final, more anatomically accurate phantom, ensuring that both mechanical and optical characteristics of human tissue were closely replicated in the final product.

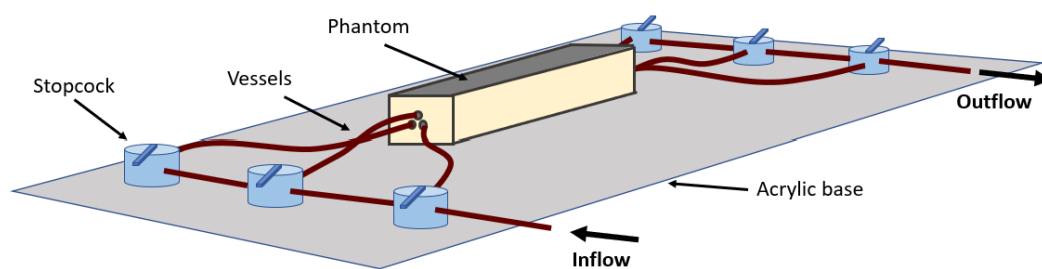


Figure 31 Illustration of the assembled phantom connected to the distribution network fixed on an acrylic sheet.

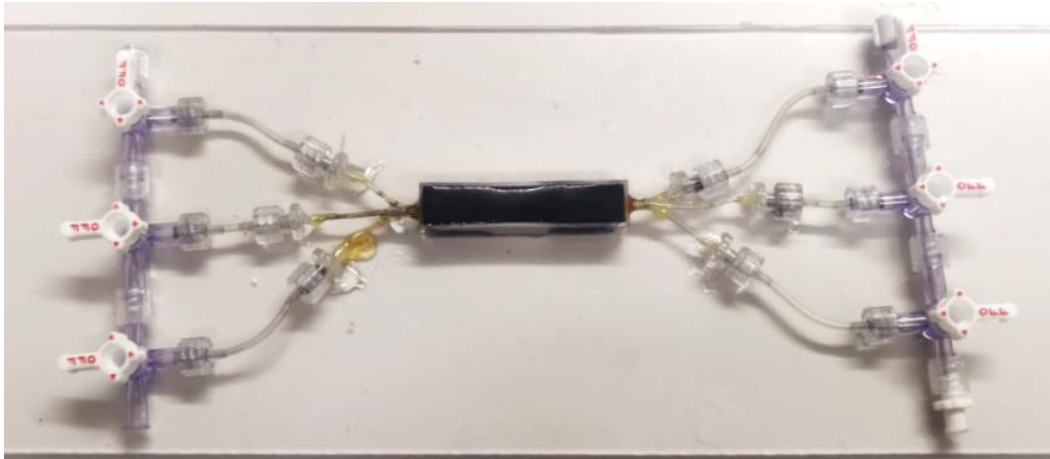


Figure 32 Photo of the assembled phantom fixed on an acrylic sheet.

The phantom depicted in Figure 32 represents the culmination of numerous design iterations. Initially facing challenges with the shared chamber design, particularly blocked vessels, we introduced individual stopcocks for each vessel. This modification allowed for targeted flow control to specific vessels, effectively resolving the flow issues and ensuring consistent fluid movement through each vessel.

Initially, in the development of the phantom, we employed commercial vessels due to their ready availability and ease of integration. These vessels were adequate for replicating larger vascular structures like the brachial artery, producing high-quality PPG signals that closely resembled physiological readings. However, when simulating smaller vessels, particularly those akin to digital arteries, the commercial vessels presented significant limitations. Their inherent stiffness, not representative of the more pliable nature of smaller arteries, resulted in poorer quality PPG signals, failing to accurately mimic the subtle hemodynamic variations found in finer vasculature.

This discrepancy in signal quality and physiological realism highlighted the need for more flexible and anatomically accurate vessels. Consequently, we shifted our focus to developing custom in-house vessels. These custom vessels were designed to offer greater elasticity and more accurately represent the dimensions and mechanical properties of human arteries. The subsequent section details the process and rationale behind the development of these custom vessels, showcasing their role in enhancing the fidelity of our PPG phantom models.

Fabrications of Custom Vessel

In this section, we delve into the development of a novel approach for fabricating custom polydimethylsiloxane (PDMS) vessels, a pivotal component in our pulsatile vascular tissue 6.5. phantoms. Our method, centered around a continuous dip-coating process, marks a significant leap in phantom design. It facilitates the creation of vessels with precise dimensions and mechanical properties, tailored to the unique requirements of PPG sensor testing.

The motivation for this custom fabrication approach is rooted in our model's anatomical accuracy, specifically mirroring the finger, a common site for pulse oximetry. The human finger, primarily supplied by the radial and ulnar digital arteries, has been reported to have an average largest digital artery diameter of 1.44 mm [161], with the nearest comparable vessel, the superficial palmar arch artery, having an intima-media thickness (IMT) of 105 μm [162]. These specific dimensions pose a challenge as commercial artificial vessels or tubing rarely meet these exact values, and custom production is often prohibitively expensive. This gap in the availability of suitable artificial vessels has been a common obstacle in PPG research, compelling many groups to pursue their own vessel fabrication methods [163]. Consequently, a unique fabrication method was developed to create vessels that not only meet these specific anatomical dimensions but also contribute to advancing the field of PPG research.

6.5.1. Methodology

This process, leveraging the capabilities of a modified dip coating system, was meticulously designed to create vessels that not only meet the exacting standards required for accurate PPG sensor testing but also offer versatility in terms of size and mechanical characteristics. Here is the detailed methodology that follows this approach:

- 1) **Preparation of the Dip Coating System:** A precision dip coater (Qualtech, UK) is adapted for the fabrication process. Silicone tubing with an internal diameter (ID)

of 1.3mm (Hilltop-Products, UK) is attached to the dip coater's arm and threaded through a heating coil.

- 2) **Dip Coating Process:** The silicone tubing is then passed through a trough filled with PDMS (Sylgard 184, Dowsil, UK), selected for its long pot life of 2 hours and fast cure rate. This setup is diagrammatically represented in Figure 33.
- 3) **Coating and Curing:** The tubing, weighted and suspended across a series of pulleys, is dipped into the PDMS. The dip coater system progresses the tubing at a steady rate of 10 mm/min to ensure an even coating. The coated tubing then passes through the heating element set at 275°C, curing the coating.
- 4) **Withdrawal and Final Curing:** Once the dip coater reaches its maximum withdrawal length, the tubing is cut, and the system is reset. The coated tubing is then placed in an infrared reflow oven set at 150°C for 10 minutes to ensure complete curing.
- 5) **Separation and Customization:** After curing, the PDMS coating is separated from the internal silicone tubing. This method results in custom vessels with inner diameters equivalent to the outer diameter of the silicone tubing. The wall thickness and mechanical properties, including shore hardness, are adjustable by varying the withdrawal speed and altering the catalyst ratio of the PDMS.

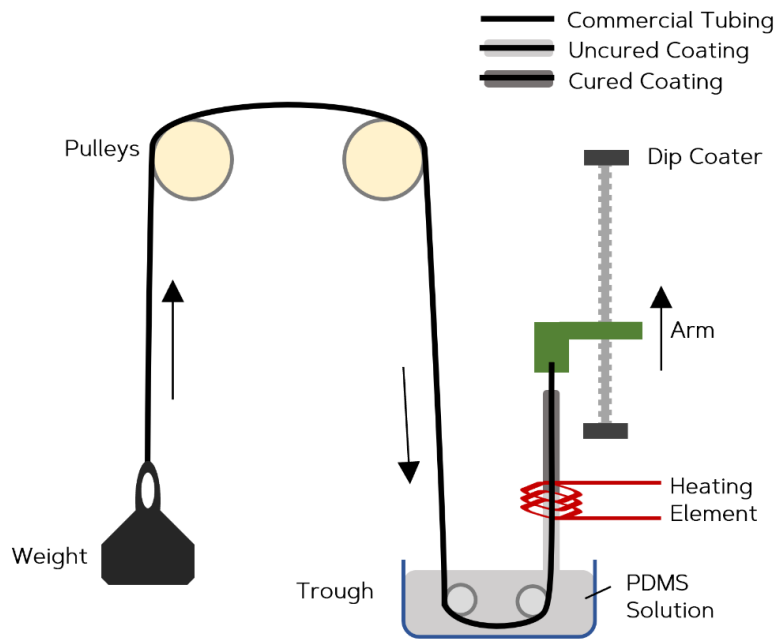


Figure 33 Continuous dip-coating vessel fabrication method.

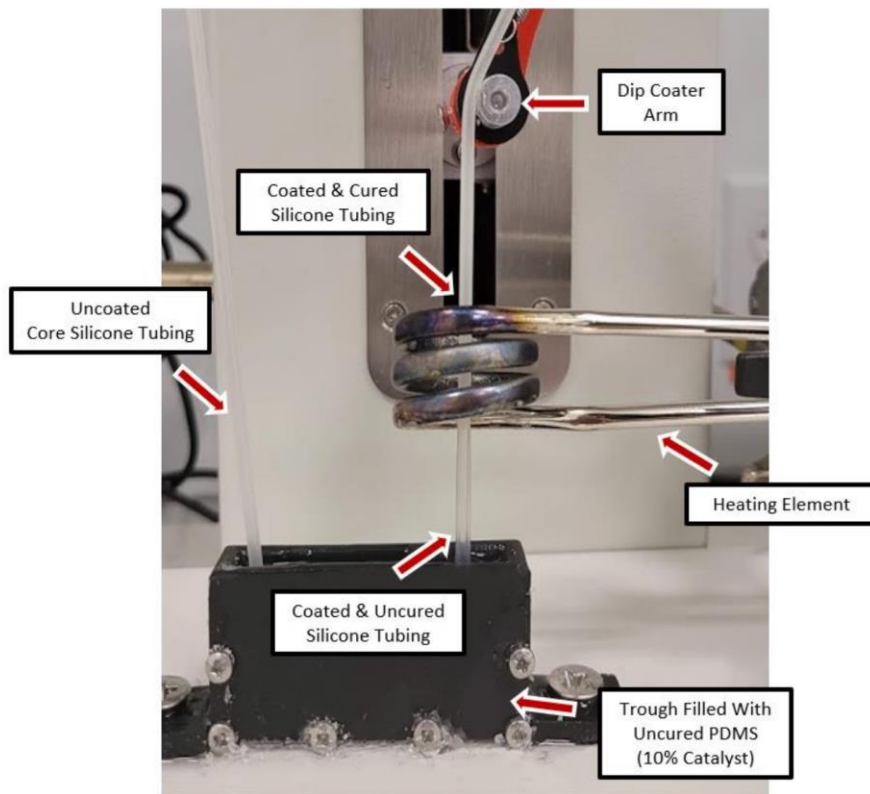


Figure 34 an Image showing the trough, heating element and dip coater.

Validation of Vessels and Tissue

This section describes the methods used to characterize and evaluate both the custom fabricated PDMS vessels, and the PDMS tissue segments of the phantom. The elastic properties of the vessel under inflation are investigated alongside the compressive strength of segments of PDMS that mimic the tissue portion of a phantom.

The evaluation of the custom fabricated vessels aims to verify their anatomical accuracy, mechanical robustness, and suitability for photoplethysmography (PPG) applications. This assessment is crucial to ensure that the vessels accurately mimic the human vascular system in terms of structure, optical properties, and response to physiological conditions. We compare the resulting ppg signals from commercial tubing and the custom fabricated vessels described in this chapter.

6.6.1. Vessel Properties

Dimensions:

The evaluation of the custom and commercial vessel cross-sections revealed significant differences in their dimensions, a critical aspect for their application in photoplethysmography (PPG). The commercial vessels, typically used in standard phantoms, had a uniform wall thickness of approximately 350 μm . In contrast, the custom-fabricated vessels, designed through a novel dip-coating process, exhibited a more varied and realistic wall thickness, see Figure 35. The median wall thickness for these vessels was measured at about 60 μm , closely resembling the dimensions of actual human blood vessels. This reduction in wall thickness not only makes the custom vessels more anatomically accurate but also potentially enhances their performance in PPG simulations by more accurately mimicking the human vascular system's light absorption and scattering properties. This result highlights the significant advancement made in developing more realistic phantoms for PPG research, where dimensional accuracy plays a vital role in the effectiveness of the simulation. The process was repeated for a vessel size to replicate the radial artery and similarly we see the drastic difference in wall thickness, see Figure 36 .

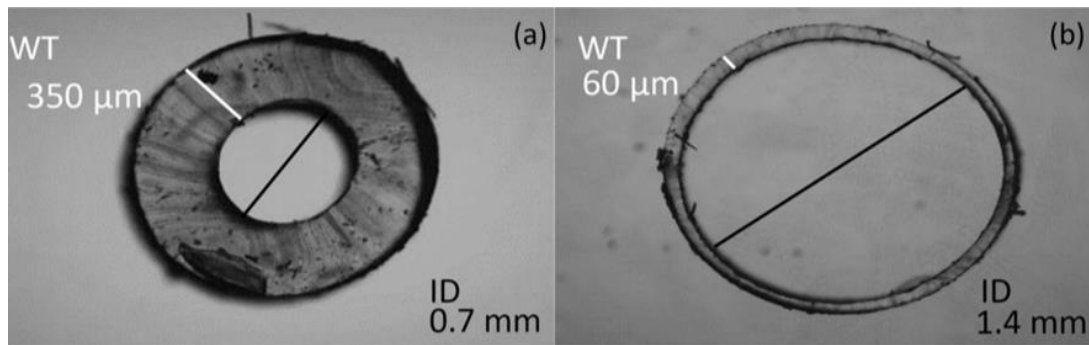
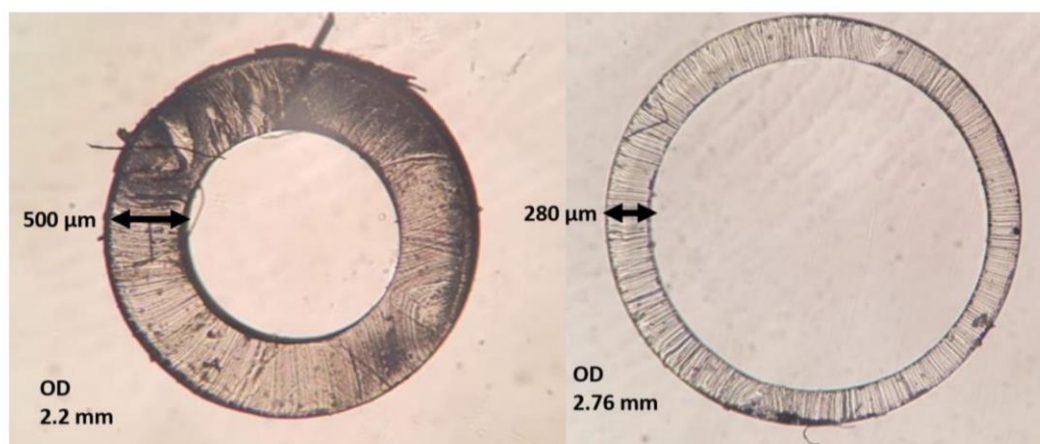


Figure 35 Images of vessel cross sections. Commercial vessel (ID = 0.7 mm) (a) Custom Vessel (ID = 1.4 mm) (b) withdrawn at $10 \text{ mm}\cdot\text{min}^{-1}$. (ID = inner diameter).



d

Figure 36 Cross section of vessels representing the radial artery. Commercial silicone tube (left) with outer diameter of 2.2 mm and an IMT of $500 \mu\text{m}$. Custom silicone vessel (right) with outer diameter of 2.76 mm and an IMT of $280 \mu\text{m}$.

The main variable during production was the withdrawal rate. Four speeds were selected and tested, 5, 10, 15, and $20 \text{ mm}\cdot\text{min}^{-1}$. The vessels were sliced at varying points along their lengths and placed under a microscope (Micropix Ltd, Midhurst, UK) to take measurements using YenCAM (Micropix Ltd, Midhurst, UK). Analysis was performed using MATLAB (The MathWorks, Plano, TX, USA) to determine the effect of withdrawal speed has on wall thickness and variability. The boxplot in Figure 37 displays the distribution of wall thickness at the withdrawal speeds of 5 to $20 \text{ mm}\cdot\text{min}^{-1}$. The median wall thickness shows a positive correlation with withdrawal speed and demonstrates the effect that withdrawal speed has on the variability of wall thickness measurements.

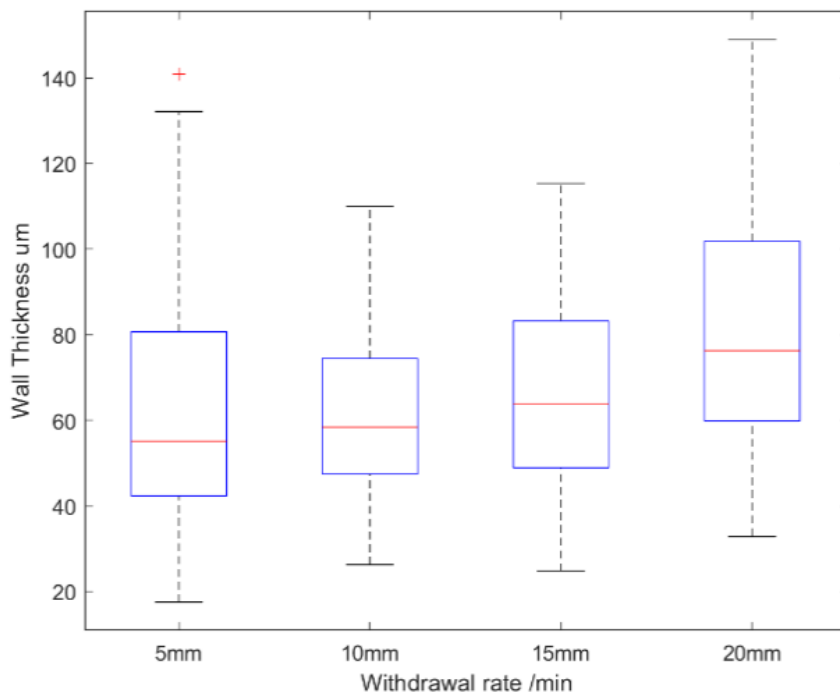


Figure 37 Box plot of wall thicknesses measured from custom vessels withdrawn at several rates.

Mechanical properties:

The fabrication method of the PDMS vessels can be customized to produce vessels at various elasticities by altering the catalyst ratio of the PDMS mixture. The manufacturer guidelines for the selected material (Sylgard 184, Dow Inc, US) are to mix the base with 10% of its weight with the catalyst. Through experimentation, the lowest stable catalyst ratio for vessel production was found to be 3.5%, beyond which the cured solution was too fragile to complete the fabrication process, and instead formed as a gel.

Longitudinal elasticity

A comparative test was first carried out to test the tensile response of the custom vessel against a commercial vessel. Sample 1 was a commercial silicone vessel with an outer diameter of 2.4 mm and a wall thickness of 0.5mm. Sample 2 was the custom PDMS vessel fabricated in the lab at 10% catalyst. The vessel had an outer diameter of 2.76 mm and a wall thickness of 0.28mm. The vessel samples were placed into the grips of the testing system (Instron 5944, Illinois, USA) with a 2kN loadcell, see Figure 38. A Generic tubular tensile test program was selected on the machine and each vessel was pulled apart till the breaking point.



Figure 38 The Instron 5944 installed in the lab (left). Custom radial silicone vessel undergoing tensile stress test (right).

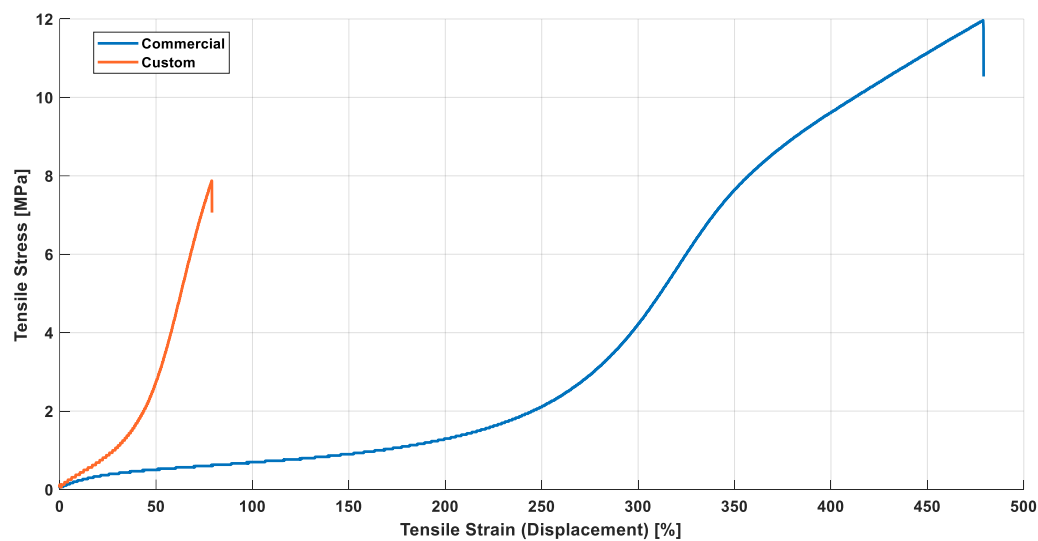


Figure 39 Tensile stress/strain graph of commercial and custom vessel.

The longitudinal tensile stress test was carried out on the 10% custom vessel and the comparative commercial vessel. Figure 39 shows the stress/strain graphs for both vessels. The elastic modulus was calculated to be 0.47 MPa for the commercial vessel and 1.86 MPa for the custom vessel. This longitudinal tensile stress test highlights that when stretched, the commercial vessel is less stiff, failing at almost 500% elongation. Looking at this parameter alone, does not describe the its properties entirely. The custom vessel, although having a higher modulus, failed at a lower stress value, showing that the material for the custom vessel

is softer overall. In a study conducted in 1994, researchers compared the tensile stress of the radial artery wall in normotensive and hypertensive patients [164]. In the study the arterial wall stress was calculated by measuring the change in IMT and vessel diameter using a pulse-echo ultrasonic tracking device and synchronised with the BP waveform from a Finapres system. The results presented from the 47 patients in the study appear to be in the same broad range (1-6 MPa) as the preliminary results we present here, giving us confidence in the path chosen for custom vessel construction.

Most references to the elastic properties of arteries in literature are in-vivo investigation conducted to calculate the circumferential elastic properties. This is often derived with the use of imaging devices to detect the changing dimensions of a vessel, alongside internal pressure information obtained via blood pressure devices. The benefit of our in-vitro system is the ability to measure such properties directly.

Circumferential elasticity

Following the vessel fabrication method outlined, custom PDMS vessels were produced at 10%, 5%, and 3.5% catalyst ratios. The vessels had a wall thickness of 0.2 mm \pm 0.04 mm and an outer diameter of 3.07 mm \pm 0.12 mm which is similar to human radial arteries [165]. The vessels were then cut to lengths between 5 mm and 10 mm and connected to a syringe pump in a closed system show in Figure 40. The pump was used to increase the fluid levels in the vessels and cause inflation. The internal pressure (mmHg) was measured by a pressure transducer, and the resulting change in length and diameter was recorded by a digital microscope. A precision ruler was used as a calibration tool during analysis of the captured images to measure dimensions.

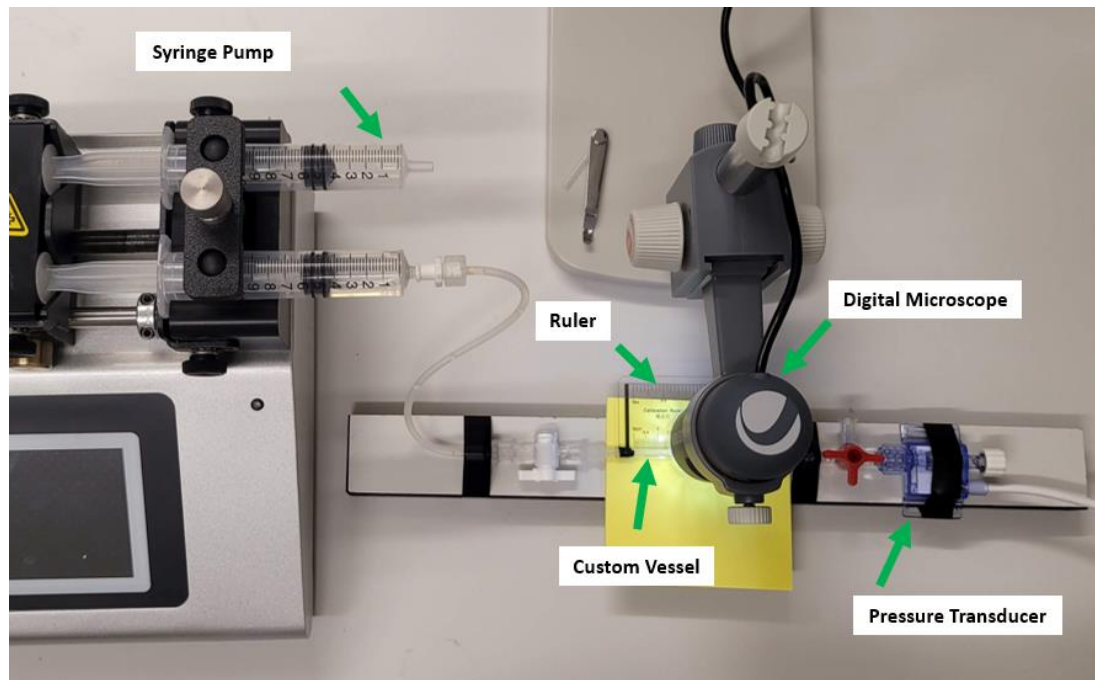


Figure 40 Photograph of the vessel inflation set-up. The syringe pump provided the manual control of internal pressure, with user relayed feedback from the pressure transducer. The digital microscope recorded the parameter changes during inflation by the pump.

For each iteration of the test an initial image was captured with the calibration ruler in focus. The pixel distance between the marks were obtained and then used in the conversion factor for pixels to millimetres. The syringe pump was used to increase the internal pressure from 0 mmHg to the point of failure in 20 mmHg increments. At each step, an image of the vessel was captured with the focus adjusted to sharpen the sides of the vessel. The length was measured from a reference point on the right side of the vessel across the length of the vessel to the black tape. The mean diameter was measured from three points perpendicular to the length line. Figure 41A and 42B show the length and diameter measurements for the 10% catalyst ratio vessel at 0 mmHg and 1000 mmHg respectively.



Figure 41 (A). 10% catalyst vessel at 0 mmHg with annotated pixel measurements of diameter and length. (B) the same 10% vessel at 1000 mmHg internal pressure with annotated pixel measurements of diameter and length. Values are pixel length.

Langewouters et al. carried out ex-vivo pressure-diameter investigations, and our circumferential vessel inflation test was adapted from it [166]. The elastic response of the 10% catalyst ratio PDMS vessel was found to be too stiff, as can be seen in Figure 42 **Error! Reference source not found.** (blue line). Reducing the catalyst ratio does increase the elasticity of the vessel significantly and emphasizes the hyperelastic nature that is expected from them, however, even at 3.5% the response is still not in the target region required and referenced in [166].

The elastic modulus decreases as the catalyst ratio decrease. This is expected as the material resembles a soft rubber at 11% and a soft gel at 2%. The elastic modulus of the 10%, 5% and 3.5% vessels are 1.62 MPa, 0.34 MPa and 0.104 MPa.

The current work in vessel manufacturing is highly encouraging, although it is clear from experimentation and the results shown that the limit of what can be achieved with the current vessel construction has been reached. Significant efforts need to be made to replicate the elastic properties of human vessels closer. The results notably highlight how far commercial vessels are from human biology, and how the custom vessels are a step closer to accurate artificial vessels.

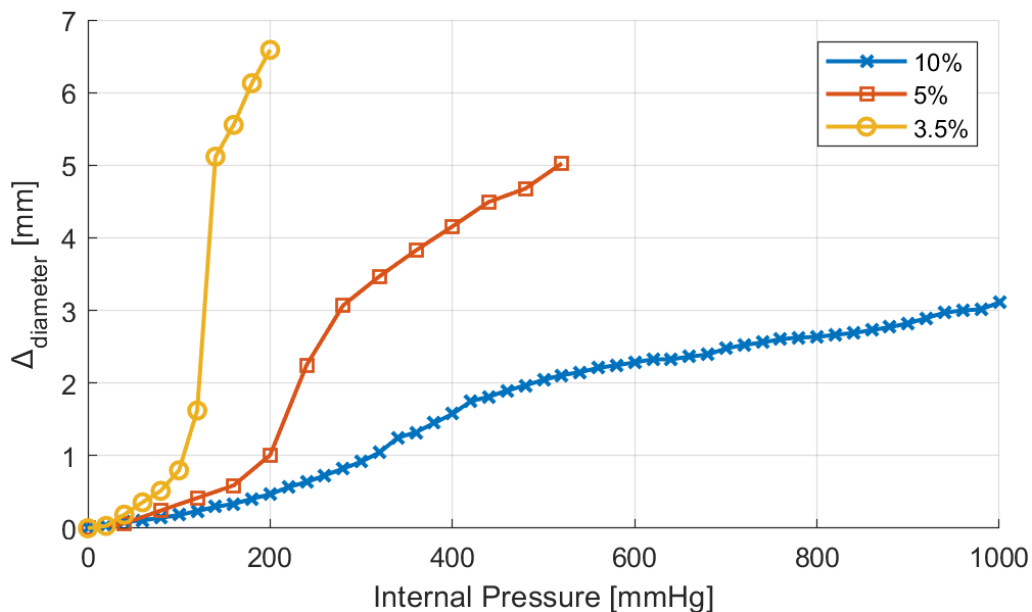


Figure 42 Internal pressure of artery against the measured external diameter change for three catalyst ratios.

6.6.2. Tissue Properties

A basic pulsatile phantom consists of a vessel across which pulsatile flow travels through. This vessel is often embedded into a material which mimics the tissue that would surround the chosen vessel in biology. The manufacturers guideline of 10% catalyst ratio will produce a silicone sample with a shore hardness of 43A which converts to a 2.71 MPa Young's Modulus (YM), which is significantly harder than human tissue. Through experimentation it was found that by reducing this ratio down to a minimum 2%, the elastic properties of the silicone rubber can be manipulated, beyond this point the cured solution resembles a silicone gel.

To aid in the design process of custom phantom fabrication, a dataset for the compressive strength of the PDMS at various catalyst ratio solutions needed to be produced. Eight solutions ranging from 2% to 11% catalyst ratios were poured into 0.5-inch cylindrical moulds to cure at room temperature. After a 48hr cure time, the silicone was removed from their moulds and cut into 1-inch specimens. These specimens then underwent compression testing (Figure 43) in an Instron 5944 in accordance with the ASTM D0575-91 standard.

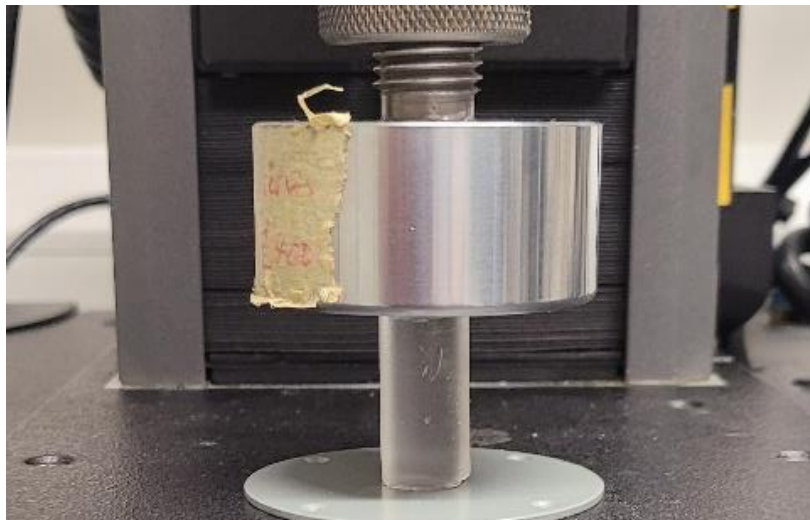


Figure 43 Silicone sample under compression testing.

Shore hardness assessments, conducted using a scale 00 durometer on the fingertips of twenty volunteers, revealed that the average hardness closely matches that of PDMS mixed with a 3% catalyst ratio. This finding, detailed in Table 4, demonstrates that a 3% catalyst ratio effectively emulates the shore hardness of natural tissue at the finger.

Table 4 Results comparing shore hardness at each fingertip and the value for the polydimethylsiloxane (PDMS) when mixed with 3% catalyst. A catalyst ratio below 3% was found to be unstable. Measurements taken with a shore 00 durometer.

	Location	Mean	SD
Left	Thumb	24.4	3.3
	Index	28.7	4.1
	Middle	25.9	3.8
	Ring	23.9	3.5
	Little	29.3	3.4
Right	Thumb	25.4	3.7
	Index	29.4	3.7
	Middle	25.9	4.9
	Ring	23.4	3.0
	Little	31.8	4.2
Phantom	-	32.5	2.4

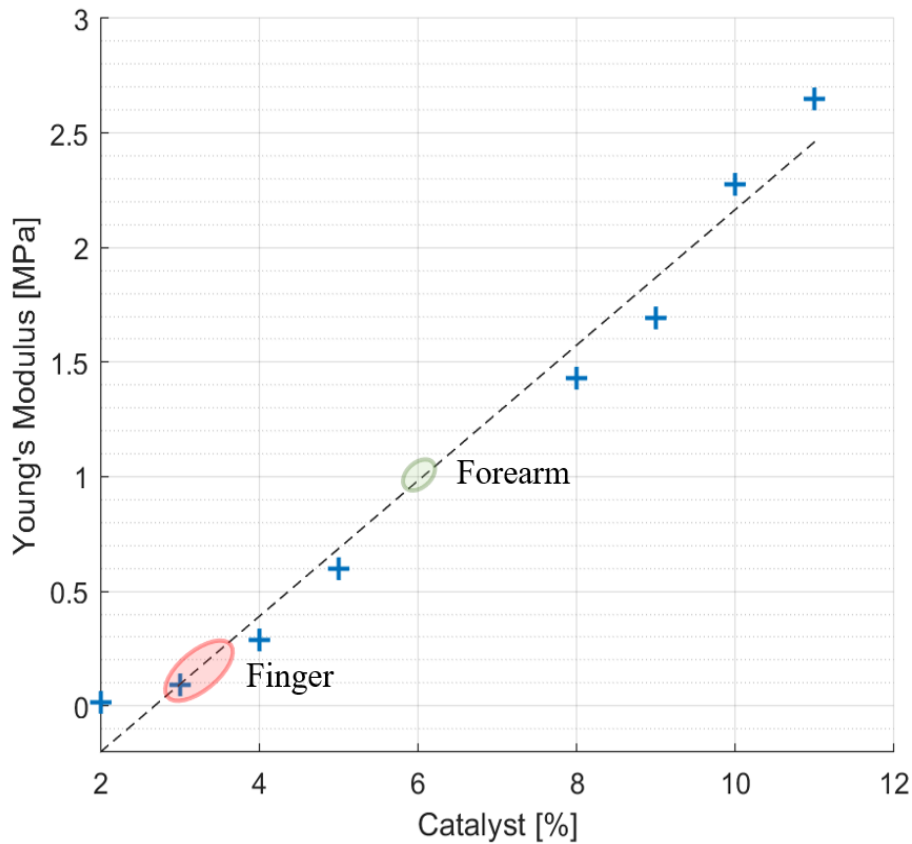


Figure 44 Measured Young's Modulus at different catalyst ratios with the marked YM range for the finger and forearm as seen in the literature[167], [168]

It is observed that as the catalyst ratio decreases so does the elastic modulus, as expected. The graph in Figure 44 shows the measured elastic modulus at the various catalyst ratios. The dataset produced is highly valuable moving forward with phantom design and development, where depending on the desired tissue that needs replicating, the corresponding catalyst ratio can be chosen. The nearest values for tissue from the finger and arm can be found ranging between 0.07 and 0.2 MPa for the finger and 1.03 MPa for the forearm and are highlighted on the graph[167], [168]. The values for the finger are validated values obtained from the volunteer data.

6.6.3. Signal comparison

Both commercial (ID = 1.3 mm) and custom vessels (ID = 1.35 mm) were embedded into separate phantom moulds and encased within clear silicone tissue. Clear tissue was chosen at this stage to eliminate further variables affecting the resultant signals. The phantoms were

connected to the in-vitro system and a pulsatile flow was introduced into the phantoms. PPG data was collected from the sensor (OSRAM SFH 7050) placed above the surface of the phantom. The PPGs of both phantoms were recorded in Labview (National Instruments, Austin, TX, USA) and are compared in Figure 45.

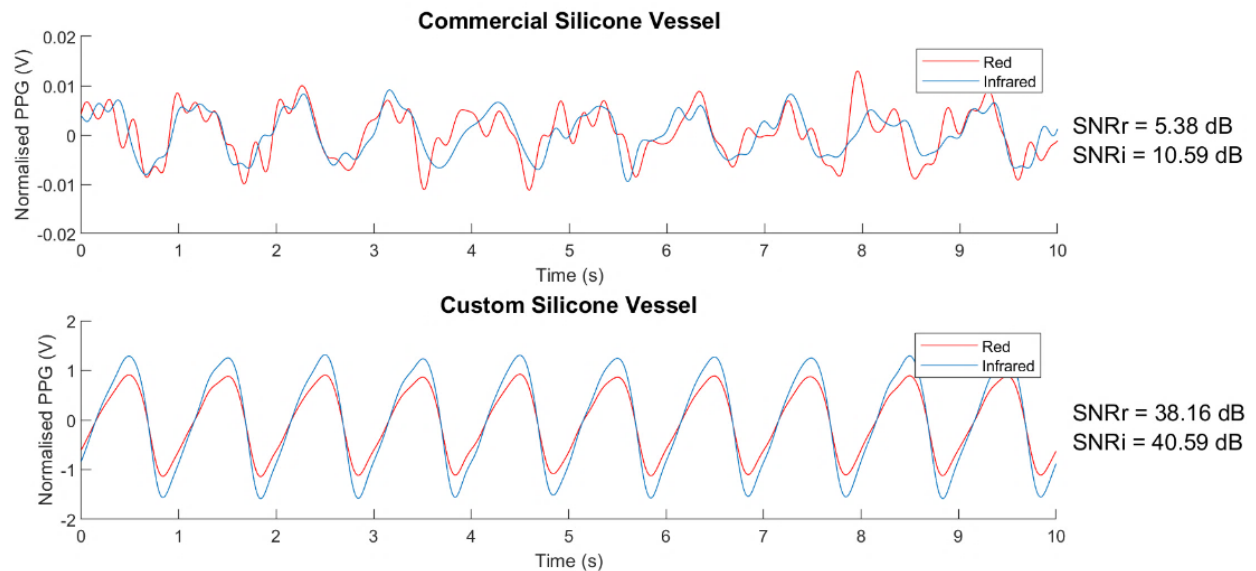


Figure 45 The photoplethysmography (PPG) signal from the clear vessel phantoms. (a) Commercial vessels. (b) Custom vessels. SNRr = signal-to-noise ratio (red wavelength). SNRi = signal-to-noise ratio (infrared wavelength).

Summary

This chapter details the development of tissue phantoms for photoplethysmography (PPG) research. Initially, gelatine was used for its simplicity but later replaced by silicone due to its durability and closer resemblance to human tissue properties. A significant part of the development involved creating custom polydimethylsiloxane (PDMS) vessels using a novel dip-coating system, allowing precise control over their dimensions and mechanical properties.

The phantoms underwent rigorous mechanical testing to validate their ability to simulate human tissue mechanics accurately. This step was crucial in ensuring the phantoms' utility for PPG sensor testing and broader physiological research applications. A key finding was the superiority of custom vessels over commercial ones in providing accurate PPG signals, highlighting their importance in enhancing the fidelity of PPG simulations. In conclusion, this chapter underscores the advancements in phantom development, emphasizing the role of

material selection, anatomical accuracy, and mechanical validation in pushing forward PPG research.

7

Investigating Separation Distance & Arterial Depth

7.1	INTRODUCTION	106
7.2	METHODS	107
7.2.1	PROTOCOL.....	108
7.3	RESULTS	111
	SUMMARY	113

7.1 Introduction

The brachial gelatine phantom, introduced in previous chapters, serves as a pivotal tool in this investigation, aimed at uncovering novel insights into light-tissue interactions central to photoplethysmography (PPG). This research endeavours to peel back layers of complexity and contribute new knowledge to the foundational understanding of the PPG signal's origin. To achieve this, we harness the exploratory potential of in vitro experiments, which allow for meticulous control over each influential parameter.

The novelty of this investigation lies in its collective approach to simultaneously examine the impact of two critical parameters: arterial depth and emitter-detector distance. While previous studies have explored these factors individually [122], [169], [170][171], [172], this research takes a synergistic approach, investigating how variations in both depth and distance jointly affect PPG signal characteristics. Understanding these relationships is crucial for developing more accurate and reliable PPG technologies, particularly in applications where anatomical variances and sensor positioning play a significant role.

Our methodology involves the strategic manipulation of these parameters within the controlled environment provided by the brachial gelatine phantom. This setup allows for the precise measurement and analysis of PPG signals under various simulated physiological conditions. By systematically altering both the depth of the arterial vessels within the phantom and the distance between the PPG signal emitter and detector, we aim to map out

how these variations influence the quality and accuracy of the PPG signal. The outcomes of this study are expected to provide valuable contributions to the field of PPG, enhancing our ability to interpret and utilize these signals in clinical and health monitoring applications.

In doing so, this chapter not only furthers our understanding of the fundamental mechanics of PPG but also sets a precedent for future research in the field, emphasizing the importance of comprehensive, multi-faceted investigations in advancing biomedical engineering technologies.

7.2 Methods

This study was conducted using the brachial gelatine phantom introduced in Chapter 6. This phantom is equipped with nine artificial vessels at depths ranging from 3.2 mm to 24.6 mm, as depicted in Figure 46. The investigation focuses on two key variables: arterial depth and the separation distance between the emitter and detector. The dynamic PPG probe system, detailed in Chapter 5, allows precise control of these variables.

Figure 46 illustrates the homogenous pulsatile phantom featuring multiple vessels with depths incrementally increasing from 3.2 mm (V1) to 24.4 mm (V9). Refer to Table 5 for the specific depths of all vessels.

The dynamic PPG probe system described in chapter 5 (DPPGS V1) was utilised in this investigation. A microcontroller-controlled stepper motor adjusts the separation distance between the two arms. This setup is integrated with ZenPPG, a dual-wavelength, dual-channel research PPG system created by the Research Centre for Biomedical Engineering at City, University of London. ZenPPG is operated via LabVIEW software (National Instruments, TX, USA), which controls the current source and allows for real-time visualization and recording of the signals.

An electronically-controlled pump (Harvard Apparatus, MA, USA) generates the pulsatile flow within the phantom, enabling adjustments in heart rate, stroke percentages for systole

and diastole, and stroke volume. An external pressure transducer (Harvard Apparatus, MA, USA) is incorporated into the artificial arterial network for pressure measurement. With the pump set to simulate average blood flow conditions (5 L/min, 60 BPM), the generated pressure wave closely resembles human blood pressure readings (131/78 mmHg). The pressure waveform's morphology can be further fine-tuned using adjustable resistance clamps placed along the arterial network, which is connected to a gradually narrowing circuit of tubes.

This setup and methodology provide a detailed framework for investigating the impact of arterial depth and emitter-detector separation on PPG signals.

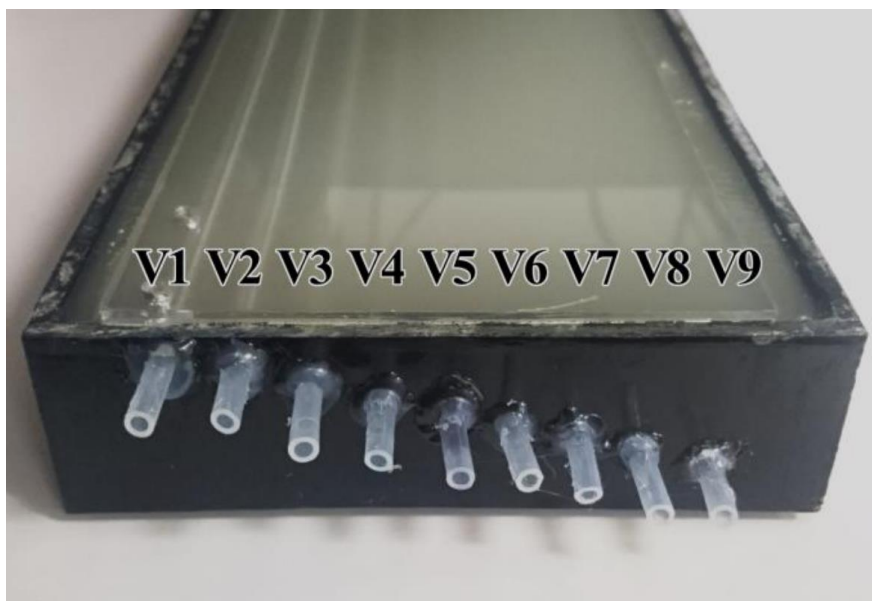


Figure 46 Homogenous pulsatile phantom with multiple vessels and increasing depths from 3.2 mm (V1) to 24.4 mm (V9). See Table 1 for all Vessel depths.

7.2.1 Protocol

The methodology for the investigation using the phantom involved a series of carefully orchestrated steps:

1. **Temperature Normalization:** The phantom was taken out of refrigeration and allowed to acclimatize to room temperature for 30 minutes.
2. **Network Connection:** It was then integrated into the arterial network, ensuring the pressure transducer was connected at the inflow point.

3. **Reservoir Preparation:** The pump reservoir was filled with a solution comprising water and black India ink. The ink was chosen for its capacity to provide a consistent baseline of absorption across a broad range of wavelengths.
4. **Emitter-Detector Placement:** The arms of the translation bridge, holding the emitter and detector, were positioned directly above the phantom's first vessel. They were initially set at the minimum possible separation distance of 2 mm (centre-to-centre).
5. **Light Blocking:** To minimize ambient light interference, all exposed areas of the phantom were covered with a black material.
6. **Data Recording:** The translation bridge was activated, automating the process of sequentially recording 60 seconds of data at each separation distance. The distance between the emitter and detector was increased in 0.1 mm increments until a separation of 8 mm was achieved.
7. **Sequential Measurements:** After completing measurements for one vessel, the phantom was reconnected to the arterial network at the next vessel, and the measurement sequence was repeated for each of the remaining eight vessels.

The entire system setup, as detailed above, is depicted in Figure 47. The collected raw PPG data was subsequently analysed using a custom MATLAB script in an offline environment. This methodical approach ensured a comprehensive and precise investigation of the impact of separation distance and vessel depth on PPG signal characteristics.

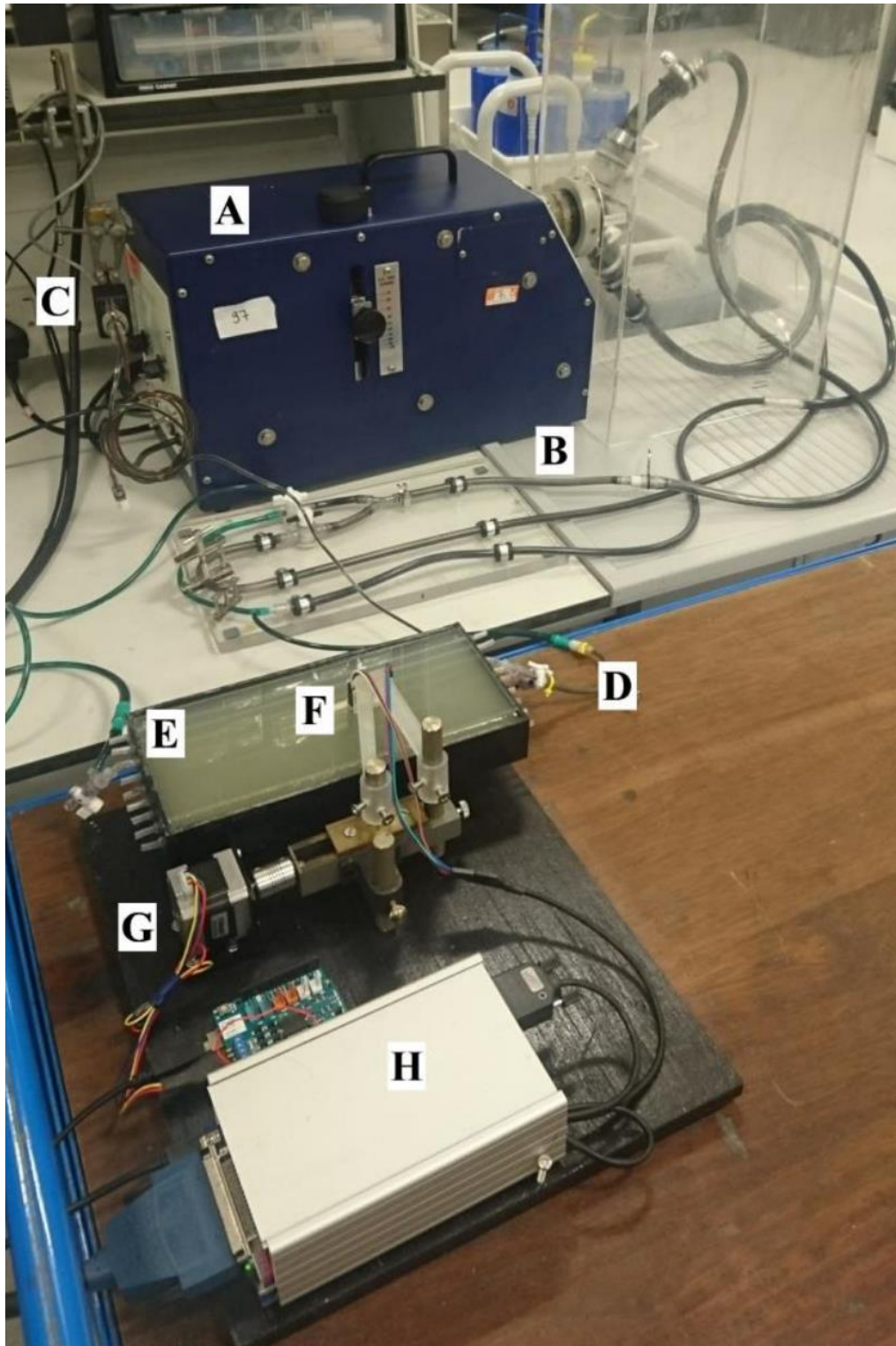


Figure 47 In- vitro investigation setup. The pulsatile pump (A) connected to the arterial network (B) with a pressure transducer (C) attached at the inflow of the phantom (E). The emitter and detector were held by the bridge (F). The separation distance between them is controlled by the translation bridge (G) and the signal was acquired by the ZenPPG (H).

7.3 Results

The signals obtained in the study were down sampled and filtered through a band-pass Finite Impulse Response (FIR) filter, ranging from 0.5 to 5 Hz. Figure 48 showcases an eight-second snapshot of these filtered signals from each vessel depth, specifically focusing on a 4 mm emitter-detector separation distance. The signal from Vessel 1 (V1), the closest to the sensor at a depth of 3.2 mm, displayed a typical PPG waveform characterized by a distinct dicrotic notch and the highest amplitude observed at 4.3 Vpp. It was noted that the signal amplitude decreases progressively with increasing vessel depth.

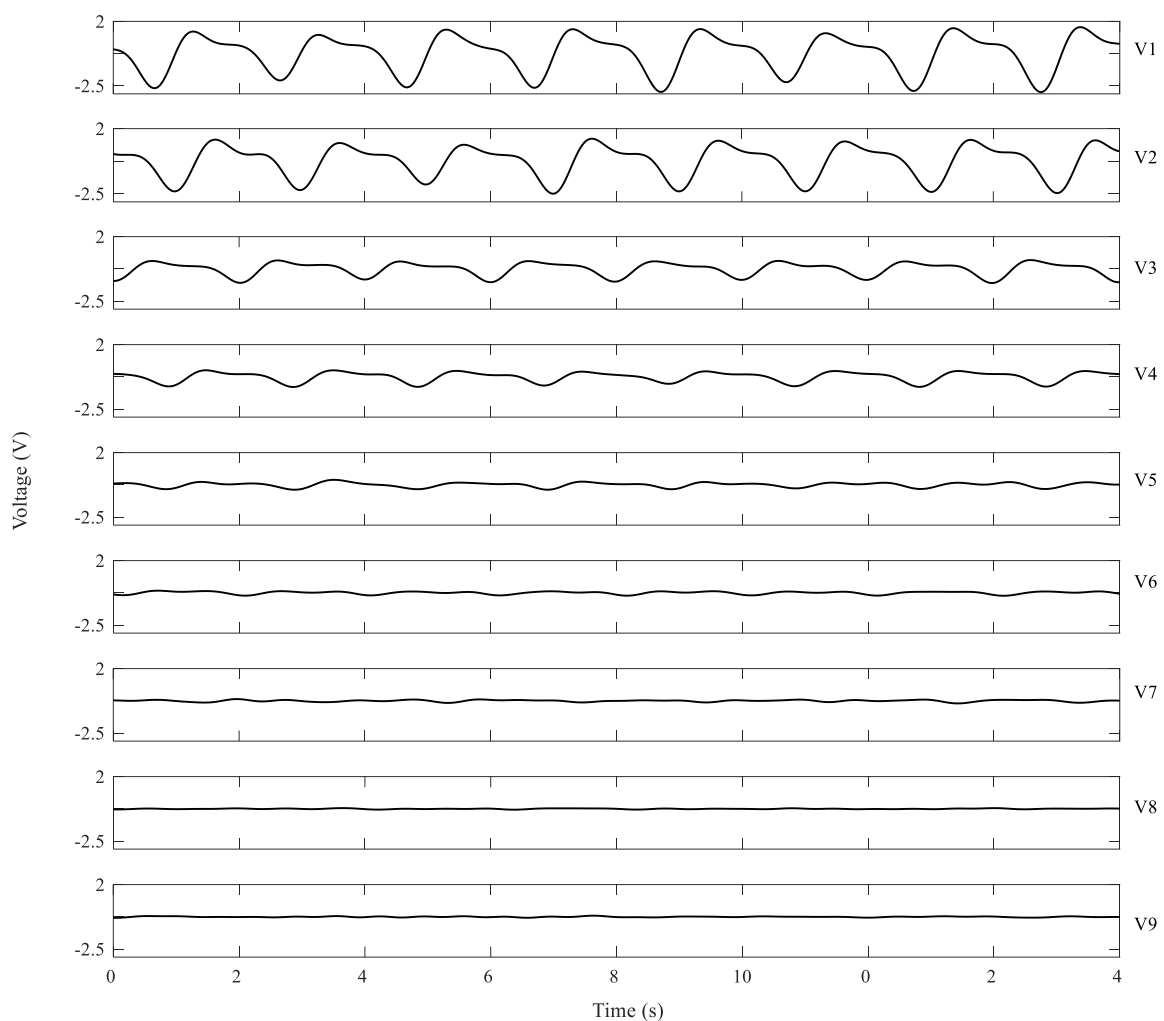


Figure 48 An eight second window of the filtered PPG signals at 4 mm

To evaluate the quality of PPG signals at various depths and separation distances, the Root Mean Square (RMS) amplitude was calculated for each, as depicted in Figure 49. The highest quality signals, indicated by large amplitudes, were recorded in V1 at a separation distance of

3.8 mm. The peak amplitudes for V3 and V4 were found at separation distances of 4.35 mm and 4.4 mm, respectively. This trend of increasing optimal separation distance correlating with greater vessel depth becomes less pronounced from Vessel 5 (V5) onwards, situated at a depth of 12.5 mm. In Fig. 4, the shift of the optimal peak to the right (indicating an increase in separation distance) coincides with a broadening of the peak's shape, eventually leading to an indiscernible peak in the response at V5. Vessels V1 to V4 all yielded clear PPG signals with signal-to-noise ratios (SNR) exceeding 22 dB, as shown in Table 5. Though Vessels V5, V6, and V7 still exhibited noticeable PPG waveforms, there was a notable reduction in their amplitudes. The deeper Vessels V8 and V9, however, failed to produce detectable PPG signals.

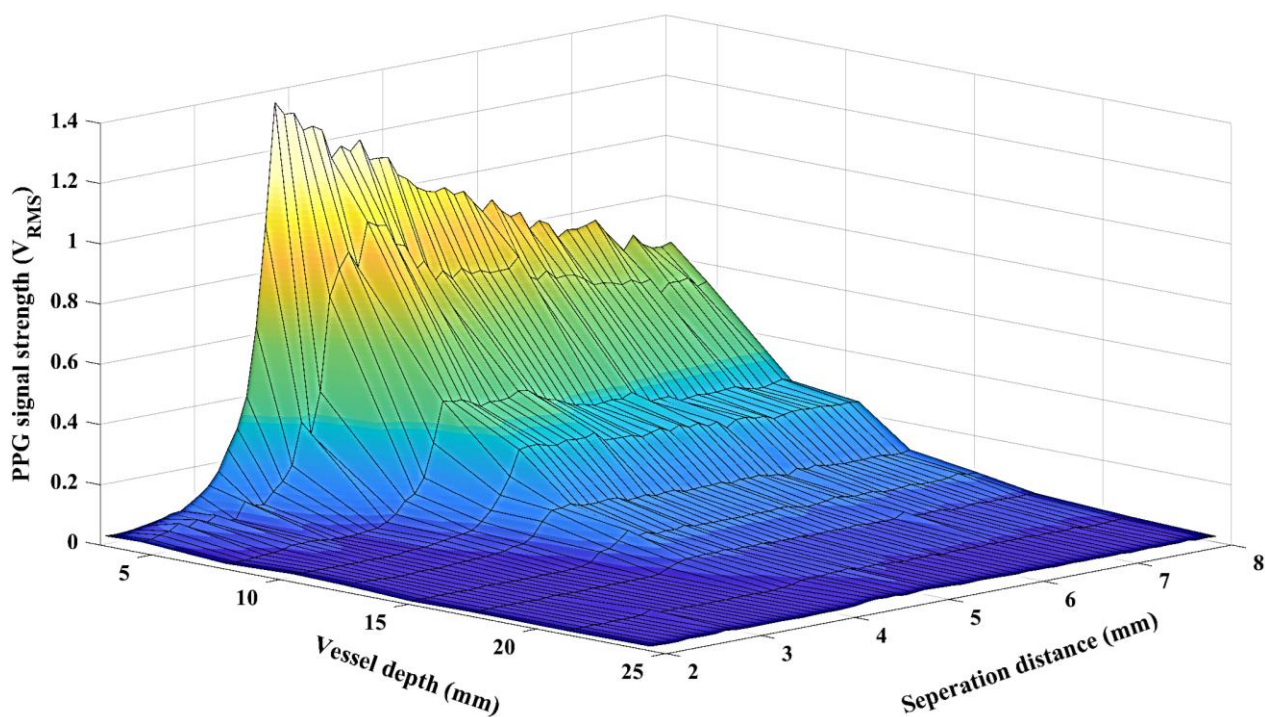


Figure 49 A 3D surface plot of the PPG signal strength against both variable parameters. Separation distance (mm) (x-axis). Vessel depth (mm)(y-axis).

Table 5 Signal-to-noise ratio for all vessel depths

Vessel	Depth (mm)	Maximum Signal-to-Noise Ratio (dB)
V1	3.2	28.16
V2	4.6	26.35
V3	7.9	23.07
V4	10.5	22.19
V5	12.5	14.79
V6	15.1	13.21
V7	17.4	9.83
V8	21.1	2.77
V9	24.4	1.82

The study concludes that for vessel depths less than 10.5 mm, optimal IR PPG signals are attainable when the separation distance between the emitter and detector ranges from 3.8 mm to 4.4 mm. For vessels deeper than 10.5 mm, although PPG signals are present, they exhibit SNRs below 20 dB, which could potentially impact the reliability of both qualitative and quantitative signal analysis.

Summary

This study, utilizing a brachial gelatine phantom with varying vessel depths, serves as a foundational exploration into how vessel depth and emitter-detector separation affect PPG signal quality. By processing and analysing signals from nine vessels with depths ranging from 3.2 mm to 24.6 mm, we discovered optimal PPG detection at shallower depths, specifically when the emitter-detector separation was between 3.8 mm and 4.4 mm. The research highlights a depth limitation for IR PPG signal detection in deeper vessels.

Crucially, this investigation marks a significant starting point for more detailed studies. The insights gained lay the groundwork for further research aimed at unravelling the complexities of PPG signal origin. Future investigations, building on these initial findings, can delve deeper into the nuances of light-tissue interaction and the factors influencing PPG signal characteristics. This progression of research is vital for advancing our understanding of PPG technology, potentially leading to enhanced sensor designs and more accurate health monitoring applications, especially considering the variability in human anatomy and sensor placement.

8

Investigating Haemodynamic Properties

8.1 INTRODUCTION	114
8.2 IN-VITRO SYSTEM SETUP	114
8.2.1 DRIVING THE PUMP	116
8.2.2 VERIFICATION	117
8.3 PPG ANALYSIS	122
SUMMARY	125

8.1 Introduction

In this chapter we focus on fundamental investigations of Haemodynamics and utilise their response as a method of validation for the developed in vitro system. Ultimately, the investigations in this chapter demonstrate the ability of the in-vitro system to be employed in potential investigations of PPG sensor technologies against a pulsatile phantom where properties of the phantom or the pump can be altered to investigate different pathologies.

8.2 In-vitro System Setup

The set up for the in-vitro experiment follows the windkessel model, a widely used model for estimating the overall compliance of a systematic arterial system [173] Figure 50 (a) shows the actual physical setup of the pump with the diagrammatic representation of all major components. The pump is a pulsatile fluidic pump from BDC Labs (Wheat Ridge, CO, USA), driven by a computer-controlled linear motor. Isolation between the pump head and pulsatile fluid is achieved by a fluid isolation module. This facilitates the pumping of liquids that may otherwise interfere with the operation of the motor, including biological fluids (blood, serum, and plasma), fluids with particle suspensions and Phosphate Buffered Saline (PBS) solutions. The pulsatile fluid sits in a chamber that can be pressurised and heated to effectively control overall compliance and offer control over liquid viscosity. The outlet feeds an artificial Aortic vessel (ID = 40 mm, vulcanised rubber). A single tap off the Aortic vessel feeds a brachial

vessel (ID = 2.4 mm, silicone). The brachial vessel is stepped down to the finger tissue-vessel phantom model under test. See chapter 6 figure 33.

The outlet of the phantom is stepped back up to a brachial vessel before returning to the vena-cava vessel on the opposite side of a resistance clamp that is designed to simulate the reflection of the Iliac artery (Iliac Reflection Clamp IRC). Before returning to the pump for recirculation, the fluid passes a total peripheral resistance (TPR) clamp designed to simulate whole body peripheral resistance on the pulsatile fluid. Figure 50 (b) shows the systems setup diagrammatically highlighting the inline pressure transducers placed on the compliance chamber, to the input of the brachial feeding the phantom, and on the outlet of the phantom.

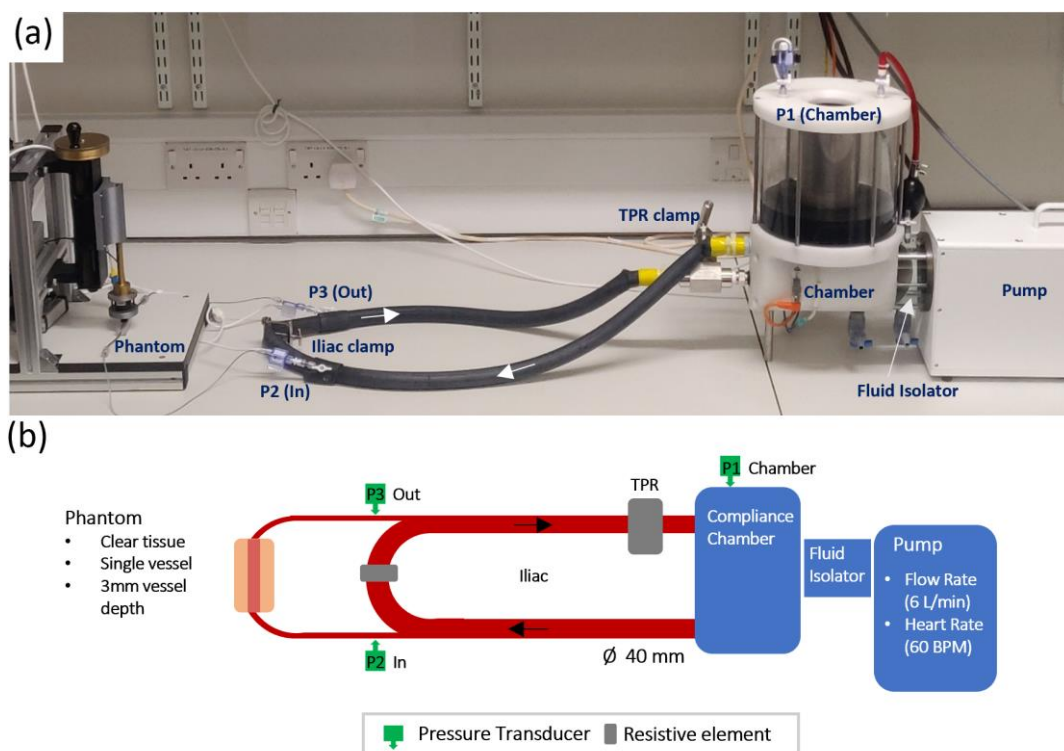


Figure 50 Pump setup. Actual in-vitro lab setup (a), with diagrammatic representation of all major components (b).

Table 6 Specification for the BDC pump and its pressure transducers

PD-1100 Pulsatile Pump	
Mean Flow Rate @ 60 BPM	0-10 L/min
Max Stroke Volume	290 mL
Driving Waveforms	Arbitrary and Sine
Working Fluid	Water, PBS, Blood Analog
Frequency	2 Min BPM
	240 Max BPM
Power Requirements	120 VAC
	20 A max
Reservoir	10 L
BDC Pressure Transducers	
Accuracy	±2% of reading in the range of 0 to 310 mm Hg
Pressure Range	-362 to 3878 mmHg
Nominal Sensitivity	5 µV/V/mmHg

8.2.1 Driving the Pump

One of the considerations in the windkessel model is the 'bell-shaped compliance curve vs. pressure curve' which follows the bell-shaped pressure vs compliance relationship as shown below [49]:

$$C[P_c(t)] = \frac{C_m}{1 + \left[\frac{P_c(t) - P_0}{P_1} \right]^2}$$

Eq. 8.1

Where $P_c(t)$ is the instantaneous pressure over the model compliance, P_0 is the maximum pressure calculated at the bell-shape relationship between the pressure and compliance, $C[P_c(t)]$ is the compliance calculated at the instantaneous pressure, C_m is the maximum compliance that is found when $P_c(t) = P_0$; and P_1 is the half-width pressure so that compliance is reduced to $\frac{C_m}{2}$ at $P_0 \pm P_1$.

The parameters in the above experiment are subjected to the sample studied. In the current experiment, however, a bell-shape pressure pulse is driven through the pump following the general normal distribution formulation as shown below:

$$f(x, \mu, \sigma) = \frac{1}{\sigma \sqrt{2\pi}} e^{-\frac{(x-\mu)^2}{2\sigma^2}}$$

Eq. 8.2

Where μ and σ are the mean and the standard deviation, respectively. Figure 51 shows the generated bell curve from the above-described models.

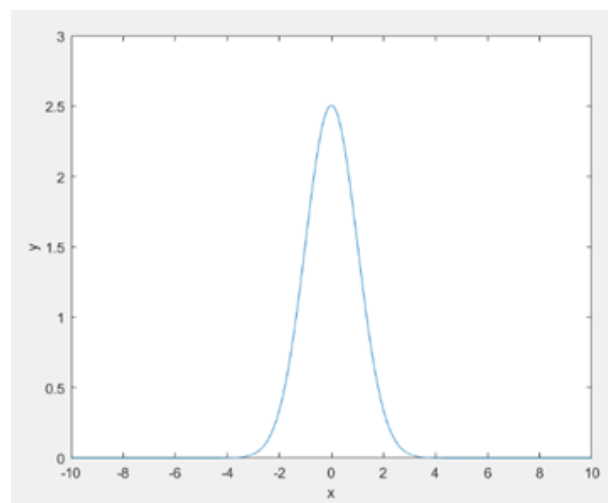


Figure 51 Bell curve generated using Eq 8.1 & Eq. 8.2, implemented in MATLAB (TheMathworks, USA). Units are arbitrary.

8.2.2 Verification

Using the Windkessel model as a reference guide to the arrangement of the pump circuit, the pump actuator was driven with a bell curve and the pressure transducers were connected at three different locations.

To verify the effectiveness of the resistance elements in our pump circuit, PPG signals were taken from the clear silicone phantom with custom a radial vessel at the four resistance configurations. The pump was set to this investigations' standard output flow of 7 L·min⁻¹ at 60 bpm. The bell curve described above was programmed into the pump and run under the following resistance conditions:

- i. IRC open, TPR open
- ii. IRC open, TPR restricted
- iii. IRC restricted, TPR open
- iv. IRC restricted, TPR restricted

Figure 52-Figure 55 display the driving signal of the pump with the consequent pressure signals in the fluid chamber, pre-phantom and post-phantom locations (under all four resistive conditions). The results demonstrate that the dicrotic notch visible at pre-phantom and post phantom are a direct result of the resistance elements, as the dicrotic notch is not witnessed inside the fluid chamber. Figure 56 shows the resulting PPG signals obtained from the phantom under all four resistive conditions. The restricted position of each resistance element was an 80% reduction in the vessel diameter from 40 to 8 mm.

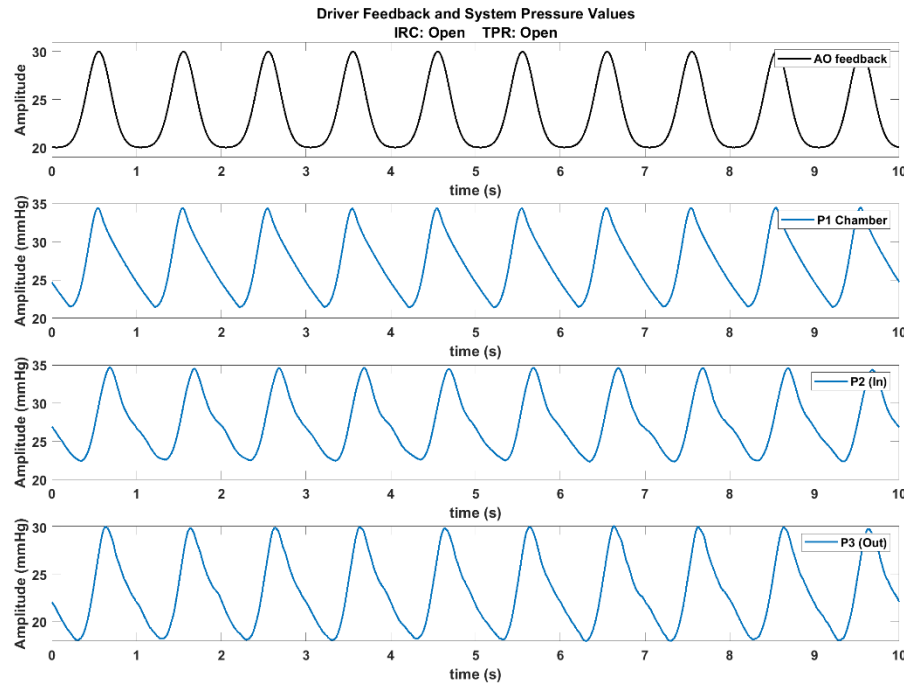


Figure 52 The analogue feedback from the driving waveform (AO feedback), and the pressure waves produced under the resistive condition i. (IRC=Open, TPR=Open) in the system at three locations: the compliance chamber (P1), pre-phantom (P2) and post-phantom (P3).

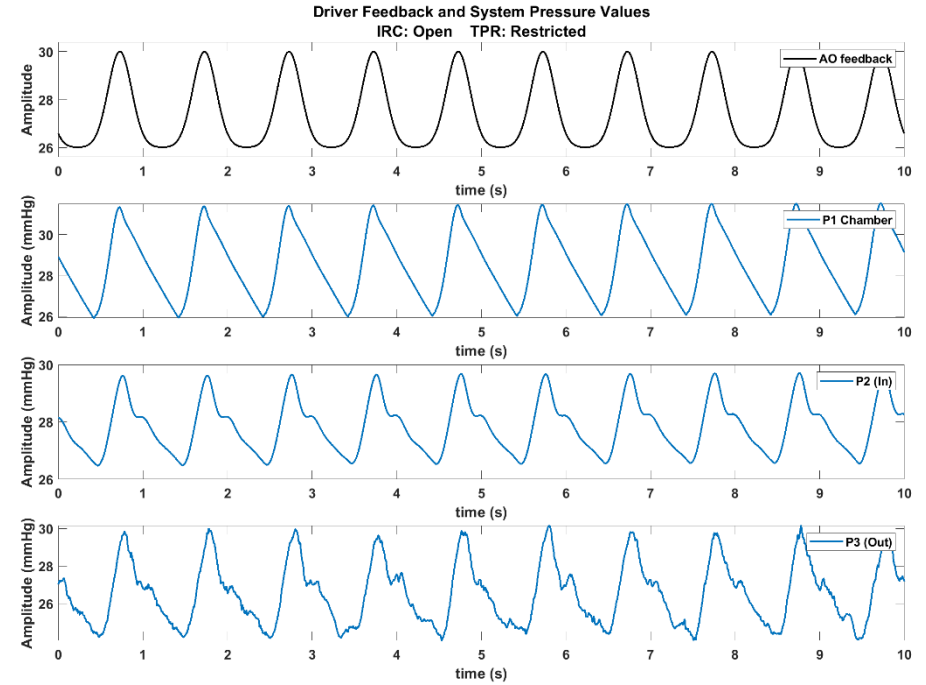


Figure 53 The analogue feedback from the driving waveform (AO feedback), and the pressure waves produced under the resistive condition ii. (IRC=Open, TPR=Restricted) in the system at three locations: the compliance chamber (P1), pre-phantom (P2) and post-phantom (P3).

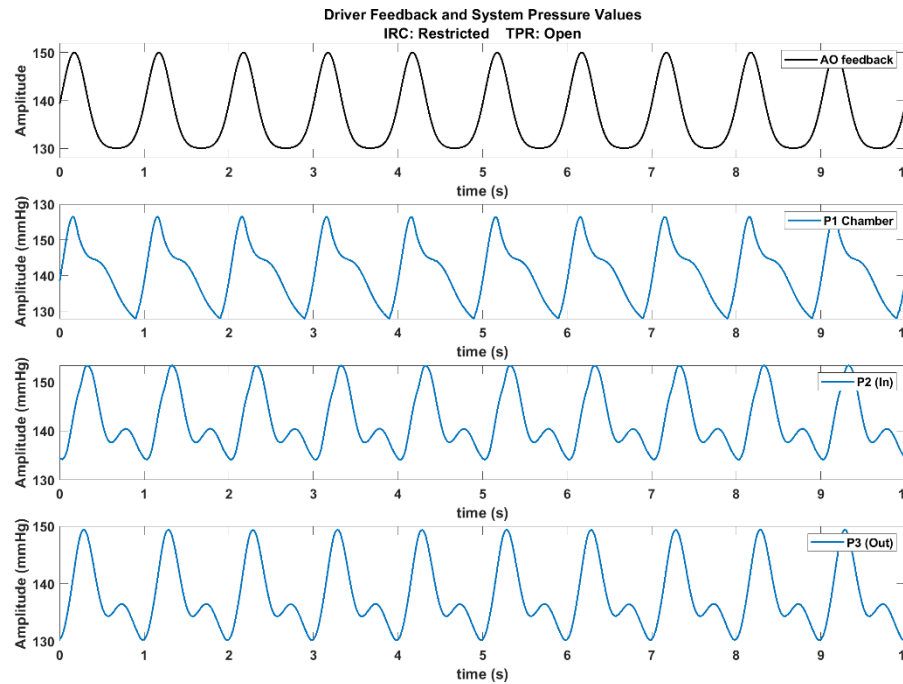


Figure 54 The analogue feedback from the driving waveform (AO feedback), and the pressure waves produced under the resistive condition iii. (IRC=Restricted, TPR=Open) in the system at three locations: the compliance chamber (P1), pre-phantom (P2) and post-phantom (P3).

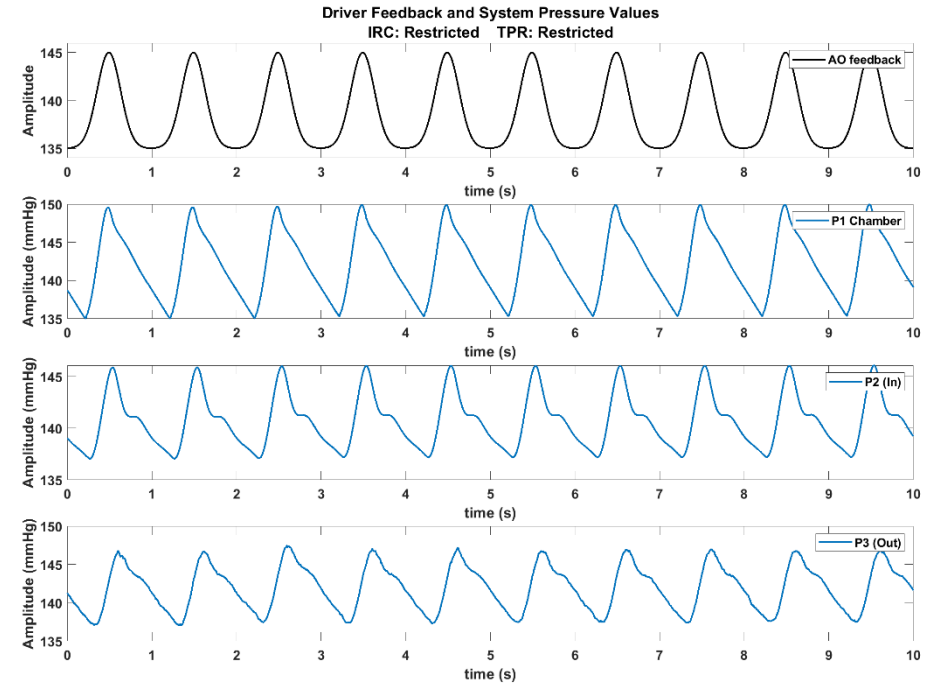


Figure 55 The analogue feedback from the driving waveform (AO feedback), and the pressure waves produced under the resistive condition iv. (IRC=Restricted, TPR=Restricted) in the system at three locations: the compliance chamber (P1), pre-phantom (P2) and post-phantom (P3).

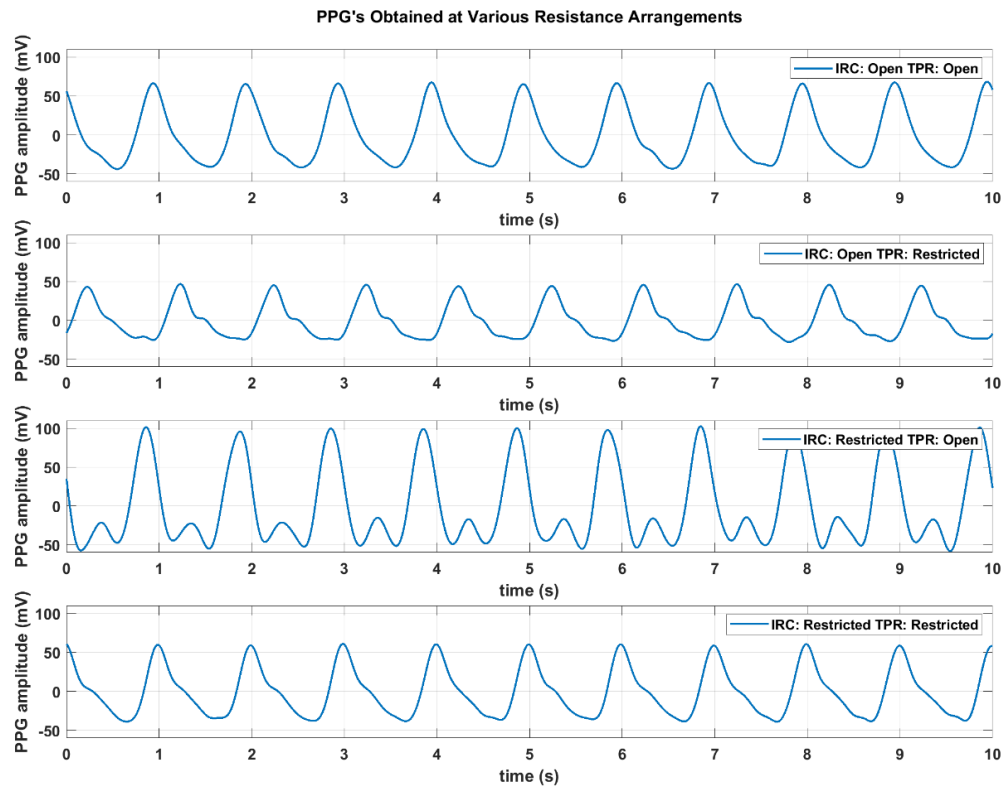


Figure 56 The PPG's detected at the pre-phantom (P2) pressure transducer for different combinations of resistive elements positions. (a) Iliac Resistive Component (IRC) and Total Peripheral Resistance (TPR) both unrestricted. (b) IRC unrestricted, TPR restricted. (c) IRC restricted, TPR unrestricted. (d) IRC and TPR restricted.

The PPG's produced at each configuration are shown to have widely varied morphology, see Figure 56. The dicrotic notch is not produced when both IRC and TPR are in their open positions. The notch can be seen in all three of the other configurations. IRC (open) TPR (restricted) produced the most exaggerated dicrotic notch, this causes the PPG signal to separate the reflectance wave from the initial wave. The configuration of peripheral resistance that produces the most standard PPG signal, is when both IRC and TPR are in their restricted position, in this position the morphology and amplitude are most ideal. In this configuration the pressure transducer placed in the fluid chamber shows the pressure waveform to be 15 mmHg in amplitude with a steep incline and sharp peak at 125 mmHg (Figure 55). The fluid then branches off into the phantom where the second pressure transducer measures an amplitude of 15 mmHg but has a max peak of 122 mmHg, a small reduction from the pressure in the chamber. The waveform exhibits a dicrotic notch, caused by the distended tubing recoiling. The pressure wave loses energy as it travels through the phantom and is measured to have an

amplitude of 10 mmHg peaking at 97 mmHg at the junction where flow re-enters the main circuit.

It is also vital to understand the relationship between heart rate, flow rate and the resulting blood pressures in the system. The resultant pressure amplitudes pre-phantom of different heart rates and flow rates are presented in Figure 57. Figure 57 (a) shows the resulting blood pressures of heart rates ranging from 40 to 120 bpm at a constant flow rate of 6 L·min⁻¹. Figure 57 (b) shows the resulting blood pressure of flow rates ranging from 1 to 12 L·min⁻¹ at a constant 60 bpm. These graphs show the maximum and minimum recorded pressure amplitudes at each level, with the calculated mean arterial pressure (MAP) indicated.

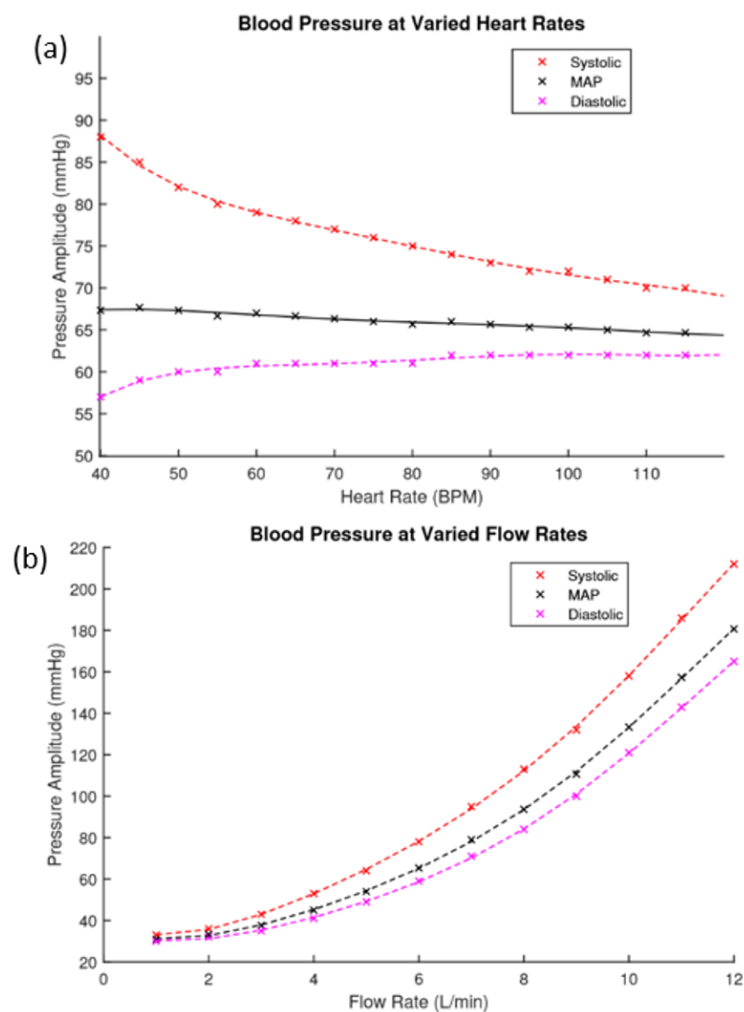


Figure 57 (a) This figure plots the blood pressure values pre-phantom against varied heart rates. (b) This figure plots the blood pressure values pre-phantom against varied flow rates.

In the in-vitro setup, the pump software allowed the user to input the heart rate and flow rate. These parameters and their effect on pressure were investigated. Increasing the heart rate had little impact on the mean arterial pressure, it largely affected the systolic and diastolic

values. Increasing the heart rate increased the diastolic pressure but decreased the systolic pressure. So, although MAP remains steady, the peak to peak amplitude of the pressure signal was reduced. The biological response is comparable to this result, as the human heart rate fluctuates throughout the day, our blood pressure remains mostly unaffected by it. The compliance of arteries can adapt to the changing heart rate and regulate blood pressure. The investigation proves that the in-vitro system can regulate a steady MAP at different heart rates, and the flow rate impacts the pressure the most.

8.3 PPG Analysis

The silicone phantom described in chapter 6 was used to take PPG results at the range of heart rate and flow rate values described in Figure 57. The Raw AC signals recorded from the ZenPPG acquisition system were digitally filtered and the mean amplitude of three-minute recordings were obtained using three second window averaging. Figure 58 displays the mean PPG amplitudes at varied heart rates. The trend line observed clearly shows there is a negative correlation. Figure 59 shows the positive correlation between flow rate and mean PPG amplitude.

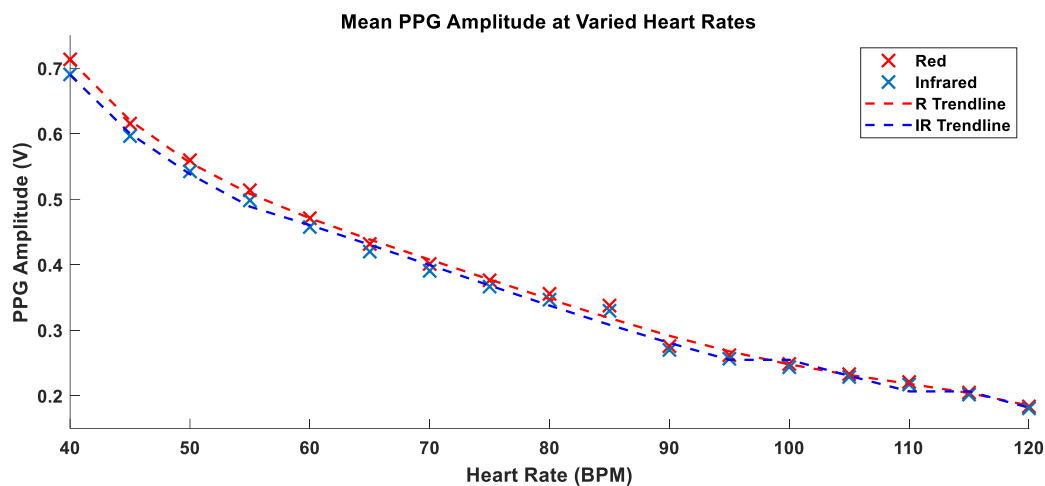


Figure 58 The mean PPG amplitude of three-minute samples with $6 \text{ L}\cdot\text{min}^{-1}$ flow and heart rates from 40–120 BPM (all $SD < 0.003$).

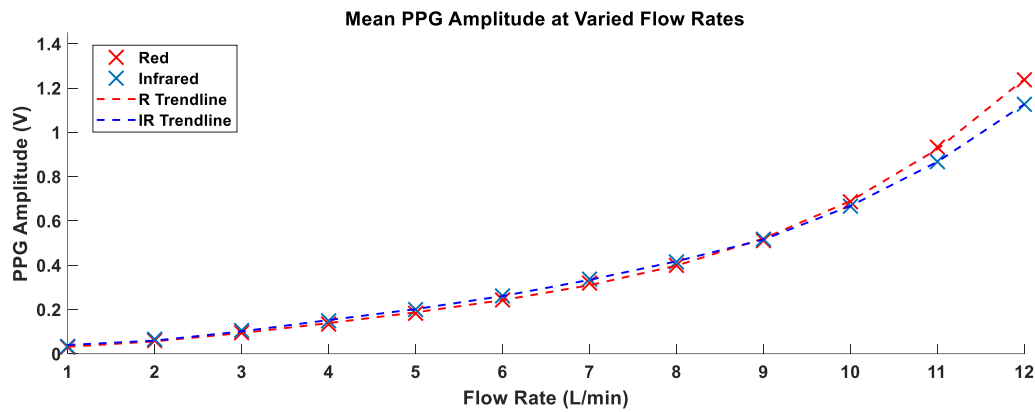


Figure 59 The mean PPG amplitude of three-minute samples with 60 BPM heart rate and flow from 1–12 L·min⁻¹ (all SD < 0.003).

PPGs obtained at all the heart rate and flow rate values implemented were plotted and the trends displayed fitted the expected outcome of the volumetric model. Chan et al describe the fundamental principle of PPG where the AC component of the signal is mainly attributed to the volume changes that occur in the vessels [151]. Increasing the heart rate, ultimately reduced the amplitude between systole and diastole (see Figure 58), which in turn reduced the distention of the vessels. This resulted in less volume of fluid therefore reducing the amplitude of the PPG. The volumetric model is again evident in the flow rate investigation. The increase of flow rate resulted in a larger volume of fluid per stroke. This positive correlation is seen in Figure 59.

In another study, we examined how variations in blood pressure influence the morphology of photoplethysmography (PPG) signals. We specifically focused on altering blood pressure by adjusting the iliac and peripheral resistance clamps, while maintaining a constant heart rate and flow rate at 60 bpm and 6 L/min, respectively.

For this analysis, we isolated a single PPG wave and plotted it against each blood pressure level see Figure 60. The resulting comparisons, as shown in our findings, clearly demonstrate significant changes in PPG wave morphology with varying blood pressure, despite keeping the flow rate and heart rate constant. It becomes evident that altering the resistance in the system to simulate different blood pressure states has a profound impact on the shape of the PPG signal. Due to the controlled nature of the invitro setup, cycle to cycle the waveform showed negligible variation.

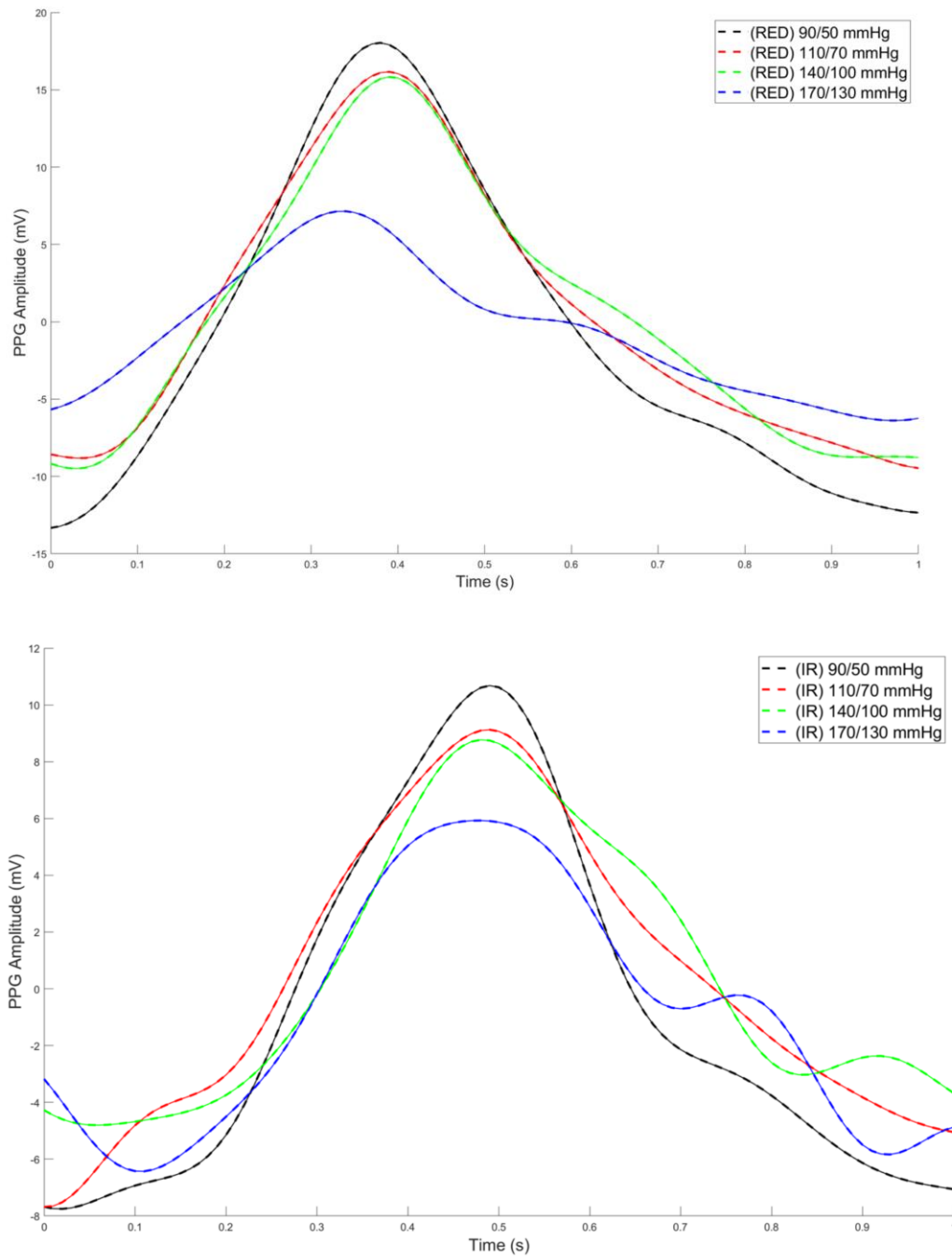


Figure 60 Red (left) and infrared (right) PPGs from the finger phantom at four different blood pressure ranges; 90/50 mmHg (black), 110/70 mmHg (red), 140/100 mmHg (green) and 170/130 mmHg (blue).

The significant influence that each parameter has on the PPG signal highlights the necessity of isolating and examining each factor thoroughly to gain a deeper understanding of PPG signal dynamics.

Summary

The in-vitro system was set up to allow individual control over its parameters. Through the adaptation of a Windkessel model, used to describe the function of the heart and the compliance of arteries to produce the arterial pressure wave, a versatile in-vitro pump circuit has been developed. A bell curve drives the actuator, pushing fluid from the chamber into the circuit. The morphology of the acquired PPG was dependant on the configuration of the resistance elements. When both elements remain unrestricted, the PPG displays no notch. Restriction of the TPR element only, produced a notch in the waveform and resulted in a lower amplitude PPG signal. Restriction of the IRC element caused a large increase in the systolic peak of the PPG, where the notch is dramatically defined. The combined restriction of both elements produced a waveform that closely resembles the “textbook” PPG/blood pressure waveform. In this chapter, we have demonstrated the versatility of our setup and how physiological parameters such as heart rate, flow rate and vascular resistance impacts the resultant pressure and PPG signals. These studies outcomes underscore the importance of considering each parameter independently in advanced PPG phantom research.

9

Investigating Arterial Compression

9.1	INTRODUCTION	126
9.2	METHODOLOGY	127
9.2.1	PROTOCOL.....	128
9.3	RESULTS	130
	SUMMARY	135

9.1 Introduction

In this pivotal chapter of the thesis on 'Novel Pulsatile Phantoms in Photoplethysmography,' we explore the nuanced interaction between externally applied contact pressure and its effects on photoplethysmography (PPG) signal amplitude across a spectrum of blood pressure levels, ranging from hypotensive to hypertensive states. This investigation delves into the critical understanding of how varying degrees of arterial compression, induced by contact pressure, correlate with PPG signal responses under different blood pressure conditions and understanding oscillatory shifts.

The primary aim of this chapter is to systematically analyse how contact pressure affects PPG signal amplitude at distinct blood pressure levels. This is achieved by employing a protocol where contact pressure is incrementally applied until arterial occlusion and then released, across six blood pressure categories. This approach enables a comprehensive examination of the PPG response under varying degrees of compression and blood pressure states, providing a clearer picture of the PPG signal behaviour in diverse physiological conditions.

This investigation is crucial not only for enhancing the accuracy of PPG-based blood pressure measurements but also for underpinning the validity of the pulsatile phantoms developed in this thesis. By identifying the optimal contact pressure for the best PPG signal quality at various blood pressure states, we can improve the reliability of PPG in clinical diagnostics and personal health monitoring, while simultaneously validating the utility and accuracy of the

developed phantoms. The insights from this study are expected to significantly contribute to the design and application of PPG technology and the future development of more refined and versatile pulsatile phantoms.

9.2 Methodology

This study aims to investigate the impact of varying contact pressure on Photoplethysmography (PPG) signal amplitude across different simulated blood pressure states. The study hypothesizes that different levels of contact pressure applied to the phantom will result in observable changes in PPG signal amplitude, with these changes varying across simulated blood pressure states. The experiment involves simulating six distinct blood pressure states within the phantom. This is achieved by adjusting the total peripheral resistance in the in-vitro system to create conditions equivalent to hypotension, normotension, pre-hypertension/low hypertension, stage 1 hypertension, and stage 2 hypertension.

This setup, derived from the research presented in Chapter 8, has been refined to utilize the minimum necessary components for modifying the bell pressure waveform output of the pump. This modification is aimed at closely emulating the morphology of a blood pressure waveform. The system incorporates two critical resistance clamps: one is designed to simulate the reflection of pulsatile pressure waves at the aortic bifurcation into the Iliac artery, and the other to represent total peripheral resistance. This streamlined setup, see Figure 61 effectively replicates key aspects of the cardiovascular system's haemodynamics, essential for our investigation.

P1 = Main Pump Pressure
 P2 = Outflow pressure from pump (Pre Iliac Clamp)
 P3 = Phantom inflow pressure
 P4 = Phantom outflow pressure
 P5 = Post Iliac Clamp Pressure

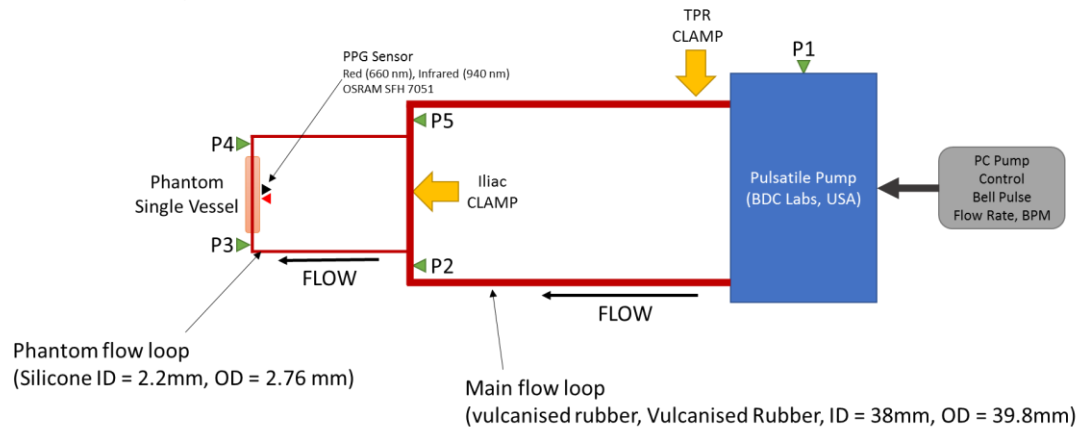


Figure 61 Pulsatile flow rig diagram for compression study.

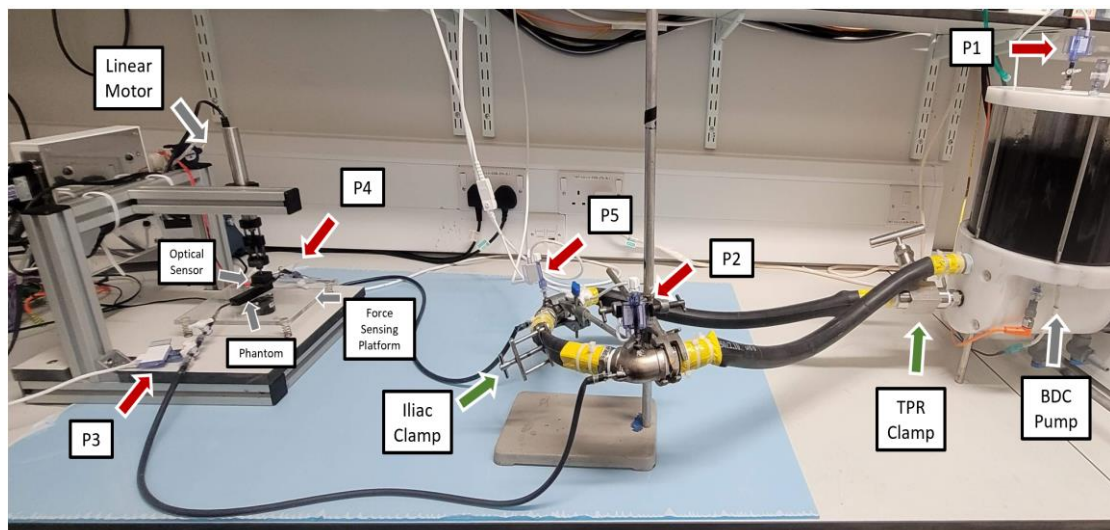


Figure 62 Photo of pulsatile flow rig set-up. The optical sensor is attached to the DPPGS V2 system described in chapter 5.

Figure 63 showed the updated invitro system first described in chapter 5. One main arterial loop contains most of the blood flow. Two metal elbow joints are used to branch off a single brachial branch providing flow to the phantom. P1-P5 indicate the pressure transducer locations.

9.2.1 Protocol

To investigate the effect of varying contact pressure on the PPG signal, a blood-mimicking fluid (distilled water and India ink solution) was continuously pulsed through the phantom via a branching circuit from a simplified human arterial network. The pulses were timed at 60

BPM (1 Hz) using a custom bell-pulse profile, previously outlined in chapter 8. Six blood pressure states were implemented by varying the flow rates outputted by the pump. These pressures ranged from hypotensive, to stage 2 hypertensive conditions, and were confirmed by reading the pressure at the input of the phantom for 30s prior to the main experiment. The systolic blood pressure (SBP), diastolic blood pressure (DPB), and mean arterial pressure (MAP) produced are reported for each state in Table 7.

Table 7 Measured pressures in each blood pressure state at the input of the phantom.

Flow Rate (L/min)	Blood Pressure (SBP/DBP) (mmHg)	MAP (mmHg)	Blood Pressure Classification
6	77/53	61.0	HYPOTENSION
7	92/63	72.3	NORMOTENSION (LOW)
8	110/76	87.3	NORMOTENSION
9	130/91	117.3	PRE-HYPERTENSION/HYPERTENSION (LOW)
10	152/110	138.7	STAGE 1 HYPERTENSION
11	175/130	145.0	STAGE 2 HYPERTENSION

On confirmation that the correct pressure-state had been established, the linear actuator descended the PPG sensor into the phantom at a rate of 0.03 mms^{-1} , starting just above the phantom surface. The sensor was withdrawn once it had reached the depth of the vessel (3 mm), ensuring that the vessel had been completely occluded. PPG signals were recorded simultaneously with the load cell voltage and repeated 3 times.

All signals were sampled at 1 kHz and were processed offline in MATLAB® (The MathWorks, Natick, MA, USA). A sample signal profile is shown in Figure 63. The corresponding labels identify the various events that occur:

- A) PPG signal just above surface of phantom before force is applied
- B) PPG sensor makes contact with phantom
- C) PPG Signal is observed to flip orientation (TFLIP1)
- D) Maximum PPG amplitude during force application (TMAX1)
- E) Vessel becomes occluded (TOCC)
- F) Force actuator switches direction to start releasing pressure
- G) Vessel becomes un-occluded and PPG returns (TRETURN)
- H) Sudden PPG amplitude increase (TRUSH)
- J) Maximum PPG amplitude during release of force on phantom (TMAX2)

K) PPG Signal is observed to flip orientation again

L) PPG Sensor breaks contact with phantom, remain PPG signal is that observed just above the surface with no applied force.

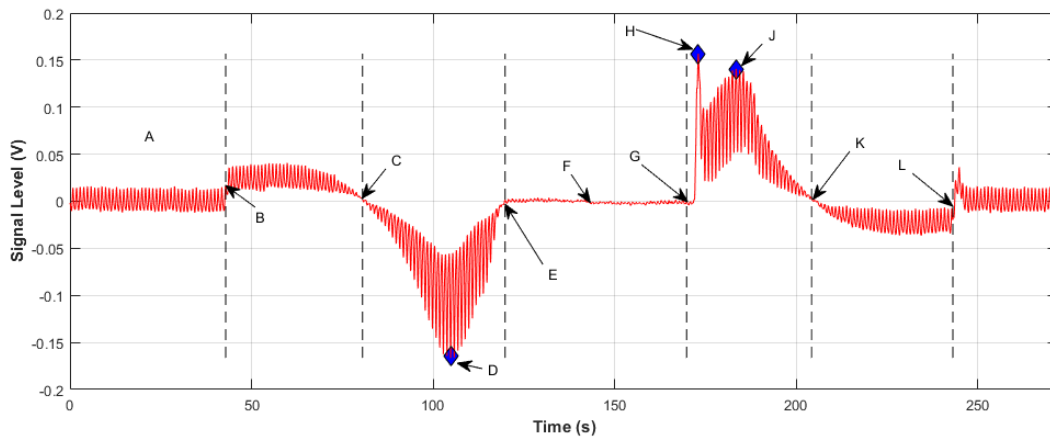


Figure 63 : Application and Release of force on a vessel-tissue phantom signal profile.

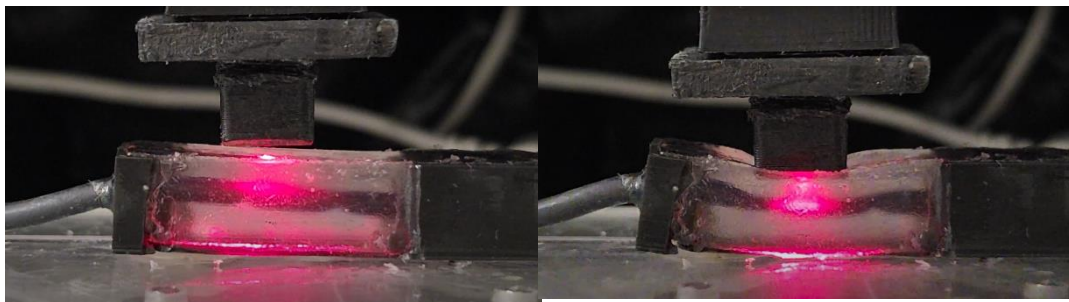


Figure 64 side profile view of phantom taken at (left) stage A of the protocol where the sensor is just above the surface, and (right) stage E where it occludes the flow.

9.3 Results

Informed by Nitzan's research [174], our study investigates the efficacy of photoplethysmography (PPG) as an enhanced method for non-invasively measuring systolic blood pressure. Nitzan's work suggests a correlation between oscillometric peak points and PPG signals, a concept central to our analysis. Our experimental approach involves Identifying the oscillometric peak in two instances: firstly, as we apply force to simulate increasing cuff pressure, and secondly, as the force is released, allowing blood flow to resume. Figure 66 shows the oscillometric pulse effect.

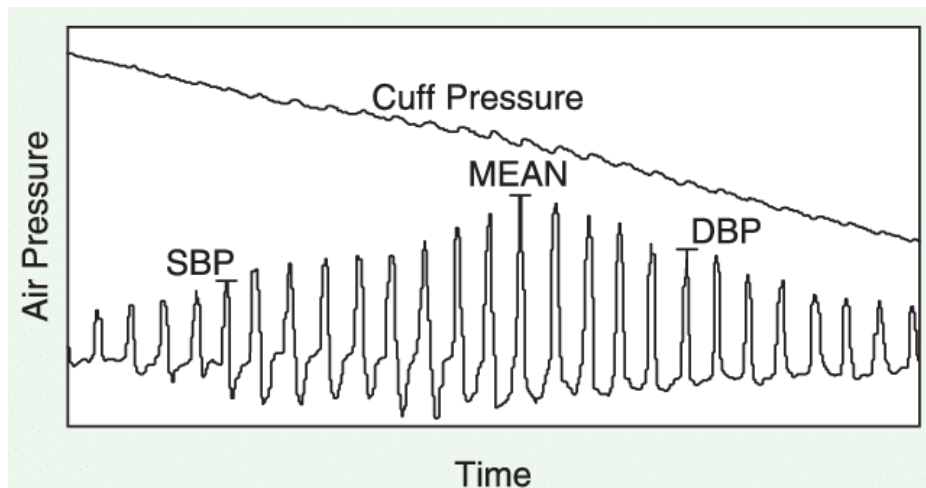


Figure 65 Oscillometry: The oscillometric pulse effect that occurs in sphygmomanometer as cuff pressure deflates.

Referring to Figure 63 in our study, we observe two critical points of interest. Point D (TMAX1) marks the maximum amplitude observed during the application of force. The second oscillometric peak is noted at point J (TMAX2), which occurs during the release of the applied pressure. This dual observation provides a comprehensive perspective on the PPG signal's response to varying degrees of arterial compression.

Building upon our experimental design, we extracted and evaluated data specifically at these two pivotal points, TMAX1 and TMAX2. This focused analysis was conducted to gain a deeper understanding of the PPG signal's behaviour under varying arterial compression conditions. Figure 66 Iteration Plots for Hypotensive Flow Experiment. Each graph in this series of six shows one iteration of the experiment under hypotensive conditions undergoing applied pressure, with the PPG signal in blue and load cell data in orange. TMAX 1 is indicated on each plot and the corresponding force is recorded. and Figure 67 presents the responses from the six iterations of our experiment conducted under hypotensive conditions. In this figure, we have plotted the data captured by the load cell, and highlighted the peak points identified during each iteration.

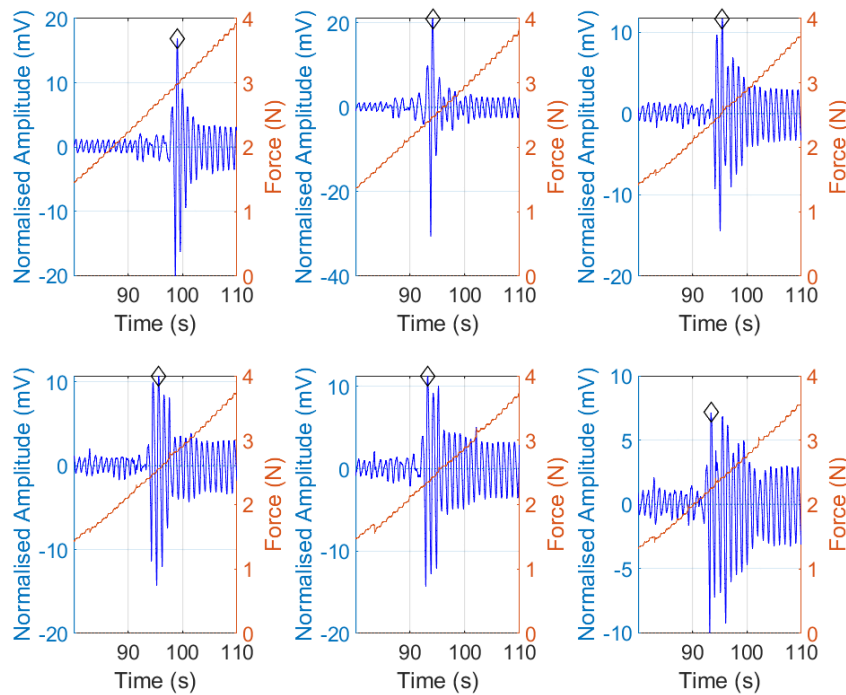


Figure 66 Iteration Plots for Hypotensive Flow Experiment. Each graph in this series of six shows one iteration of the experiment under hypotensive conditions undergoing applied pressure, with the PPG signal in blue and load cell data in orange. TMAX 1 is indicated on each plot and the corresponding force is recorded.

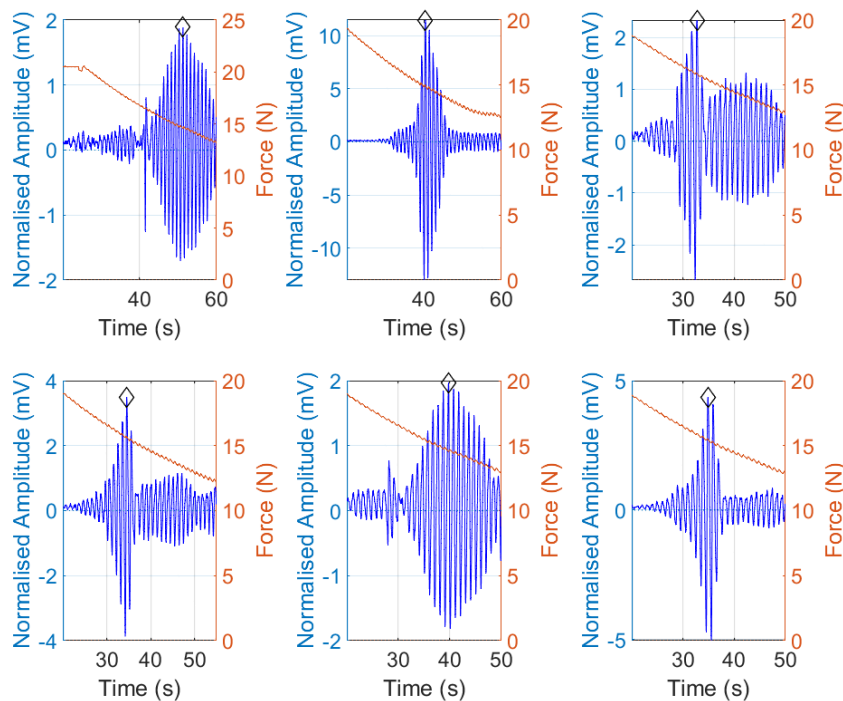


Figure 67 Iteration Plots for Hypotensive Flow Experiment. Each graph in this series of six shows one iteration of the experiment under hypotensive conditions undergoing released pressure, with the PPG signal in blue and load cell data in orange. TMAX 2 is indicated on each plot and the corresponding force is recorded.

Table 8 presents a comprehensive summary of the averaged peak points (TMAX1) from the experiments across all blood pressure states, ranging from hypotension to stage 2 hypertension. The data were analysed and averaged to provide a clear overview of the PPG signal response under varying arterial pressures.

Table 8 The mean force values for TMAX 1 and TMAX 2.

	BLOOD PRESSURE (SBP/DBP) (MMHG)					
	77/53	92/63	110/76	130/91	152/110	175/130
	<u>TMAX1</u>					
MEAN (N)	2.75	2.13	1.85	1.63	1.67	1.55
STD (N)	0.31	0.21	0.08	0.12	0.10	0.11
MEDIAN (N)	2.8	2.14	1.83	1.65	1.65	1.56
	<u>TMAX 2</u>					
MEAN (N)	15.60	13.83	13.54	12.87	12.77	12.56
STD (N)	0.68	0.49	0.23	0.26	0.19	0.14
MEDIAN (N)	15.51	13.76	13.45	12.99	12.77	12.55

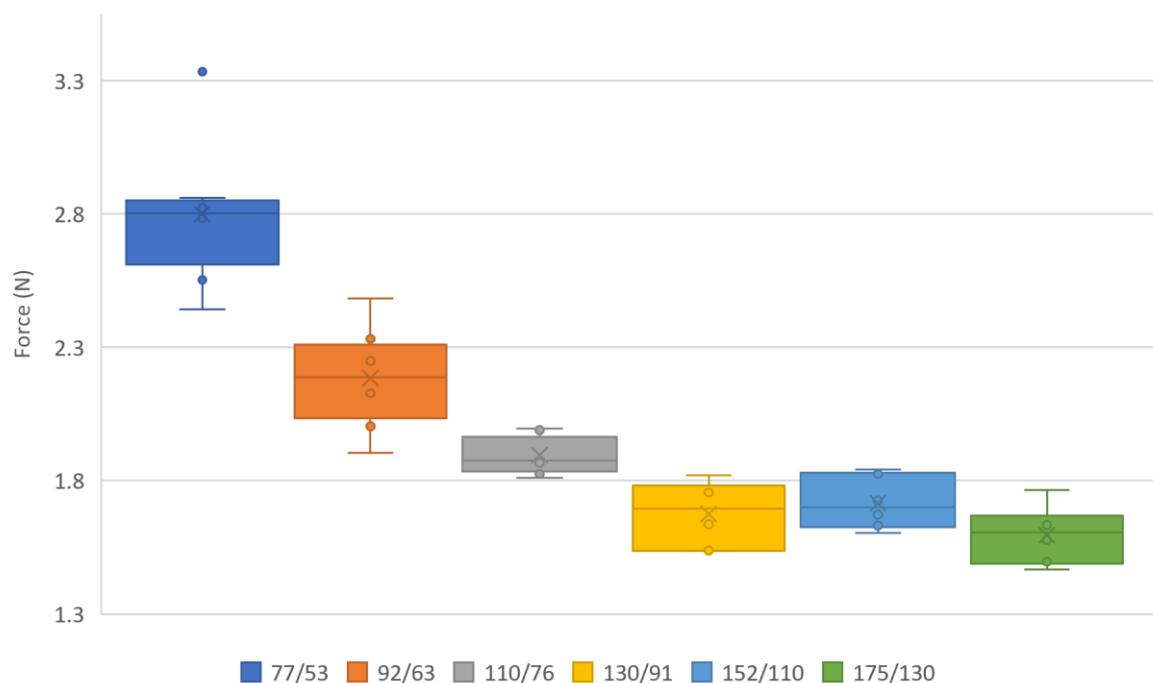


Figure 68 The force at TMAX 1 for each blood pressure level.

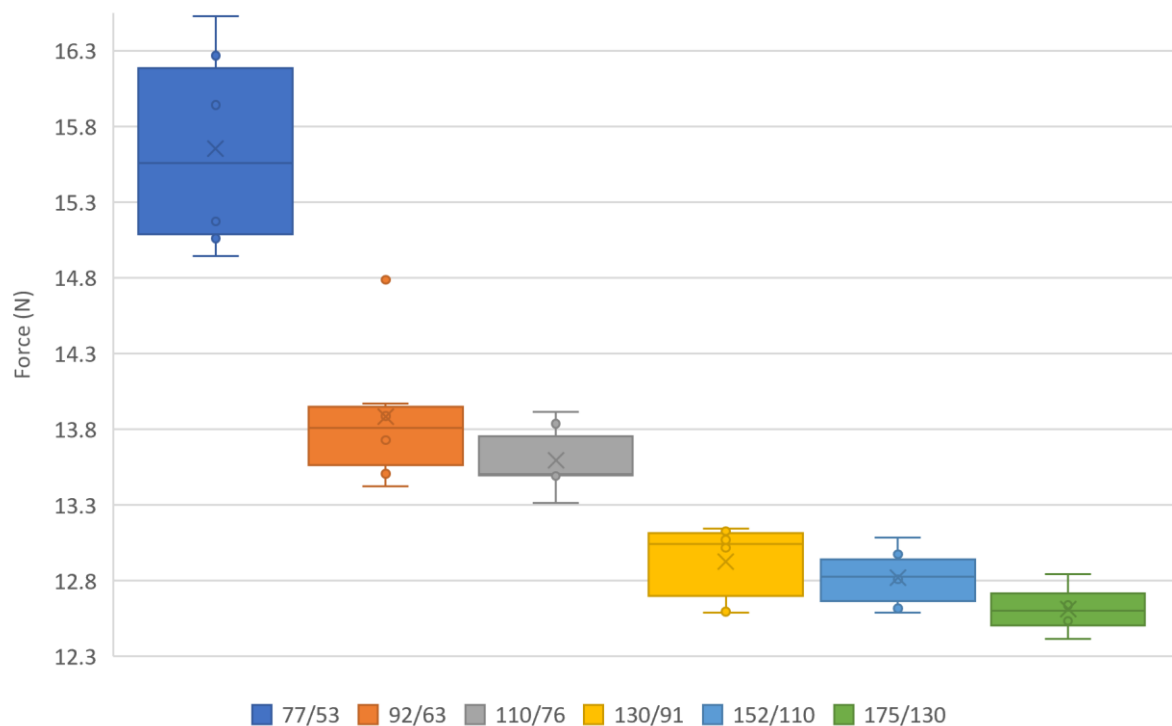


Figure 69 The force at TMAX2 for each blood pressure level.

Figure 68 illustrates the averaged force values at TMAX1 across different blood pressure levels. An observable negative trend is evident, suggesting that the oscillometric peak is influenced by blood pressure, and this effect is detectable in the PPG signal response. Similarly, Figure 69 shows this trend for TMAX2 data, reinforcing the observation. These results signify the potential of using non-invasive blood pressure measurement in wearable technology. Incorporating a simple force sensor in devices like smartphones or smartwatches could enable users to replicate our experimental protocol, leading to more accurate, potentially calibration-free blood pressure measurements. Although preliminary, our findings lay the groundwork for future research, including the development of datasets for machine learning algorithms. This trend observed in our results not only validates our phantom model but also underscores the significance of the advancements made in phantom research throughout this thesis.

Summary

This chapter examines the impact of contact pressure on photoplethysmography (PPG) signal amplitude across different blood pressure levels, from hypotension to stage 2 hypertension. The primary aim of the chapter was to explore how varying degrees of arterial compression affect PPG signals, thereby exploring the implication of PPG in blood pressure measurements. The methodology involved simulating various blood pressure states within a phantom and analysing PPG signal changes at key points during the application and release of force.

The results reveal a notable negative trend in force values at these peak points, suggesting a relationship between oscillometric peaks and blood pressure within the PPG signal response. This trend is evident across all the simulated blood pressure states, indicating the potential of PPG in non-invasive blood pressure measurement in wearable technology. The chapter emphasizes the significance of these findings in validating the phantom model and contributing to the advancement of phantom research, with implications for developing more accurate blood pressure measurement techniques than current cuffless technology and training machine learning algorithms in wearable devices.

10

Discussion

The exploration of novel pulsatile phantoms in photoplethysmography (PPG) undertaken in this research has not only achieved its primary objectives but has also opened up new avenues in the field of biomedical engineering and sensor technology. This chapter aims to critically analyse these achievements, considering their broader implications and potential future research directions.

Methodological Innovation in Phantom Design

The development of vessel-tissue phantoms using a continuous dip-coating method represents a significant methodological innovation in the realm of photoplethysmography research. Achieving a median wall thickness of just 60 μm through this method required meticulous experimentation and optimization, thereby setting a new standard in phantom design. This advancement is particularly noteworthy considering the rarity of phantoms that can simulate human blood pressure dynamics with such precision, especially due to construction constraints in smaller vessels. Traditionally, smaller vessels have been created using lithography and etching techniques in harder resins, silicones or glass[144]. However, these materials often fail to accurately reflect the mechanical properties of real vascular tissues. By contrast, the development work undertaken in this research represents a significant step towards creating more accurate phantoms, capable of mimicking vessels at smaller sizes with greater fidelity. This progress not only demonstrates the potential for achieving a delicate balance between mechanical accuracy and practical usability in phantom development but also paves the way for more realistic and clinically relevant PPG simulations.

Deeper Insights from The Emitter Detector Separation Study

The separation study's findings on emitter-detector distances have initiated an important dialogue about the fundamental principles of PPG sensor design. This study extends beyond contributing to the existing body of knowledge, posing new questions regarding the optimization of sensor placement in wearable devices. The results indicate a need for potential re-evaluation of sensor design strategies, emphasizing improvements in both comfort and accuracy for wearable PPG devices. Notably, the system developed during this study has proven to be an efficient and effective tool for research, facilitating a more nuanced understanding of these factors. This efficiency underscores the study's practical value in guiding future sensor development. Further research might explore the interplay between light penetration depth, skin type, and signal quality, aiming to develop more personalized and efficient wearable PPG sensors. The integration of such findings could significantly enhance the user experience and reliability of these devices, marking a substantial advancement in the field of wearable health monitoring.

Haemodynamic Properties and Cardiovascular Dynamics

The application of the developed vessel-tissue phantoms for simulating different blood pressure states has been instrumental in providing valuable insights into cardiovascular dynamics, a key aspect of this research. This application highlights the complexities involved in accurately replicating human physiological conditions within a controlled environment. By adjusting parameters such as fluid viscosity, flow rate, and vessel compliance within the phantoms, the study was able to mimic various blood pressure scenarios, from normotensive to hypertensive states. The observed changes in PPG signal morphology in response to these varying conditions underscore the intricate relationship between cardiovascular dynamics and PPG signal characteristics.

Particularly noteworthy is how these simulations have enhanced our understanding of the PPG signal's sensitivity to both macroscopic and microscopic changes in blood flow and pressure. For instance, subtle variations in pulse wave velocity and arterial distensibility, induced by different simulated blood pressure states, led to distinct changes in the PPG waveform, including its amplitude and contour. These observations are crucial in

understanding the biophysical mechanisms underpinning PPG readings and their potential variances in clinical situations.

The findings from this research suggest a potential for using PPG not only as a tool for basic heart rate and oxygen saturation measurements but also as a more comprehensive diagnostic method capable of assessing vascular health and blood flow dynamics. This opens exciting possibilities for the future, where PPG could be employed in early detection and monitoring of conditions such as arterial stiffness, peripheral artery disease, and even in assessing the efficacy of antihypertensive treatments.

Arterial Compression Study and Non-Invasive Monitoring

The arterial compression study presented in this thesis offers significant insights into the relationship between mechanical compression and photoplethysmography (PPG) signal response, with far-reaching implications for non-invasive blood pressure monitoring. This study effectively bridges the gap between theoretical research and practical application, setting the stage for innovative uses of PPG in routine health monitoring.

A key achievement of this research has been the development of advanced phantoms capable of accurately mimicking human arterial properties under varying degrees of compression. These phantoms, developed through meticulous methods including the continuous dip-coating technique, have enabled a more precise simulation of arterial behaviour under external pressure. The study's findings reveal that changes in PPG signal amplitude and morphology correlate significantly with the degree of arterial compression, offering a new perspective on assessing vascular health and blood pressure non-invasively.

This correlation is pivotal in understanding the mechanics of blood flow and pressure changes within the vascular system and how they can be effectively captured through PPG technology. The phantoms developed have proven to be exceptional tools in this regard, allowing for controlled experimentation that closely replicates physiological conditions. The ability to simulate a range of blood pressure states, from normal to hypertensive conditions, under

varying degrees of compression provides invaluable data for the development of new PPG-based devices.

The scientific analysis conducted in this study lays the groundwork for the next generation of non-invasive blood pressure monitoring devices. The implications of these advancements are profound. They promise not only to transform how blood pressure is measured in both clinical and non-clinical settings but also to enhance patient comfort and compliance. The integration of these findings and machine learning together into the design and development of advanced, non-invasive blood pressure monitoring devices could mark a significant leap forward in cardiovascular health monitoring.

Future Research Directions

The substantial findings of this research not only contribute significantly to the field of photoplethysmography (PPG) but also illuminate several promising avenues for future exploration. These avenues span from the enhancement of phantom design to the application of advanced technologies in cardiovascular health assessment.

Building upon the significant achievements in phantom development presented in this study, future research should embark on exploring alternative materials and coating processes. This exploration is critical to further enhance the realism and applicability of these phantoms across a range of biomedical research scenarios. One key area of this exploration involves the addition of optical characteristics that mimic multiple layers of tissue, thereby providing a more accurate representation of human physiological conditions. It would be vital to measure the scattering coefficient of the materials used to ensure it is realistic.

In addition to improving the mechanical properties and the simulation of tissue layers, a crucial advancement would be the reduction of vessel sizes to approach microvascular levels. The development of phantoms that can accurately replicate the complexities of the microvasculature will be a groundbreaking step forward. This level of detail is essential for simulating and studying a wide array of cardiovascular and microcirculatory conditions, and

it would significantly enhance the fidelity of simulations in both academic and clinical research.

The incorporation of these advanced features – improved optical characteristics, finer vessel structures, and enhanced material properties – will not only benefit academic research but also have substantial implications for clinical applications. These advancements could lead to better diagnostic tools, more effective treatment strategies, and a deeper understanding of various cardiovascular diseases.

Future studies should aim to expand the scope of research to include a wider array of cardiovascular conditions, such as arrhythmic events and arterial stiffness. The inclusion of these conditions would not only broaden the applicability of the phantoms but also contribute to a more comprehensive understanding of cardiovascular health and disease. The integration of advanced computational modelling and machine learning with these simulations could further enhance the predictive accuracy and diagnostic value of PPG technology.

In summary, the research presented in this thesis not only achieves its set objectives but also paves the way for future advancements in the field of PPG and wearable health monitoring. The methodologies developed and findings obtained offer a foundation upon which future research can build, potentially leading to significant improvements in non-invasive cardiovascular monitoring and patient care.

11

Conclusion

Here we reflect on the comprehensive journey undertaken to achieve the objectives set out at the outset. The primary goal was to significantly advance photoplethysmography (PPG) technology through the development of novel pulsatile phantoms, and to rigorously explore their application in simulating various cardiovascular conditions. This aim has been meticulously realized through the chapters of the thesis, each contributing to a deeper understanding and enhancement of PPG technology.

The initial chapters laid the foundation by developing geometrically and mechanically accurate vessel-tissue phantoms. This achievement, facilitated by a novel continuous dip-coating method, marked a significant leap in the field of PPG. It resulted in the creation of custom-made vessels with a median wall thickness of just 60 μm , offering a more realistic simulation of human vascular structures compared to commercially available options. This breakthrough in phantom design has been crucial in improving the fidelity of PPG signals, thereby enabling more accurate simulations of physiological conditions.

The separation study further explored the impact of emitter-detector distance on PPG signal characteristics, revealing that optimal PPG detection occurs at shallower depths. This finding is instrumental in understanding the fundamental mechanics of PPG and sets a new standard of sensors for future research in the field.

The investigation into haemodynamic properties utilized the developed phantoms to simulate different blood pressure states. This study was pivotal in demonstrating how altering resistance elements could replicate various blood pressure conditions, leading to observable changes in PPG signal morphology. The findings from this study provided critical insights

into the impact of blood pressure variations on PPG signal characteristics, enhancing our understanding of cardiovascular dynamics.

The arterial compression study delved into the effect of varying degrees of compression on PPG signal amplitudes across different blood pressure levels. The clear relationship between applied force and PPG signal oscillometric response highlighted the potential of PPG in non-invasive blood pressure measurement, a significant stride towards practical applications in health monitoring.

The collective outcomes from these studies have directly addressed the thesis's objectives. The development of custom-made phantoms and the insights from the separation study have advanced PPG technology, particularly in terms of signal analysis accuracy. The arterial compression and haemodynamic properties studies have validated the utility of these phantoms in simulating cardiovascular conditions, revealing complex interactions within the cardiovascular system.

Moreover, these findings carry significant implications for the future of non-invasive cardiovascular assessment, especially in the context of wearable technology. The potential for PPG to be utilized in wearable devices for more accurate and user-friendly blood pressure monitoring is a testament to the success of this research. The progression from the development of novel phantoms to their application in simulating and understanding complex cardiovascular phenomena demonstrates how innovative phantom design can enhance the accuracy and reliability of PPG technology. The insights gained from this research not only advance our understanding of cardiovascular health and disease but also open new avenues for applying PPG technology in modern healthcare settings.

References

- [1] J. Allen, 'Photoplethysmography and its application in clinical physiological measurement.', *Physiol Meas*, vol. 28, no. 3, pp. R1–R39, 2007, doi: 10.1088/0967-3334/28/3/R01.
- [2] I. Fine, 'The optical origin of the PPG signal', E. A. Genina, V. L. Derbov, I. Meglinski, and V. V. Tuchin, Eds., International Society for Optics and Photonics, Jan. 2014, p. 903103. doi: 10.1117/12.2051228.
- [3] A. Herzman and C. Spealman, 'Observations of the finger volume pulse recorded photo-electrically.', *American Journal of Physiology*, vol. 119, pp. 334–335, 1937.
- [4] T. Aoyagi, 'Pulse oximetry: its invention, theory, and future', *J Anesth*, vol. 17, no. 4, pp. 259–266, Nov. 2003, doi: 10.1007/s00540-003-0192-6.
- [5] T. Tamura, Y. Maeda, M. Sekine, and M. Yoshida, 'Wearable Photoplethysmographic Sensors—Past and Present', *Electronics (Basel)*, vol. 3, no. 2, pp. 282–302, 2014, doi: 10.3390/electronics3020282.
- [6] H. H. Asada, P. Shaltis, A. Reisner, S. Rhee, and R. C. Hutchinson, 'Mobile Monitoring with Wearable Photoplethysmographic Biosensors', *IEEE Engineering in Medicine and Biology Magazine*, 2003, doi: 10.1109/MEMB.2003.1213624.
- [7] M. Ghamari, 'A review on wearable photoplethysmography sensors and their potential future applications in health care', *Int J Biosens Bioelectron*, vol. 4, no. 4, 2018, doi: 10.15406/ijbsbe.2018.04.00125.
- [8] M. Hosanee *et al.*, 'Cuffless single-site photoplethysmography for blood pressure monitoring', *Journal of Clinical Medicine*, vol. 9, no. 3. 2020. doi: 10.3390/jcm9030723.
- [9] G. J. Tortora and B. Derrickson, *Principles of Anatomy & Physiology 14th Edition*. 2014. doi: 10.1017/CBO9781107415324.004.
- [10] X. Xing and M. Sun, 'Optical blood pressure estimation with photoplethysmography and FFT-based neural networks', *Biomed Opt Express*, vol. 7, no. 8, 2016, doi: 10.1364/boe.7.003007.
- [11] J. F. Stover *et al.*, 'Noninvasive cardiac output and blood pressure monitoring cannot replace an invasive monitoring system in critically ill patients', *BMC Anesthesiol*, vol. 9, 2009, doi: 10.1186/1471-2253-9-6.

-
- [12] B. Saugel, K. Kouz, A. S. Meidert, L. Schulte-Uentrop, and S. Romagnoli, 'How to measure blood pressure using an arterial catheter: A systematic 5-step approach', *Critical Care*, vol. 24, no. 1. 2020. doi: 10.1186/s13054-020-02859-w.
- [13] B. Saugel, F. Fassio, A. Hapfelmeier, A. S. Meidert, R. M. Schmid, and W. Huber, 'The T-Line TL-200 system for continuous non-invasive blood pressure measurement in medical intensive care unit patients', *Intensive Care Med*, vol. 38, no. 9, 2012, doi: 10.1007/s00134-012-2617-x.
- [14] M. Di Biase, A. Casani, and L. Orfeo, 'Invasive arterial blood pressure in the neonatal intensive care: a valuable tool to manage very ill preterm and term neonates', *Ital J Pediatr*, vol. 41, no. S1, 2015, doi: 10.1186/1824-7288-41-s1-a9.
- [15] D. Perloff *et al.*, 'Human blood pressure: Determination by sphygmomanometry', *Circulation*, vol. 88, no. 5 I, 1993, doi: 10.1161/01.CIR.88.5.2460.
- [16] G. Drzewiecki, R. Hood, and H. Apple, 'Theory of the oscillometric maximum and the systolic and diastolic detection ratios', *Ann Biomed Eng*, vol. 22, no. 1, 1994, doi: 10.1007/BF02368225.
- [17] A. Chandrasekhar, C. S. Kim, M. Naji, K. Natarajan, J. O. Hahn, and R. Mukkamala, 'Smartphone-based blood pressure monitoring via the oscillometric finger-pressing method', *Sci Transl Med*, vol. 10, no. 431, 2018, doi: 10.1126/scitranslmed.aap8674.
- [18] A. Chandrasekhar, K. Natarajan, M. Yavarimanesh, and R. Mukkamala, 'An iPhone Application for Blood Pressure Monitoring via the Oscillometric Finger Pressing Method', *Sci Rep*, vol. 8, no. 1, 2018, doi: 10.1038/s41598-018-31632-x.
- [19] G. Fortino and V. Giampà, 'PPG-based methods for non invasive and continuous blood pressure measurement: an overview and development issues in body sensor networks', *Medical Measurements and Applications Proceedings (MeMeA), 2010 IEEE International Workshop on*, pp. 1–4, 2010, doi: 10.1109/MEMEA.2010.5480201.
- [20] M. Elgendi *et al.*, 'The use of photoplethysmography for assessing hypertension', *NPJ Digit Med*, vol. 2, no. 1, 2019, doi: 10.1038/s41746-019-0136-7.
- [21] J. Liu, B. P.-Y. Yan, W.-X. Dai, X.-R. Ding, Y.-T. Zhang, and N. Zhao, 'Multi-wavelength photoplethysmography method for skin arterial pulse extraction', *Biomed Opt Express*, vol. 7, no. 10, p. 4313, 2016, doi: 10.1364/BOE.7.004313.

-
- [22] C. I. Nwafor *et al.*, 'Assessment of a noninvasive optical photoplethysmography imaging device with dynamic tissue phantom models', *J Biomed Opt*, 2017, doi: 10.1117/1.jbo.22.9.096003.
- [23] N. Stuban, M. Niwayama, and H. Santha, 'Phantom with Pulsatile Arteries to Investigate the Influence of Blood Vessel Depth on Pulse Oximeter Signal Strength', *Sensors*, vol. 12, pp. 895–904, 2012, doi: 10.3390/s120100895.
- [24] M. Nomoni, J. M. May, and P. A. Kyriacou, 'Fabricating Novel PDMS Vessels for Phantoms in Photoplethysmography Investigations', in *2020 42nd Annual International Conference of the IEEE Engineering in Medicine & Biology Society (EMBC)*, 2020, p. Accepted.
- [25] G. Derrickson, B. Tortora, *Principles of Anatomy and Physiology 13th ed.* 2012. doi: 10.1007/s13398-014-0173-7.2.
- [26] E. N. Marieb and S. M. Keller, *Essentials of Human Anatomy & Physiology plus Pearson Mastering Anatomy & Physiology with Pearson eText, Global Edition.* 2017.
- [27] B. T. G Derrickson, *Principles of Anatomy and Physiology 13th ed.* 2012. doi: 10.1007/s13398-014-0173-7.2.
- [28] E. N. Marieb, P. B. Wilhelm, and J. Mallatt, 'Human Anatomy', *Pearson*, no. July, p. 784, 2014, doi: 10.1016/j.mrgentox.2012.03.010.
- [29] M. B. Wayson *et al.*, 'Suggested reference values for regional blood volumes in children and adolescents', *Phys Med Biol*, vol. 63, no. 15, p. 155022, Aug. 2018, doi: 10.1088/1361-6560/aad313.
- [30] R. J. Solaro, 'Regulation of Cardiac Contractility', *Colloquium Series on Integrated Systems Physiology: From Molecule to Function*, vol. 3, no. 3, 2011, doi: 10.4199/c00030ed1v01y201104isp018.
- [31] J. Mayet and A. Hughes, 'Cardiac and vascular pathophysiology in hypertension', *Heart*, vol. 89, no. 9. 2003. doi: 10.1136/heart.89.9.1104.
- [32] R. E. Klabunde, 'Cardiovascular Physiology Concepts', *Lippincott Williams & Wilkins*, 2004, doi: citeulike-article-id:2086320.
- [33] M. H. C. Pham *et al.*, 'Normal values of aortic dimensions assessed by multidetector computed tomography in the Copenhagen General Population Study', *Eur Heart J Cardiovasc Imaging*, vol. 20, no. 8, pp. 939–948, Aug. 2019, doi: 10.1093/ehjci/jez012.

-
- [34] *Biomechanics of Living Organs*. Elsevier, 2017. doi: 10.1016/c2015-0-00832-2.
- [35] C. Y. Liu *et al.*, 'Evolution of aortic wall thickness and stiffness with atherosclerosis: Long-term follow up from the multi-ethnic study of atherosclerosis', *Hypertension*, vol. 65, no. 5, pp. 1015–1019, May 2015, doi: 10.1161/HYPERTENSIONAHA.114.05080.
- [36] A. M. Manole, D. M. Iliescu, A. Rusali, and P. Bordei, 'Morphometry of the aortic arch and its branches', *ARS Medica Tomitana*, vol. 19, no. 3, pp. 154–159, Oct. 2013, doi: 10.2478/arism-2013-0027.
- [37] M. M. Kupari, M. S. Pamilo, R. I. Pajari, V.-P. Poutanen, P. E. Hekali, and R. Raninen, 'Arterial wall thickness measurements by B mode ultrasonography in patients with Takayasu's arteritis Reino', *Ann Rheum Dis*, vol. 55, pp. 461–465, 1996, doi: 10.1136/ard.55.7.461.
- [38] Y. Iwamoto *et al.*, 'Intima-media thickness of brachial artery, vascular function, and cardiovascular risk factors', *Arterioscler Thromb Vasc Biol*, vol. 32, no. 9, pp. 2295–2303, Sep. 2012, doi: 10.1161/ATVBAHA.112.249680.
- [39] D. Getachew, A. Astatkie, and K. Lemma, 'Diameter, Vessel Thickness and Angle of Bifurcation of the Radial Artery in Ethiopian Cadavers', *J Morphol Sci*, vol. 35, pp. 129–135, 2018, doi: 10.1055/s-0038-1669905.
- [40] V. P. S. Fazan, C. T. Borges, J. H. da Silva, A. G. Caetano, and O. A. R. Filho, 'Superficial palmar arch: An arterial diameter study', *J Anat*, vol. 204, no. 4, pp. 307–311, Apr. 2004, doi: 10.1111/j.0021-8782.2004.00281.x.
- [41] A. N. Pruzan, A. E. Kaufman, C. Calcagno, Y. Zhou, Z. A. Fayad, and V. Mani, 'Feasibility of imaging superficial palmar arch using micro-ultrasound, 7T and 3T magnetic resonance imaging.', *World J Radiol*, vol. 9, no. 2, pp. 79–84, Feb. 2017, doi: 10.4329/wjr.v9.i2.79.
- [42] B. M. Leslie, L. K. Ruby, S. J. Madell, and F. Wittenstein, 'Digital artery diameters: an anatomic and clinical study.', *J Hand Surg Am*, vol. 12, no. 5 Pt 1, pp. 740–3, Sep. 1987, doi: 10.1016/s0363-5023(87)80060-6.
- [43] D. Lakshmipathy, 'Human anatomy and physiology', in *Biomedical Engineering and its Applications in Healthcare*, 2019. doi: 10.1007/978-981-13-3705-5_1.
- [44] J. R. Levick and J. R. Levick, 'Chapter 10 – Vascular smooth muscle', in *An Introduction to Cardiovascular Physiology*, 1991. doi: 10.1016/B978-0-7506-1028-5.50013-5.

-
- [45] J. R. Levick and J. R. Levick, 'Chapter 10 – Vascular smooth muscle', in *An Introduction to Cardiovascular Physiology*, 1991. doi: 10.1016/B978-0-7506-1028-5.50013-5.
- [46] J. E. Hungerford, G. K. Owens, W. S. Argraves, and C. D. Little, 'Development of the aortic vessel wall as defined by vascular smooth muscle and extracellular matrix markers.', *Dev Biol*, vol. 178, no. 2, pp. 375–392, 1996, doi: 10.1006/dbio.1996.0225.
- [47] P. Salvi, *Pulse Waves*. 2012. doi: 10.1007/978-88-470-2439-7.
- [48] P. Salvi, *Pulse Waves*. 2012. doi: 10.1007/978-88-470-2439-7.
- [49] R. Fogliardi, M. Di Donfrancesco, and R. Burattini, 'Comparison of linear and nonlinear formulations of the three-element windkessel model', *Am J Physiol Heart Circ Physiol*, vol. 271, no. 6 40-6, 1996, doi: 10.1152/ajpheart.1996.271.6.h2661.
- [50] M. Olufsen and A. Nadim, 'On deriving lumped models for blood flow and pressure in the systemic arteries', *Mathematical Biosciences and Engineering*, vol. 1, no. 1, 2004, doi: 10.3934/mbe.2004.1.61.
- [51] D. N. Ku, 'BLOOD FLOW IN ARTERIES', *Annu Rev Fluid Mech*, 1997, doi: 10.1146/annurev.fluid.29.1.399.
- [52] J. G. Webster, 'Measurement of flow and volume of blood', *Medical Instrumentation Application and Design*, 2008, doi: 10.1016/j.mpaic.2011.12.013.
- [53] W. B. Carpenter and H. Power, 'Principles of Human Physiology', *J Cell Sci*, vol. S2-4, no. 16, 1864, doi: 10.1242/jcs.s2-4.16.282.
- [54] Z. S. Bruss and A. Raja, *Physiology, Stroke Volume*. 2019.
- [55] R. H. G. Schwinger, 'Pathophysiology of heart failure', *Cardiovascular Diagnosis and Therapy*, vol. 11, no. 1. 2021. doi: 10.21037/CDT-20-302.
- [56] C. Saxelby, 'Cardiovascular Disease: Diet, Nutrition and Emerging Risk Factors', *Nutrition & Dietetics*, vol. 63, no. 3, 2006, doi: 10.1111/j.1747-0080.2006.00084.x.
- [57] M. A. Creager, J. A. Beckman, and J. Loscalzo, *Vascular Medicine: A Companion to Braunwald's Heart Disease: Second Edition*. 2012. doi: 10.1016/C2009-0-63388-2.
- [58] P. M. Kearney, M. Whelton, K. Reynolds, P. Muntner, P. K. Whelton, and J. He, 'Global burden of hypertension: Analysis of worldwide data', *Lancet*, vol. 365, no. 9455, 2005, doi: 10.1016/S0140-6736(05)70151-3.

-
- [59] J. Mayet and A. Hughes, 'Cardiac and vascular pathophysiology in hypertension', *Heart*, vol. 89, no. 9. 2003. doi: 10.1136/heart.89.9.1104.
- [60] M. Steenman and G. Lande, 'Cardiac aging and heart disease in humans', *Biophysical Reviews*, vol. 9, no. 2. 2017. doi: 10.1007/s12551-017-0255-9.
- [61] S. Saheera and P. Krishnamurthy, 'Cardiovascular Changes Associated with Hypertensive Heart Disease and Aging', *Cell Transplantation*, vol. 29. 2020. doi: 10.1177/0963689720920830.
- [62] T. Sidiropoulou, M. Tsoumpa, P. Griva, V. Galarioti, and P. Matsota, 'Prediction and Prevention of Intraoperative Hypotension with the Hypotension Prediction Index: A Narrative Review', *Journal of Clinical Medicine*, vol. 11, no. 19. 2022. doi: 10.3390/jcm11195551.
- [63] F. Guarracino and P. Bertini, 'Perioperative hypotension: causes and remedies', *Journal of Anesthesia, Analgesia and Critical Care*, vol. 2, no. 1, 2022, doi: 10.1186/s44158-022-00045-8.
- [64] M. Dani *et al.*, 'Orthostatic hypotension in older people: Considerations, diagnosis and management', *Clinical Medicine, Journal of the Royal College of Physicians of London*, vol. 21, no. 3. 2021. doi: 10.7861/CLINMED.2020-1044.
- [65] Vertex42, 'Blood Pressure Chart'. Accessed: Nov. 20, 2023. [Online]. Available: <https://www.vertex42.com/ExcelTemplates/blood-pressure-chart.html>
- [66] Medicine & Healthcare Products Regulatory Agency, 'Blood Pressure Measurement Devices', *Medicine and Healthcare Products Regulatory Agency*, vol. 2, no. 1, 2021.
- [67] E. O'Brien *et al.*, 'European Society of Hypertension recommendations for conventional, ambulatory and home blood pressure measurement', *Journal of Hypertension*, vol. 21, no. 5. 2003. doi: 10.1097/00004872-200305000-00001.
- [68] OMRON UK, 'Automatic Sphygmomanometer OMRON'. Accessed: Nov. 20, 2023. [Online]. Available: <https://www.omron-healthcare.co.uk/products/m2>
- [69] C. K. Bradley *et al.*, 'Cuffless Blood Pressure Devices', *Am J Hypertens*, vol. 35, no. 5, 2022, doi: 10.1093/ajh/hpac017.
- [70] J. Allen, 'Photoplethysmography and its application in clinical physiological measurement.', *Physiol Meas*, vol. 28, no. 3, pp. R1–R39, 2007, doi: 10.1088/0967-3334/28/3/R01.

-
- [71] J. Allen, D. Zheng, P. A. Kyriacou, and M. Elgendi, 'Photoplethysmography (PPG): state-of-the-art methods and applications', *Physiological Measurement*, vol. 42, no. 10, 2021. doi: 10.1088/1361-6579/ac2d82.
- [72] A. Zuhair Sameen, R. Jaafar, E. Zahedi, and G. Kok Beng, 'Cuff-less and continuous blood pressure measurement based on pulse transit time from carotid and toe photoplethysmograms', *J Med Eng Technol*, vol. 46, no. 7, 2022, doi: 10.1080/03091902.2022.2077998.
- [73] R. C. Block *et al.*, 'Conventional pulse transit times as markers of blood pressure changes in humans', *Sci Rep*, vol. 10, no. 1, 2020, doi: 10.1038/s41598-020-73143-8.
- [74] D. B. McCombie, A. T. Reisner, and H. H. Asada, 'Adaptive blood pressure estimation from wearable PPG sensors using peripheral artery pulse wave velocity measurements and multi-channel blind identification of local arterial dynamics', *Annual International Conference of the IEEE Engineering in Medicine and Biology - Proceedings*, pp. 3521–3524, 2006, doi: 10.1109/IEMBS.2006.260590.
- [75] S. G. Khalid, J. Zhang, F. Chen, and D. Zheng, 'Blood Pressure Estimation Using Photoplethysmography Only: Comparison between Different Machine Learning Approaches', *J Healthc Eng*, vol. 2018, 2018, doi: 10.1155/2018/1548647.
- [76] M. H. Chowdhury *et al.*, 'Estimating blood pressure from the photoplethysmogram signal and demographic features using machine learning techniques', *Sensors (Switzerland)*, vol. 20, no. 11, 2020, doi: 10.3390/s20113127.
- [77] T. Sadad, S. A. C. Bukhari, A. Munir, A. Ghani, A. M. El-Sherbeeney, and H. T. Rauf, 'Detection of Cardiovascular Disease Based on PPG Signals Using Machine Learning with Cloud Computing', *Comput Intell Neurosci*, vol. 2022, 2022, doi: 10.1155/2022/1672677.
- [78] P. C. P. Chao, C. C. Wu, D. H. Nguyen, B. S. Nguyen, P. C. Huang, and V. H. Le, 'The Machine Learnings Leading the Cuffless PPG Blood Pressure Sensors into the Next Stage', *IEEE Sens J*, vol. 21, no. 11, 2021, doi: 10.1109/JSEN.2021.3073850.
- [79] J. Allen and P. Kyriacou, *Photoplethysmography: Technology, Signal Analysis and Applications*. 2021. doi: 10.1016/C2020-0-00098-8.
- [80] P. H. Charlton *et al.*, 'The 2023 wearable photoplethysmography roadmap', *Physiol Meas*, 2023, doi: 10.1088/1361-6579/acead2.

-
- [81] K. Welykholowa *et al.*, 'Multimodal photoplethysmography-based approaches for improved detection of hypertension', *Journal of Clinical Medicine*, vol. 9, no. 4. 2020. doi: 10.3390/jcm9041203.
- [82] S. Knight *et al.*, 'The Accuracy of Wearable Photoplethysmography Sensors for Telehealth Monitoring: A Scoping Review', *Telemedicine and e-Health*, vol. 29, no. 6, 2023, doi: 10.1089/tmj.2022.0182.
- [83] M. Namvari *et al.*, 'Photoplethysmography Enabled Wearable Devices and Stress Detection: A Scoping Review', *Journal of Personalized Medicine*, vol. 12, no. 11. 2022. doi: 10.3390/jpm12111792.
- [84] P. D. Mannheim, 'The Light-Tissue Interaction of Pulse Oximetry', *Anesth Analg*, vol. 105, no. On Line Suppl., pp. S10-S17, Nov. 2007, doi: 10.1213/01.ane.0000269522.84942.54.
- [85] D. T. Delpy, M. Cope, P. van der Zee, S. Arridge, S. Wray, and J. Wyatt, 'Estimation of optical pathlength through tissue from direct time of flight measurement.', *Phys Med Biol*, vol. 33, no. 12, pp. 1433-1442, 1988, doi: 10.1088/0031-9155/33/12/008.
- [86] V. V. Tuchin, 'Tissue Optics and Photonics: Light-Tissue Interaction', *J Biomed Photonics Eng*, 2015, doi: 10.18287/jbpe-2015-1-2-98.
- [87] K. Lüders and R. O. Pohl, 'The Relation Between Absorption, Reflection and Refraction of Light', in *Pohl's Introduction to Physics*, 2018. doi: 10.1007/978-3-319-50269-4_25.
- [88] J. D. Enderle and J. D. Bronzino, *Introduction to Biomedical Engineering*. 2011. doi: 10.1016/C2009-0-19716-7.
- [89] V. V. Tuchin, *Tissue optics: Light scattering methods and instruments for medical diagnosis: Third edition*. 2015. doi: 10.1117/3.1003040.
- [90] I. Fine, 'The optical origin of the PPG signal', E. A. Genina, V. L. Derbov, I. Meglinski, and V. V Tuchin, Eds., International Society for Optics and Photonics, Nov. 2014, p. 903103. doi: 10.1117/12.2051228.
- [91] G. J. Tortora and B. Derrickson, *Principles of Anatomy & Physiology 14th Edition*. 2014. doi: 10.1017/CBO9781107415324.004.
- [92] M. Elgendi, 'On the Analysis of Fingertip Photoplethysmogram Signals', *Curr Cardiol Rev*, 2012, doi: 10.2174/157340312801215782.

-
- [93] A. A. Awad *et al.*, 'The relationship between the photoplethysmographic waveform and systemic vascular resistance', *J Clin Monit Comput*, vol. 21, no. 6, 2007, doi: 10.1007/s10877-007-9097-5.
- [94] S. N. Zaidi and S. M. Collins, 'Orthostatic stress and area under the curve of photoplethysmography waveform', *Biomed Phys Eng Express*, vol. 2, no. 4, 2016, doi: 10.1088/2057-1976/2/4/045006.
- [95] L. Wang, E. Pickwell-MacPherson, Y. P. Liang, and Y. T. Zhang, 'Noninvasive cardiac output estimation using a novel photoplethysmogram index', in *Proceedings of the 31st Annual International Conference of the IEEE Engineering in Medicine and Biology Society: Engineering the Future of Biomedicine, EMBC 2009*, 2009. doi: 10.1109/IEMBS.2009.5333091.
- [96] S. Lu *et al.*, 'Can photoplethysmography variability serve as an alternative approach to obtain heart rate variability information?', *J Clin Monit Comput*, vol. 22, no. 1, 2008, doi: 10.1007/s10877-007-9103-y.
- [97] S. C. Millasseau, R. P. Kelly, J. M. Ritter, and P. J. Chowienczyk, 'Determination of age-related increases in large artery stiffness by digital pulse contour analysis', *Clin Sci*, vol. 103, no. 4, 2002, doi: 10.1042/cs1030371.
- [98] A. V. Challoner and C. A. Ramsay, 'A photoelectric plethysmograph for the measurement of cutaneous blood flow.', *Phys Med Biol*, vol. 19, no. 3, pp. 317–328, Nov. 1974, [Online]. Available: <http://www.ncbi.nlm.nih.gov/pubmed/4445210>
- [99] A. A. Kamshilin and N. B. Margaryants, 'Origin of Photoplethysmographic Waveform at Green Light', *Phys Procedia*, vol. 86, no. June 2015, pp. 72–80, 2017, doi: 10.1016/j.phpro.2017.01.024.
- [100] I. S. Sidorov, R. V. Romashko, V. T. Koval, R. Giniatullin, and A. A. Kamshilin, 'Origin of infrared light modulation in reflectance-mode photoplethysmography', *PLoS One*, vol. 11, no. 10, pp. 1–11, 2016, doi: 10.1371/journal.pone.0165413.
- [101] S. S. 1 & G. de H. 2 Andreia V. Moço 1, 'New insights into the origin of remote PPG signals in visible light and infrared', [Online]. Available: <file:///C:/Users/Michelle/Desktop/new%20insights%20into%20the%20origin%20of%20remote%20ppg.pdf>

-
- [102] E. D. Chan, M. M. Chan, and M. M. Chan, 'Pulse oximetry: Understanding its basic principles facilitates appreciation of its limitations', *Respiratory Medicine*. 2013. doi: 10.1016/j.rmed.2013.02.004.
- [103] M. Shabaan *et al.*, 'Survey: Smartphone-based assessment of cardiovascular diseases using ECG and PPG analysis', *BMC Medical Informatics and Decision Making*, vol. 20, no. 1. 2020. doi: 10.1186/s12911-020-01199-7.
- [104] R. S. Vulcan, S. André, and M. Bruyneel, 'Photoplethysmography in normal and pathological sleep', *Sensors*, vol. 21, no. 9, 2021, doi: 10.3390/s21092928.
- [105] J. Spigulis, L. Gailite, A. Lihachev, and R. Erts, 'Simultaneous recording of skin blood pulsations at different vascular depths by multiwavelength photoplethysmography.', *Appl Opt*, vol. 46, no. 10, pp. 1754–1759, 2007, doi: 10.1364/AO.46.001754.
- [106] B. Bradke and B. Everman, 'Investigation of photoplethysmography behind the ear for pulse oximetry in hypoxic conditions with a novel device (SPYDR)', *Biosensors (Basel)*, vol. 10, no. 4, 2020, doi: 10.3390/bios10040034.
- [107] J. T. B. Moyle, *Pulse oximetry*. BMJ Publishing Group, 1994.
- [108] P. A. Kyriacou, 'Pulse oximetry in the oesophagus', *Physiol Meas*, 2006, doi: 10.1088/0967-3334/27/1/R01.
- [109] T. Aoyagi, 'Pulse oximetry: Its invention, theory, and future', *J Anesth*, 2003, doi: 10.1007/s00540-003-0192-6.
- [110] R. Lazazzera *et al.*, 'Detection and Classification of Sleep Apnea and Hypopnea Using PPG and SpO2 Signals', *IEEE Trans Biomed Eng*, vol. 68, no. 5, 2021, doi: 10.1109/TBME.2020.3028041.
- [111] A. B. Liu, P. C. Hsu, Z. L. Chen, and H. T. Wu, 'Measuring pulse wave velocity using ECG and photoplethysmography', in *Journal of Medical Systems*, 2011. doi: 10.1007/s10916-010-9469-0.
- [112] L. N. Lyzwinski, M. Elgendi, and C. Menon, 'The Use of Photoplethysmography in the Assessment of Mental Health: Scoping Review', *JMIR Mental Health*, vol. 10. 2023. doi: 10.2196/40163.
- [113] R. Huttunen *et al.*, 'Assessment of obstructive sleep apnea-related sleep fragmentation utilizing deep learning-based sleep staging from photoplethysmography', *Sleep*, vol. 44, no. 10, 2021, doi: 10.1093/sleep/zsab142.

-
- [114] E. Volkova *et al.*, 'Multispectral sensor fusion in SmartWatch for in situ continuous monitoring of human skin hydration and body sweat loss', *Sci Rep*, vol. 13, no. 1, 2023, doi: 10.1038/s41598-023-40339-7.
- [115] P. M. Middleton, C. H. H. Tang, G. S. H. Chan, S. Bishop, A. V. Savkin, and N. H. Lovell, 'Peripheral photoplethysmography variability analysis of sepsis patients', *Med Biol Eng Comput*, vol. 49, no. 3, 2011, doi: 10.1007/s11517-010-0713-z.
- [116] S. Zanelli, M. Ammi, M. Hallab, and M. A. El Yacoubi, 'Diabetes Detection and Management through Photoplethysmographic and Electrocardiographic Signals Analysis: A Systematic Review', *Sensors*, vol. 22, no. 13, 2022. doi: 10.3390/s22134890.
- [117] A. Lanata, 'Wearable Systems for Home Monitoring Healthcare: The Photoplethysmography Success Pros and Cons', *Biosensors*, vol. 12, no. 10, 2022. doi: 10.3390/bios12100861.
- [118] W. Jiang *et al.*, 'A Wearable Tele-Health System towards Monitoring COVID-19 and Chronic Diseases', *IEEE Rev Biomed Eng*, vol. 15, 2022, doi: 10.1109/RBME.2021.3069815.
- [119] C. K. McGarry *et al.*, 'Tissue mimicking materials for imaging and therapy phantoms: A review', *Physics in Medicine and Biology*, vol. 65, no. 23, 2020. doi: 10.1088/1361-6560/abbd17.
- [120] B. W. Pogue and M. S. Patterson, 'Review of tissue simulating phantoms for optical spectroscopy, imaging and dosimetry', *J Biomed Opt*, vol. 11, no. 4, p. 41102, 2006, doi: 10.1117/1.2335429.
- [121] K. E. Keenan *et al.*, 'Quantitative magnetic resonance imaging phantoms: A review and the need for a system phantom', *Magnetic Resonance in Medicine*, vol. 79, no. 1, 2018. doi: 10.1002/mrm.26982.
- [122] N. Stuban, M. Niwayama, and H. Santha, 'Phantom with Pulsatile Arteries to Investigate the Influence of Blood Vessel Depth on Pulse Oximeter Signal Strength', *Sensors*, vol. 12, pp. 895–904, 2012, doi: 10.3390/s120100895.
- [123] A. Groenewald and W. A. Groenewald, 'Development of a universal medical X-ray imaging phantom prototype.', *J Appl Clin Med Phys*, vol. 17, no. 6, pp. 356–365, 2016, doi: 10.1120/jacmp.v17i6.6356.
- [124] Y. Watanabe and C. Constantinou, 'Phantom Materials in Radiology', in *Encyclopedia of Medical Devices and Instrumentation*, 2006. doi: 10.1002/0471732877.emd201.

-
- [125] 'QRM'. Accessed: Nov. 22, 2023. [Online]. Available: <https://www.qrm.de/en/about/about-phantoms/>
- [126] S. W. Smith, M. F. Insana, and H. Lopez, 'New contrast-detail phantoms for improved precision in lesion detection measurements', *Ultrasound Med Biol*, 1989, doi: 10.1016/0301-5629(89)90050-1.
- [127] M. Ahmad *et al.*, 'Chemical characteristics, motivation and strategies in choice of materials used as liver phantom: A literature review', *Journal of Medical Ultrasound*, vol. 28, no. 1. 2020. doi: 10.4103/JMU.JMU_4_19.
- [128] C. D. Nguyen *et al.*, 'Investigation of silk as a phantom material for ultrasound and photoacoustic imaging', *Photoacoustics*, vol. 28, 2022, doi: 10.1016/j.pacs.2022.100416.
- [129] S. M. Shalbi, A. A. Oglat, B. Albarbar, F. Elkut, M. A. Qaeed, and A. A. Arra, 'A brief review for common doppler ultrasound flow phantoms', *Journal of Medical Ultrasound*, vol. 28, no. 3. 2020. doi: 10.4103/JMU.JMU_96_19.
- [130] T. Tkaczyk *et al.*, 'High resolution, molecular-specific, reflectance imaging in optically dense tissue phantoms with structured-illumination.', *Opt Express*, 2004, doi: 10.1364/OPEX.12.003745.
- [131] U. Sukowski, F. Schubert, D. Grosenick, and H. Rinneberg, 'Preparation of solid phantoms with defined scattering and absorption properties for optical tomography', *Phys Med Biol*, 1996, doi: 10.1088/0031-9155/41/9/017.
- [132] G. Liu *et al.*, 'Fabrication of a multilayer tissue-mimicking phantom with tunable optical properties to simulate vascular oxygenation and perfusion for optical imaging technology', *Appl Opt*, vol. 57, no. 23, p. 6772, Nov. 2018, doi: 10.1364/AO.57.006772.
- [133] A. T. Peek, G. P. L. Thomas, D. F. Leotta, P. V. Yuldashev, V. A. Khokhlova, and T. D. Khokhlova, 'Robust and durable aberrative and absorptive phantom for therapeutic ultrasound applications', *J Acoust Soc Am*, vol. 151, no. 5, 2022, doi: 10.1121/10.0010369.
- [134] M. Eames, Z. Larrabee, A. Hananel, F. Padilla, and J. F. Aubry, 'Low-Cost Thermochromic Quality Assurance Phantom for Therapeutic Ultrasound Devices: A Proof of Concept', *Ultrasound Med Biol*, vol. 49, no. 1, 2023, doi: 10.1016/j.ultrasmedbio.2022.09.001.
- [135] N. GÜN, B. KARABOCE, and U. YURDALAN, 'Investigation of Therapeutic Ultrasound Dose on Muscle Phantom: An Experimental Study Investigation of

-
- Therapeutic Ultrasound Dose', *Clinical and Experimental Health Sciences*, vol. 12, no. 3, 2022, doi: 10.33808/clinexphealthsci.950896.
- [136] J. Laing, J. Moore, R. Vassallo, D. Bainbridge, M. Drangova, and T. Peters, 'Patient-specific cardiac phantom for clinical training and preprocedure surgical planning', *Journal of Medical Imaging*, vol. 5, no. 02, 2018, doi: 10.1117/1.jmi.5.2.021222.
- [137] E. Raeker-jordan, M. Martinez, and K. Shimada, '3D Printing of Customizable Phantoms to Replace Cadaveric Models in Upper Extremity Surgical Residency Training', *Materials*, vol. 15, no. 2, 2022, doi: 10.3390/ma15020694.
- [138] E. Choi *et al.*, 'A High-Fidelity Phantom for the Simulation and Quantitative Evaluation of Transurethral Resection of the Prostate', *Ann Biomed Eng*, vol. 48, no. 1, 2020, doi: 10.1007/s10439-019-02361-7.
- [139] Z. Zador, D. J. Coope, K. Gnanalingham, and M. T. Lawton, 'Quantifying surgical access in eyebrow craniotomy with and without orbital bar removal: Cadaver and surgical phantom studies', *Acta Neurochir (Wien)*, vol. 156, no. 4, 2014, doi: 10.1007/s00701-013-1947-y.
- [140] M. Higgins, S. Leung, and N. Radacsi, '3D printing surgical phantoms and their role in the visualization of medical procedures', *Annals of 3D Printed Medicine*, vol. 6, 2022. doi: 10.1016/j.stlm.2022.100057.
- [141] A. I. Chen *et al.*, 'Multilayered tissue mimicking skin and vessel phantoms with tunable mechanical, optical, and acoustic properties', *Med Phys*, vol. 43, no. 6, pp. 3117–3131, 2016, doi: 10.1118/1.4951729.
- [142] J. Yin, M. Li, G. Dai, H. Zhou, L. Ma, and Y. Zheng, '3D Printed Multi-material Medical Phantoms for Needle-tissue Interaction Modelling of Heterogeneous Structures', *J Bionic Eng*, vol. 18, no. 2, 2021, doi: 10.1007/s42235-021-0031-1.
- [143] J. I. Gear, C. Cummings, J. Sullivan, N. Cooper-Rayner, P. Downs, and I. Murray, 'Radioactive 3D printing for the production of molecular imaging phantoms', *Phys Med Biol*, vol. 65, no. 17, 2020, doi: 10.1088/1361-6560/aba40e.
- [144] S. Jenne, H. Zappe, and S. Herdt, 'Towards pulsatile multilayer tissue phantoms', 2022. doi: 10.1117/12.2608118.
- [145] S. Jenne and H. Zappe, 'Multiwavelength tissue-mimicking phantoms with tunable vessel pulsation', *J Biomed Opt*, vol. 28, no. 04, 2023, doi: 10.1117/1.jbo.28.4.045003.

-
- [146] J. Zhu, B. Wang, Y. Zhang, T. Wei, and T. Gao, 'Living electrochemical biosensing: Engineered electroactive bacteria for biosensor development and the emerging trends', *Biosensors and Bioelectronics*, vol. 237. 2023. doi: 10.1016/j.bios.2023.115480.
- [147] Z. Guo, H. Liu, W. Dai, and Y. Lei, 'Responsive principles and applications of smart materials in biosensing', *Smart Materials in Medicine*, vol. 1. 2020. doi: 10.1016/j.smaim.2020.07.001.
- [148] L. Al-Zogbi, B. Bock, S. Schaffer, T. Fleiter, and A. Krieger, 'A 3-D-Printed Patient-Specific Ultrasound Phantom for FAST Scan', *Ultrasound Med Biol*, vol. 47, no. 3, 2021, doi: 10.1016/j.ultrasmedbio.2020.11.004.
- [149] M. Alssabbagh, A. A. Tajuddin, M. Abdulmanap, and R. Zainon, 'Evaluation of 3D printing materials for fabrication of a novel multi-functional 3D thyroid phantom for medical dosimetry and image quality', *Radiation Physics and Chemistry*, vol. 135, 2017, doi: 10.1016/j.radphyschem.2017.02.009.
- [150] C. M. Chen, R. M. Kwasnicki, V. F. Curto, G. Z. Yang, and B. P. L. Lo, 'Tissue Oxygenation Sensor and an Active In Vitro Phantom for Sensor Validation', *IEEE Sens J*, vol. 19, no. 18, 2019, doi: 10.1109/JSEN.2019.2917122.
- [151] C.-M. Chen, R. Kwasnicki, B. Lo, and G. Z. Yang, 'Wearable Tissue Oxygenation Monitoring Sensor and a Forearm Vascular Phantom Design for Data Validation', in *2014 11th International Conference on Wearable and Implantable Body Sensor Networks*, IEEE, Nov. 2014, pp. 64–68. doi: 10.1109/BSN.2014.33.
- [152] R. W. C. G. R. Wijshoff, M. Mischi, J. Veen, A. M. van der Lee, and R. M. Aarts, 'Reducing motion artifacts in photoplethysmograms by using relative sensor motion: phantom study', *J Biomed Opt*, vol. 17, no. 11, 2012, doi: 10.1117/1.jbo.17.11.117007.
- [153] A. N. BASHKATOV, E. A. GENINA, and V. V TUCHIN, 'OPTICAL PROPERTIES OF SKIN, SUBCUTANEOUS, AND MUSCLE TISSUES: A REVIEW', *J Innov Opt Health Sci*, vol. 04, no. 01, pp. 9–38, Nov. 2011, doi: 10.1142/S1793545811001319.
- [154] R. R. Anderson, B. S. And, and J. A. Parrish, 'The Optics of Human Skin', *Journal of Investigative Dermatology*, vol. 77. pp. 13–19, 1981. doi: 10.1111/1523-1747.ep12479191.
- [155] T. Y. Abay and P. A. Kyriacou, 'Investigation of photoplethysmography and Near Infrared Spectroscopy for the assessment of tissue blood perfusion', in *2014 36th Annual*

-
- International Conference of the IEEE Engineering in Medicine and Biology Society, EMBC 2014*, 2014. doi: 10.1109/EMBC.2014.6944837.
- [156] Y. H. Kao, P. C. P. Chao, Y. Hung, and C. L. Wey, 'A new reflective PPG LED-PD sensor module for cuffless blood pressure measurement at wrist artery', in *Proceedings of IEEE Sensors*, 2017. doi: 10.1109/ICSENS.2017.8234348.
- [157] C. O. Martinez-Ojeda and J. C. D. Cruz, 'Analysis of Source-to-Area Distance in PPG Signal Detection Using Phototransistor', in *2020 IEEE International Conference on Automatic Control and Intelligent Systems, I2CACIS 2020 - Proceedings*, 2020. doi: 10.1109/I2CACIS49202.2020.9140101.
- [158] V. Rybynok, J. M. May, K. Budidha, H. Njoun, J. P. Phillips, and P. A. Kyriacou, 'ZenPPG: A modular multi-channel photoplethysmography system', in *Innovations and Applications of Monitoring Perfusion, Oxygenation and Ventilation (I.A.M.P.O.V.)*, 2012, 2012.
- [159] A. N. BASHKATOV, E. A. GENINA, and V. V. TUCHIN, 'OPTICAL PROPERTIES OF SKIN, SUBCUTANEOUS, AND MUSCLE TISSUES: A REVIEW', *J Innov Opt Health Sci*, vol. 04, no. 01, pp. 9–38, Jan. 2011, doi: 10.1142/S1793545811001319.
- [160] E. Salomatina, B. Jiang, J. Novak, and A. N. Yaroslavsky, 'Optical properties of normal and cancerous human skin in the visible and near-infrared spectral range', *J Biomed Opt*, 2006, doi: 10.1117/1.2398928.
- [161] B. M. Leslie, L. K. Ruby, S. J. Madell, and F. Wittenstein, 'Digital artery diameters: An anatomic and clinical study', *Journal of Hand Surgery*, vol. 12, no. 5, pp. 740–743, 1987, doi: 10.1016/S0363-5023(87)80060-6.
- [162] A. N. Pruzan, A. E. Kaufman, C. Calcagno, Y. Zhou, Z. A. Fayad, and V. Mani, 'Feasibility of imaging superficial palmar arch using micro-ultrasound, 7T and 3T magnetic resonance imaging.', *World J Radiol*, vol. 9, no. 2, pp. 79–84, Nov. 2017, doi: 10.4329/wjr.v9.i2.79.
- [163] P. Di Ninni, F. Martelli, and G. Zaccanti, 'The use of India ink in tissue-simulating phantoms', *Opt Express*, vol. 18, no. 26, p. 26854, Nov. 2010, doi: 10.1364/OE.18.026854.
- [164] S. Laurent *et al.*, 'Elastic modulus of the radial artery wall material is not increased in patients with essential hypertension', *Arterioscler Thromb Vasc Biol*, vol. 14, no. 7, 1994, doi: 10.1161/01.ATV.14.7.1223.

-
- [165] Y. M. Ku *et al.*, 'Ultrasonographic measurement of intima-media thickness of radial artery in pre-dialysis uraemic patients: Comparison with histological examination', *Nephrology Dialysis Transplantation*, vol. 21, no. 3, 2006, doi: 10.1093/ndt/gfi214.
- [166] G. J. Langewouters, A. Zwart, R. Busse, and K. H. Wesseling, 'Pressure-diameter relationships of segments of human finger arteries', *Clinical Physics and Physiological Measurement*, vol. 7, no. 1, 1986, doi: 10.1088/0143-0815/7/1/003.
- [167] M. F. Griffin, B. C. Leung, Y. Premakumar, M. Szarko, and P. E. Butler, 'Comparison of the mechanical properties of different skin sites for auricular and nasal reconstruction', *Journal of Otolaryngology - Head and Neck Surgery*, vol. 46, no. 1, 2017, doi: 10.1186/s40463-017-0210-6.
- [168] C. Opreșan, V. Cârlescu, A. Barnea, G. Prisacaru, D. N. Olaru, and G. Plesu, 'Experimental determination of the Young's modulus for the fingers with application in prehension systems for small cylindrical objects', in *IOP Conference Series: Materials Science and Engineering*, 2016. doi: 10.1088/1757-899X/147/1/012058.
- [169] M. Hickey, N. Samuels, N. Randive, R. M. Langford, and P. A. Kyriacou, 'Measurement of splanchnic photoplethysmographic signals using a new reflectance fiber optic sensor City Research Online Measurement of splanchnic photoplethysmographic signals using a new reflectance fiber optic sensor of Photo-Optical Instrumentation', *J Biomed Opt*, vol. 15, no. 2, p. 27012, 2010, doi: 10.1117/1.3374355.
- [170] C. I. Nwafor *et al.*, 'Assessment of a noninvasive optical photoplethysmography imaging device with dynamic tissue phantom models', *J Biomed Opt*, 2017, doi: 10.1117/1.jbo.22.9.096003.
- [171] G. E. Strangman, Z. Li, and Q. Zhang, 'Depth Sensitivity and Source-Detector Separations for Near Infrared Spectroscopy Based on the Colin27 Brain Template', *PLoS One*, vol. 8, no. 8, 2013, doi: 10.1371/journal.pone.0066319.
- [172] S. Gunadi, T. S. Leung, C. E. Elwell, and I. Tachtsidis, 'Spatial sensitivity and penetration depth of three cerebral oxygenation monitors', *Biomed Opt Express*, vol. 5, no. 9, 2014, doi: 10.1364/boe.5.002896.
- [173] N. Westerhof, G. Elzinga, and P. Sipkema, 'An artificial arterial system for pumping hearts.', *J Appl Physiol*, vol. 31, no. 5, pp. 776-781, Nov. 1971, doi: 10.1152/jappl.1971.31.5.776.

-
- [174] M. Nitzan *et al.*, 'Comparison of systolic blood pressure values obtained by photoplethysmography and by Korotkoff sounds.', *Sensors (Basel)*, vol. 13, no. 11, pp. 14797–14812, 2013, doi: 10.3390/s131114797.